The formation of ultrafine grained microstructure in a plain C-Mn steel

D. Ponge, R. Song, M. Calcagnotto, D. Raabe

Introduction

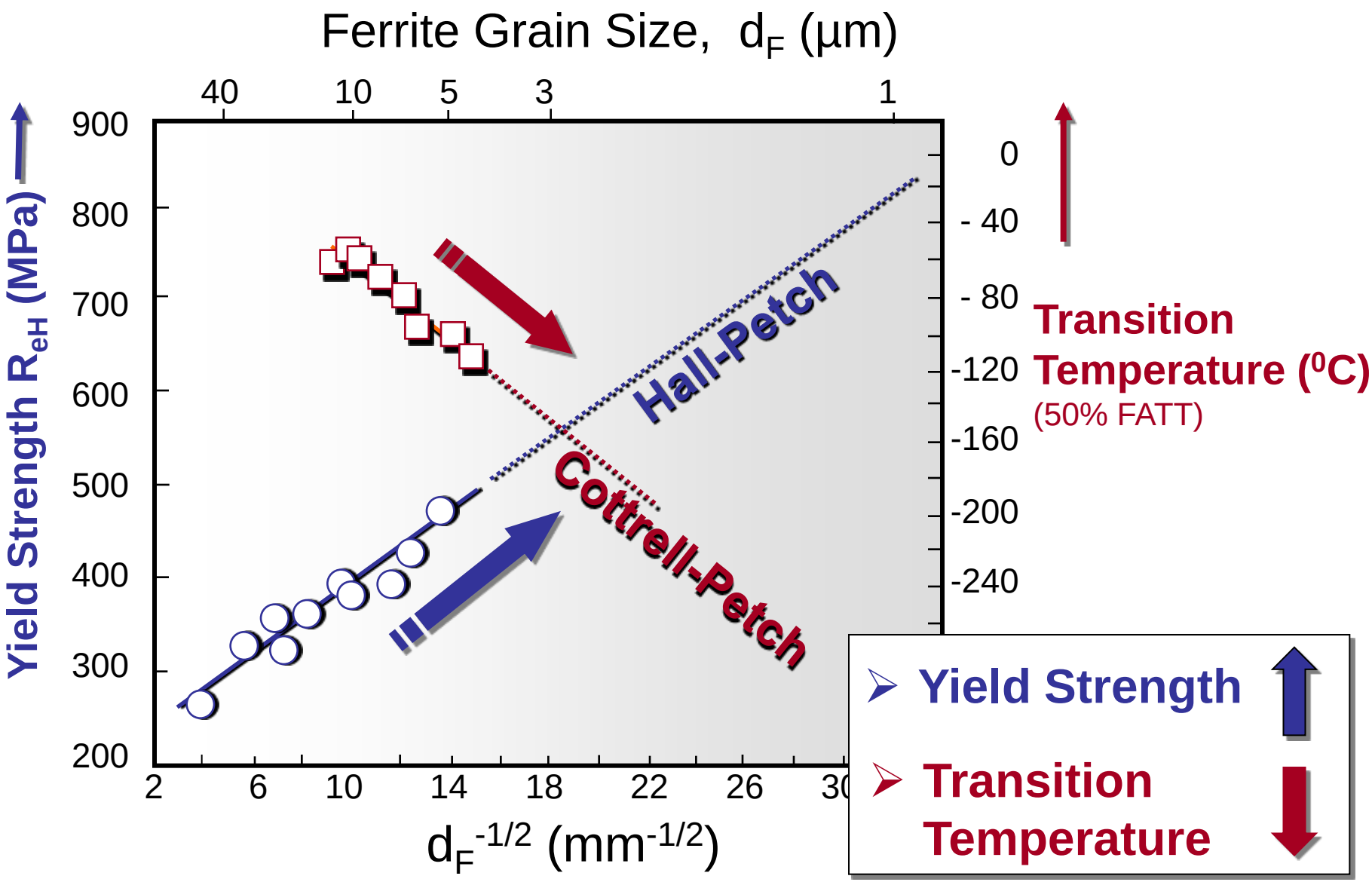

Problems/Challenges

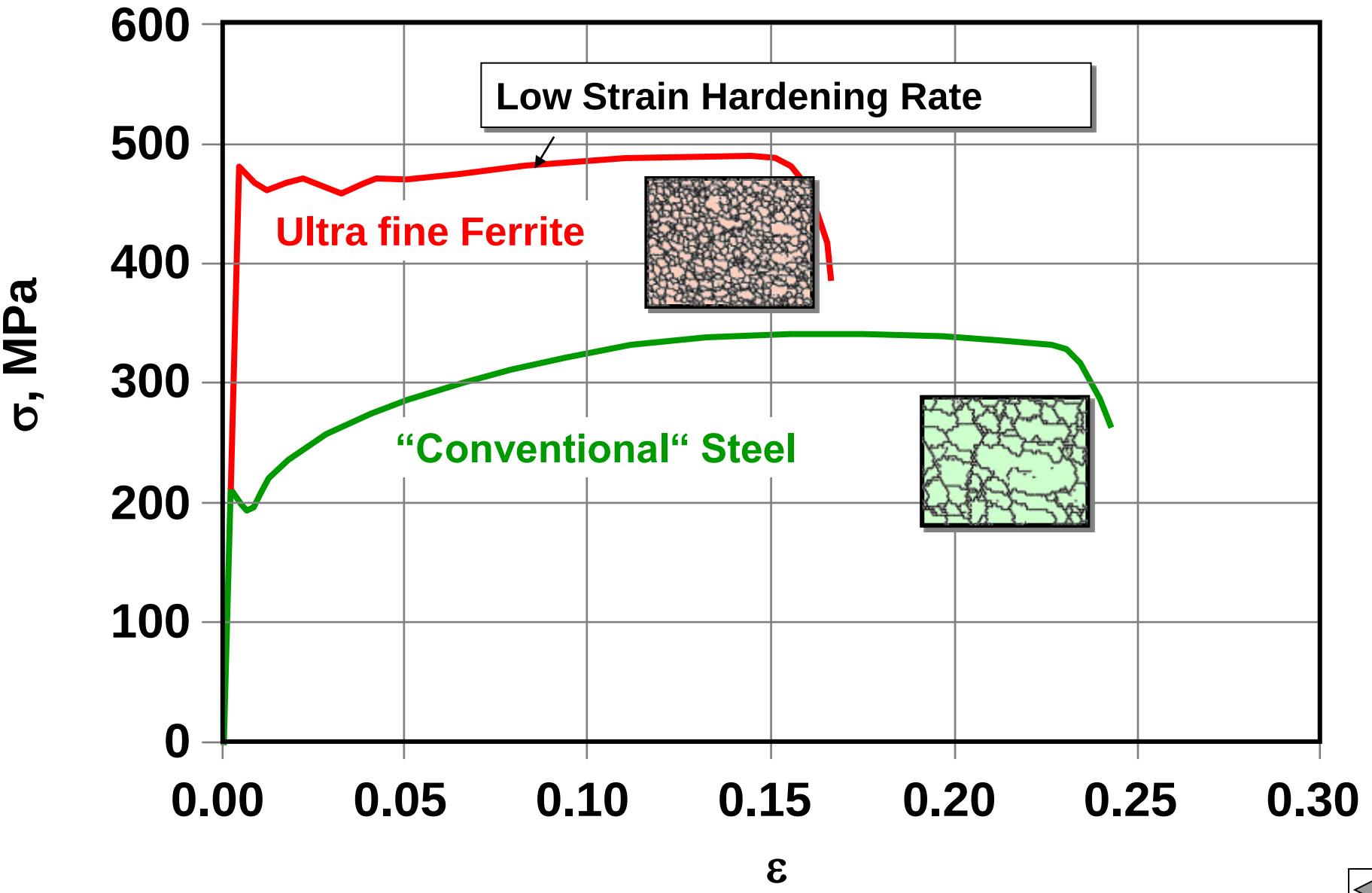

Methods to increase strain hardening rate

- precipitations (cementite, VC ...) — **Part I**
- broad or bimodal grain size distribution
- Dual-Phase steel (Ferrite + Martensite) — **Part II**
- ...

Part I

UFG steel (ferrite, cementite)

R. Song, D. Ponge, D. Raabe

Outline Part I (UFG ferrite+cementite)

- **Concept**
- Physical simulation of processing
- Microstructure and microstructure evolution
- Impact tests (Effect of microstructure)
- Effect of C
- Effect of Mn
- Conclusions Part I

Concept

- Ultrafine grain in a plain C-Mn steel

- Fine and homogeneous distribution of cementite
  (increase strain hardening rate and thermal stability)

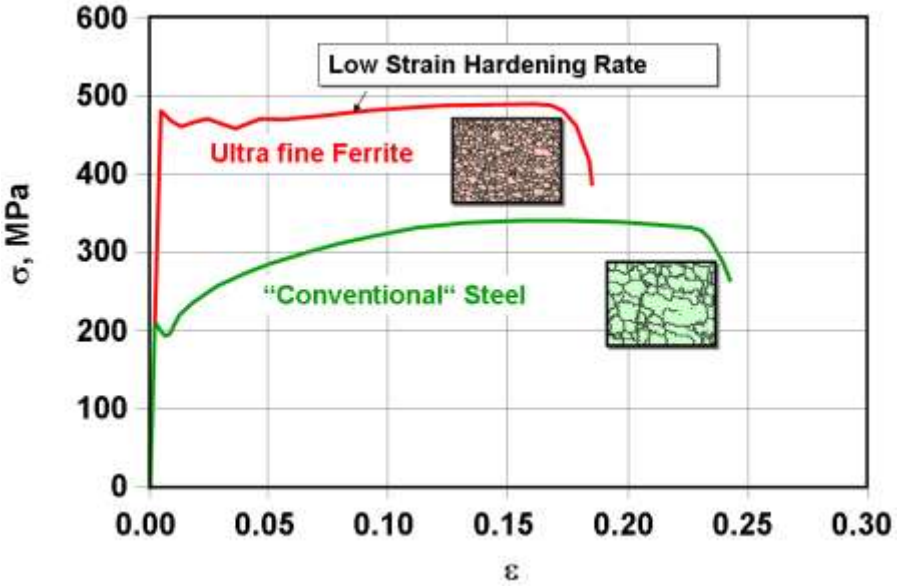

- Processing applicable for large scale production

Compositions (mass %)

Steel	C	Mn
0.15C	0.17	0.76
0.20C	0.22	0.74
0.20CMn	0.23	1.52
0.30C	0.31	0.76

	Si	P	S	Al	N
all steels	0.22	.004	.004	.030	.001

Pony Mill - Concept

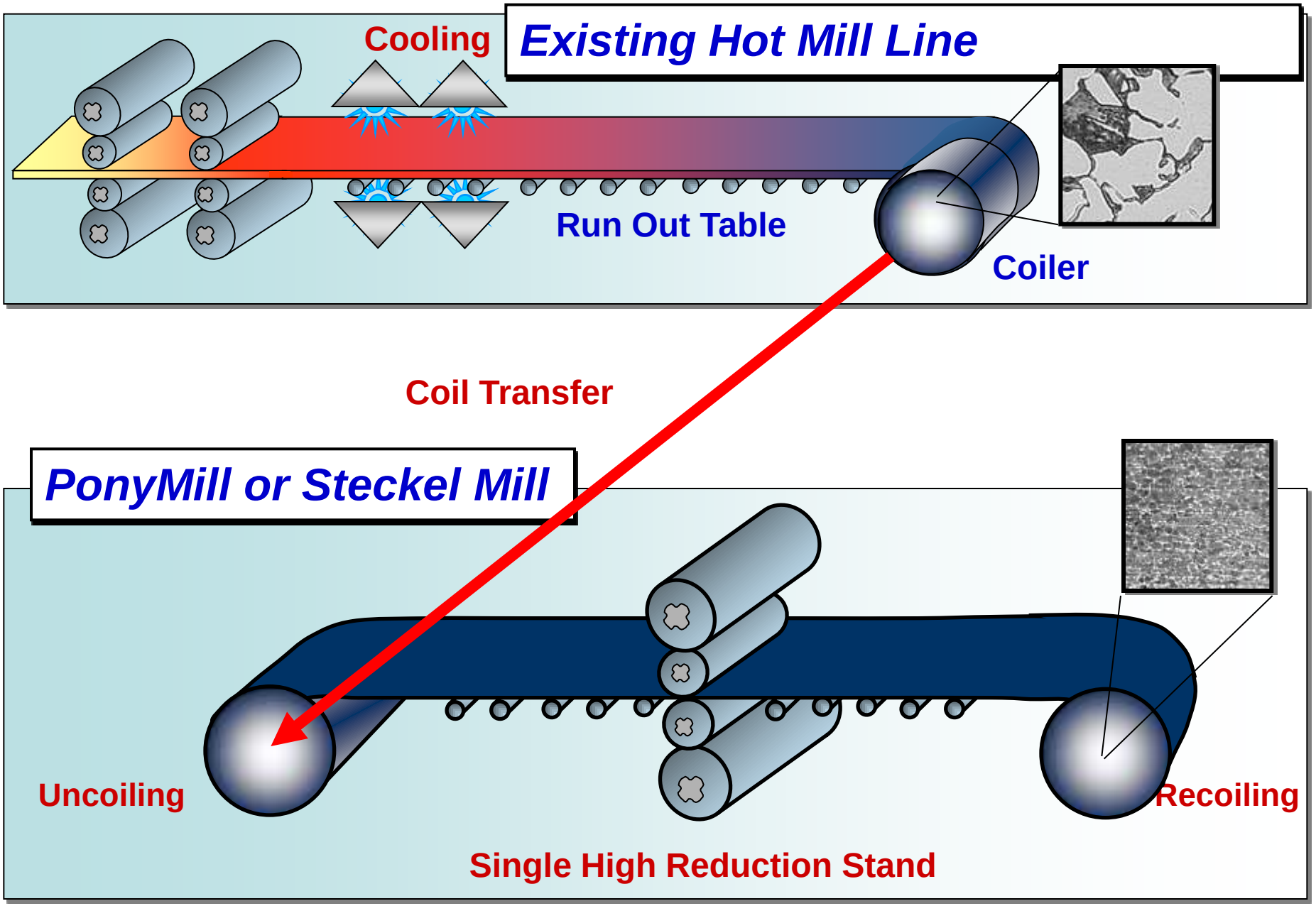

Outline Part I (UFG ferrite+cementite)

- Concept
- **Physical simulation of processing**
- Microstructure and microstructure evolution
- Impact tests (Effect of microstructure)
- Effect of C
- Effect of Mn
- Conclusions Part I

Hot Working Simulator ”WUMSI“

The Hot Working Simulator

(WarmUMformSImulator)

“WUMSI”

Hot Working Simulator ”WUMSI“

Course of a Hot Working Simulation

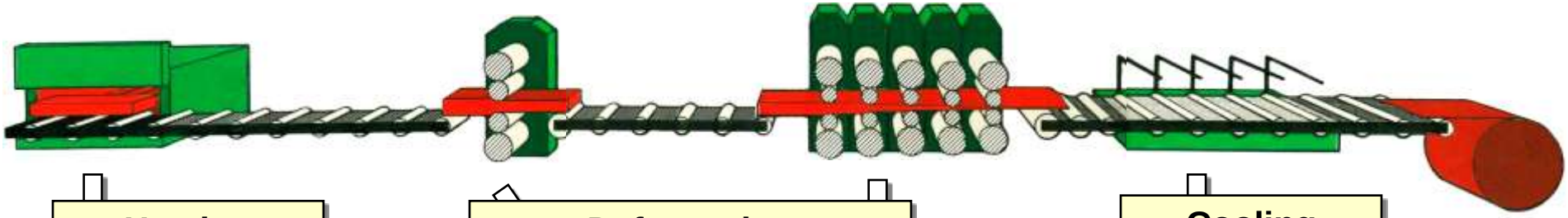

Heating

Deformation

Cooling

$$0\,K/s \leq \dot{T} \leq 400\,K/s$$

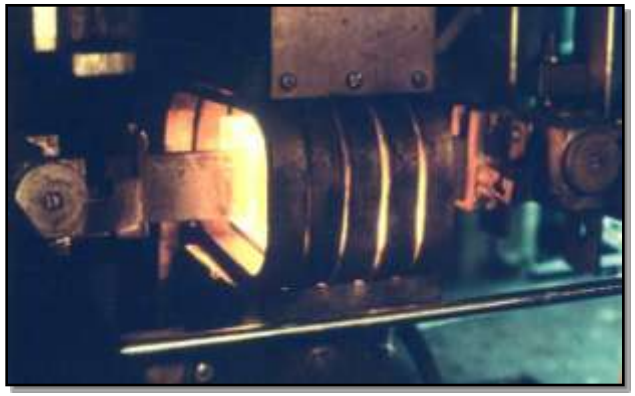

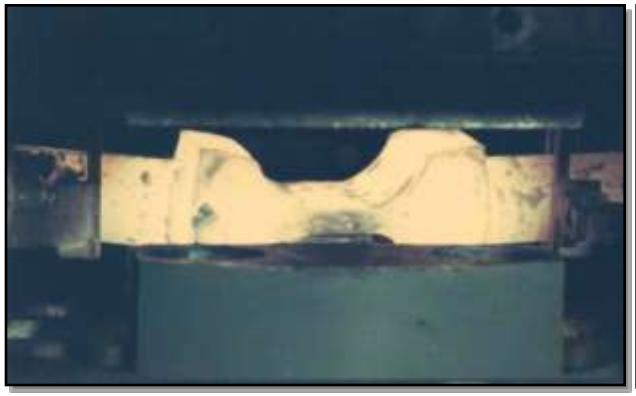

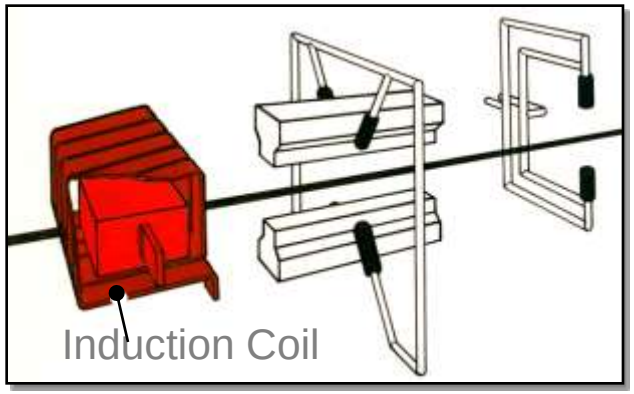

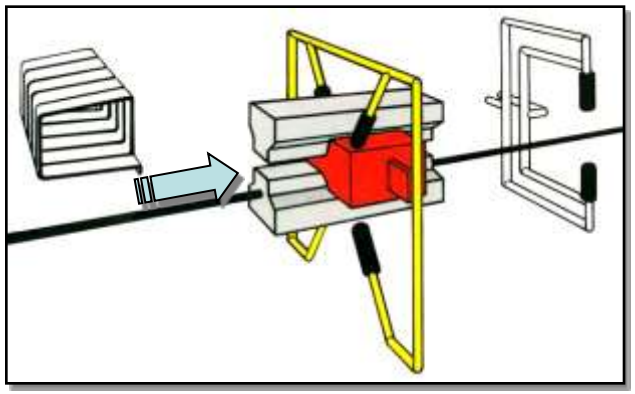

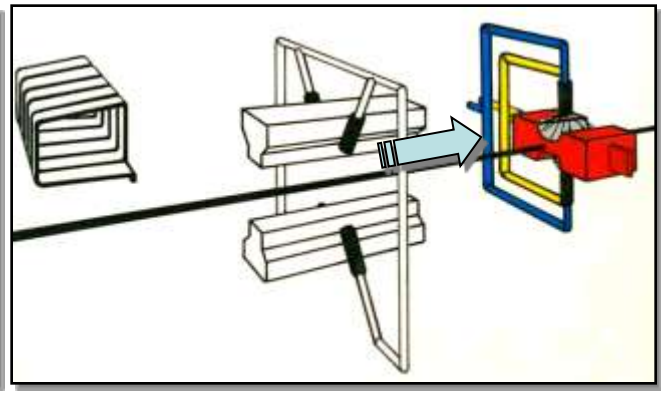

Plane Strain Compression Test

$\dot{\varepsilon}_{max}=100s^{-1}$

Minimum interpass time: 50ms

$\varepsilon_{max}=2.5$

Secondary Specimen

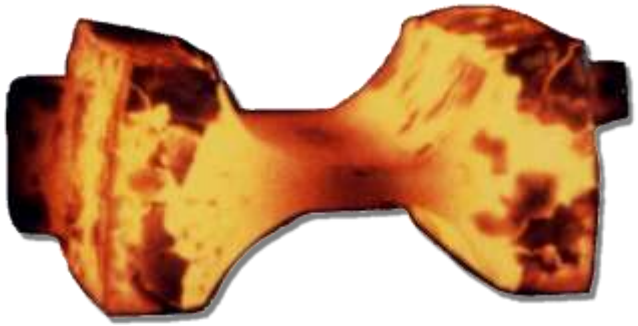

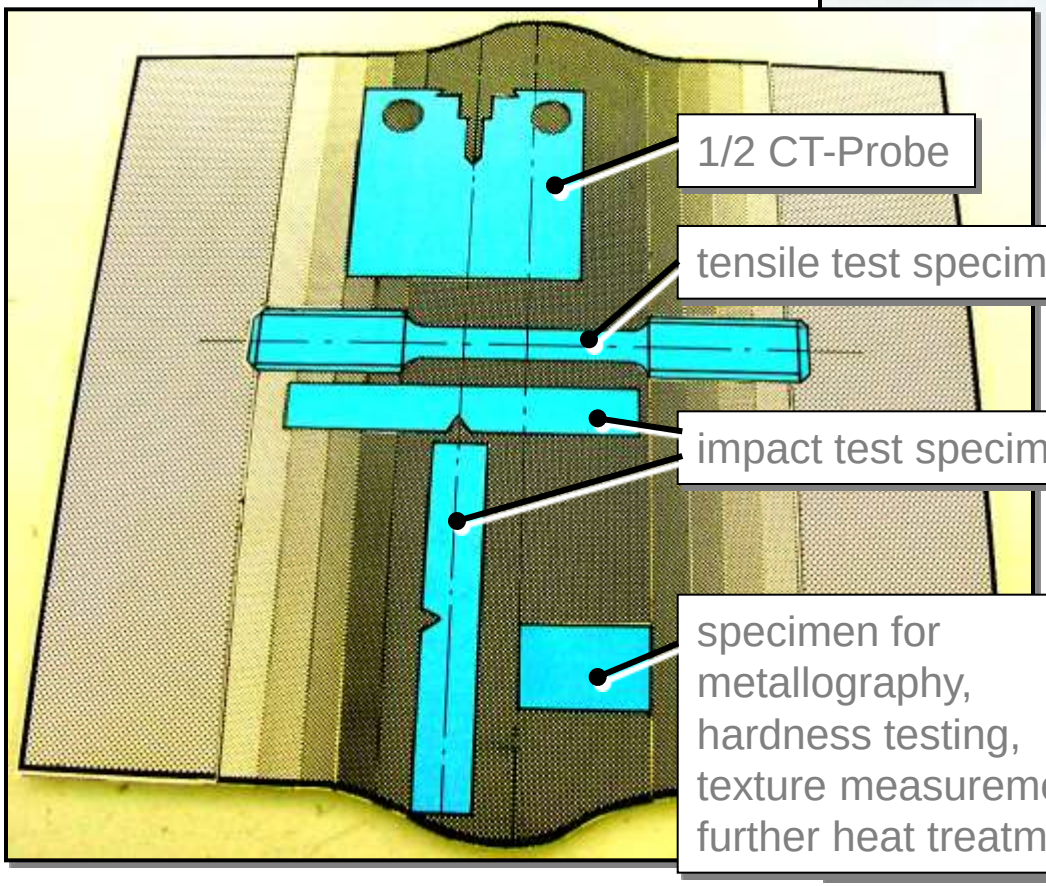

Physical simulation (WUMSI)

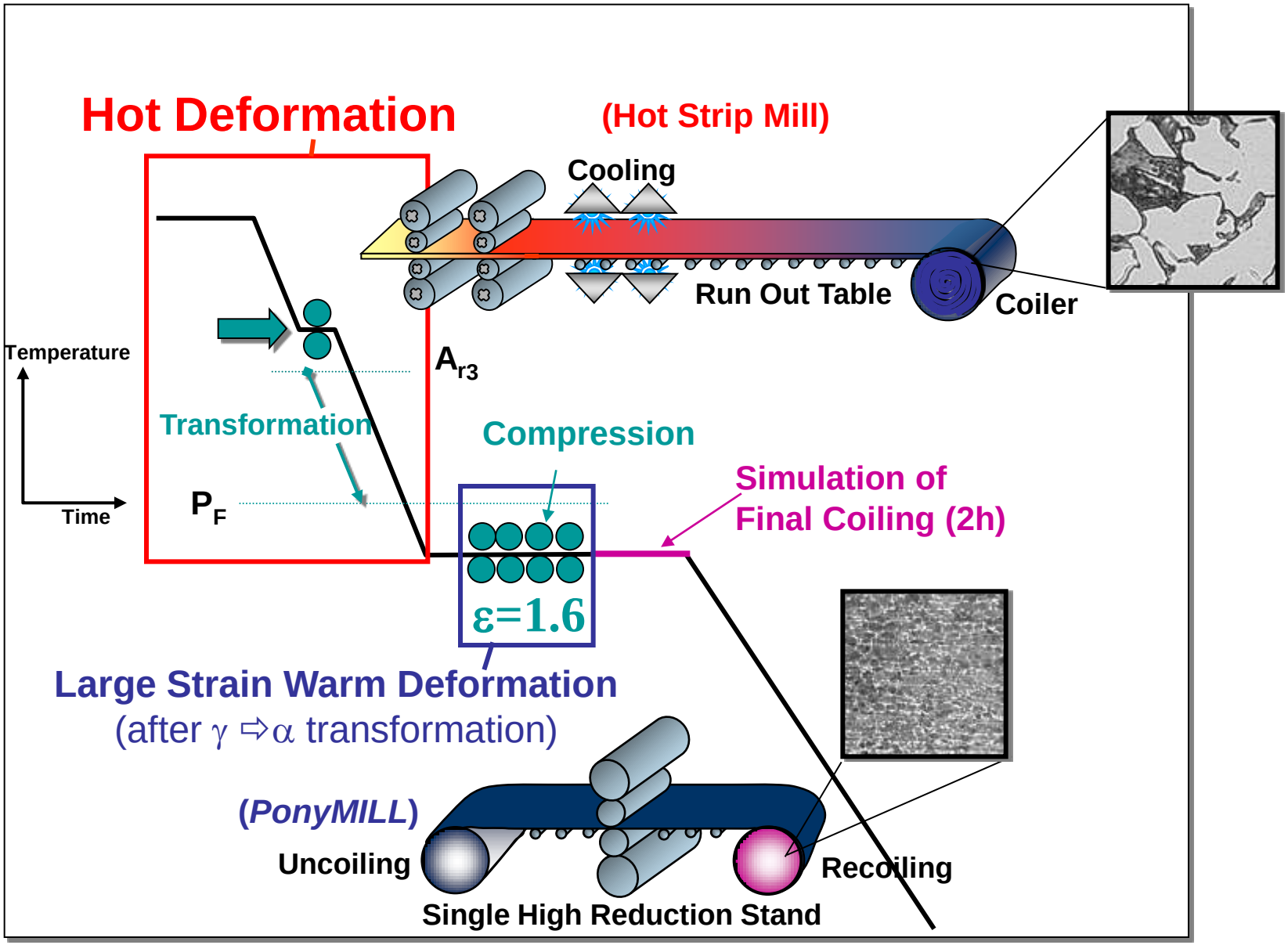

Processing (0.2%C; DCCT)

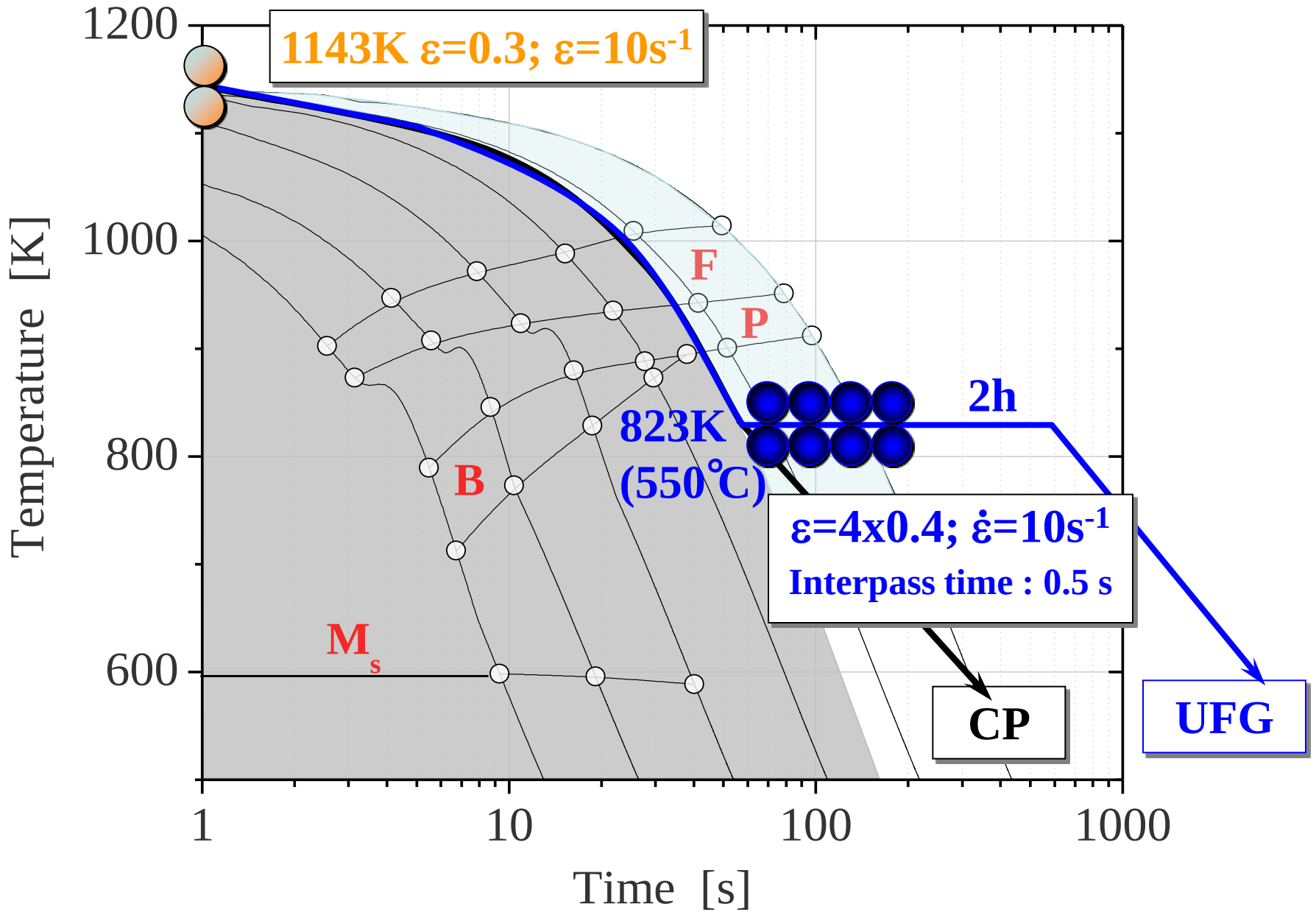

Outline Part I (UFG ferrite+cementite)

- Concept
- Physical simulation of processing
- **Microstructure and microstructure evolution**
- Impact tests (Effect of microstructure)
- Effect of C
- Effect of Mn
- Conclusions Part I

Microstructures 0.2%C

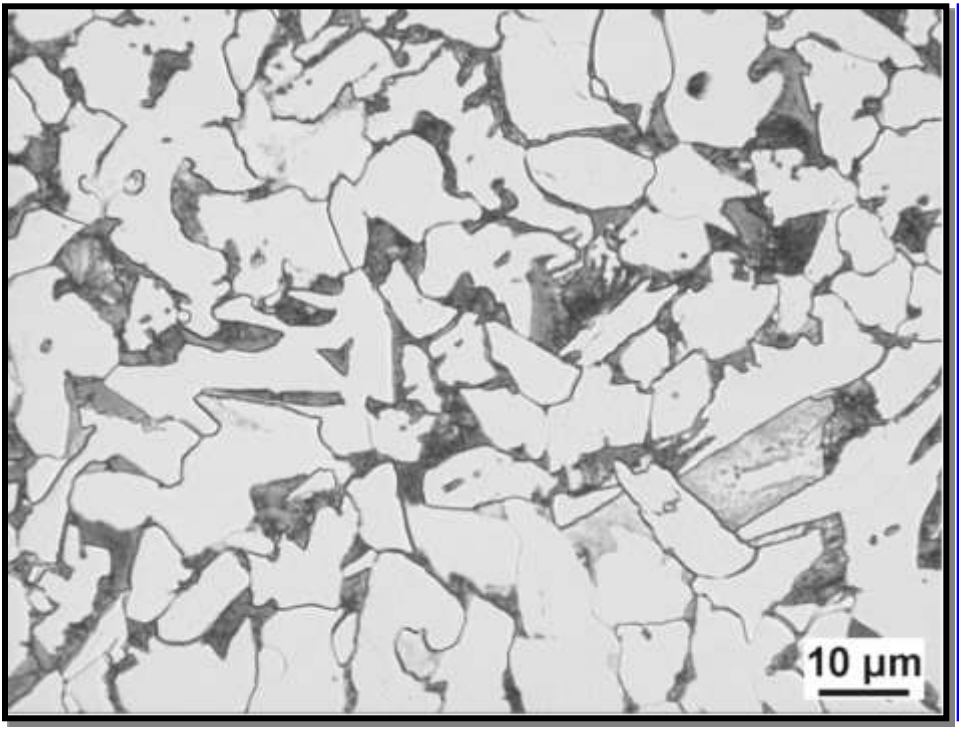

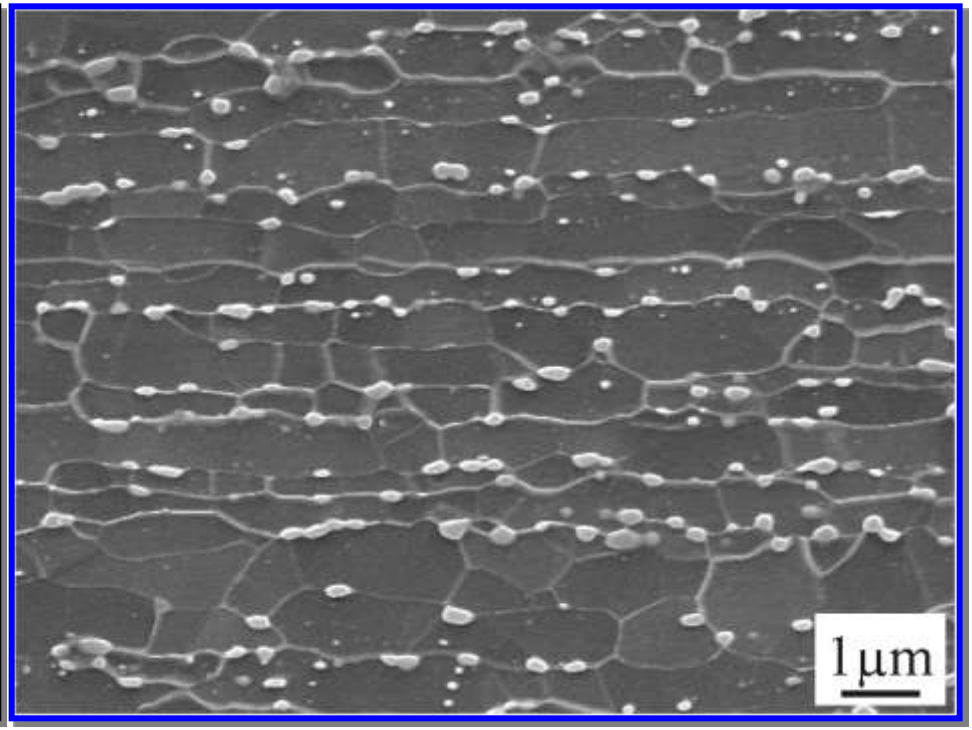

CP d_α= 6.8 µm

UFG d_α = 1.3 µm

Microstructure of the UFG steel — 0.2%CMn

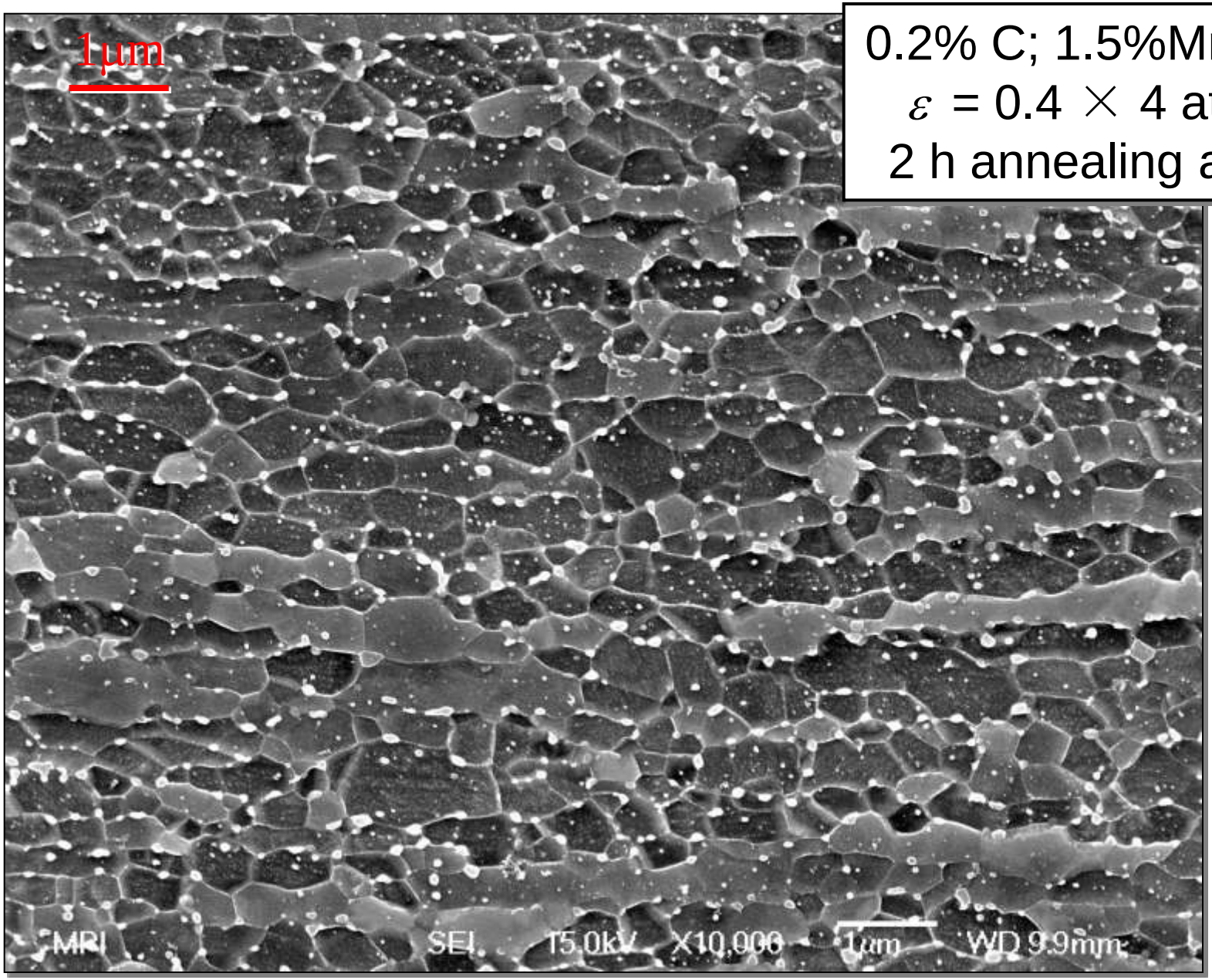

0.2% C; 1.5%Mn; 0.2%Si
ε = 0.4 × 4 at 823 K
2 h annealing at 823 K

Grain boundary character — 0.2%CMn

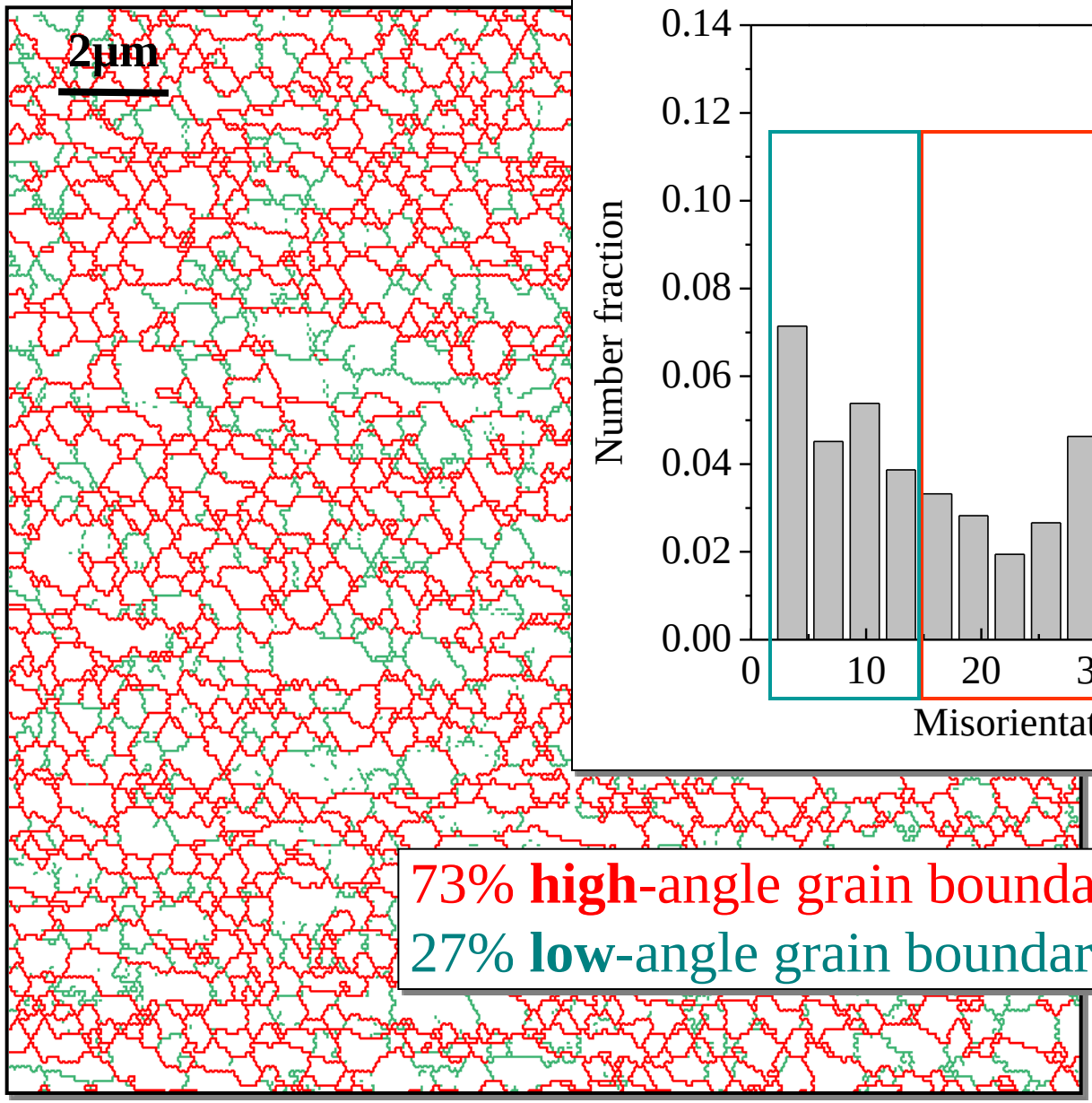

73% **high**-angle grain boundaries ($\theta \geq 15°$)

27% **low**-angle grain boundaries ($15° > \theta \geq 2°$)

Microstructure development during warm deformation

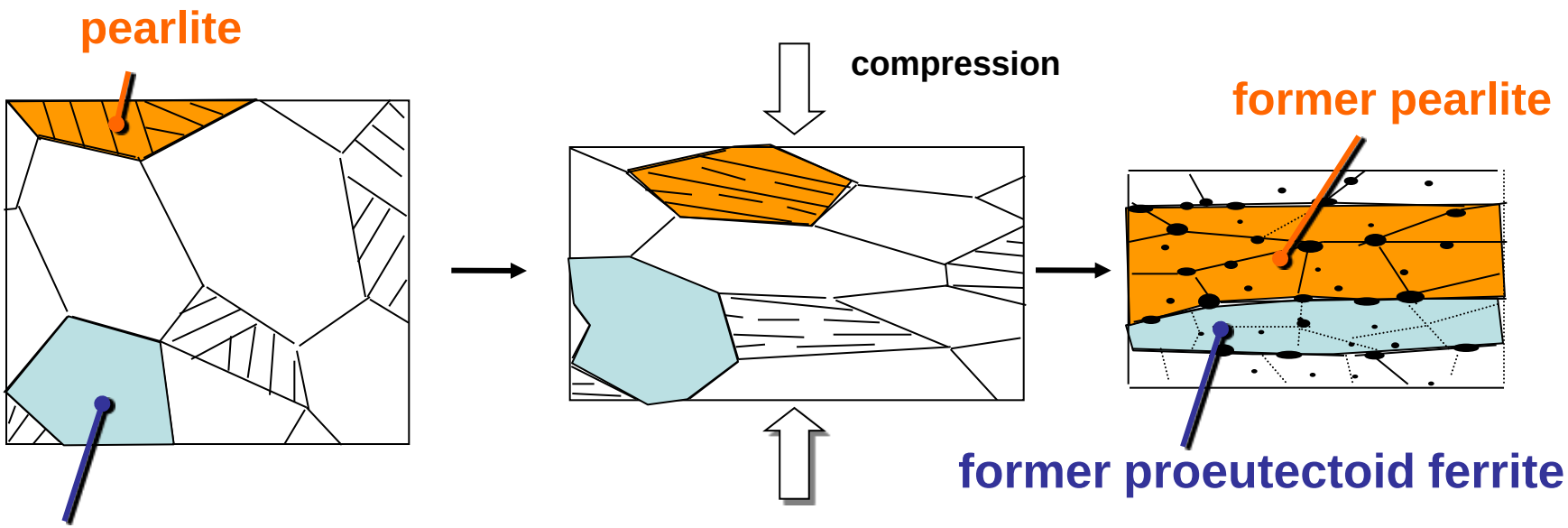

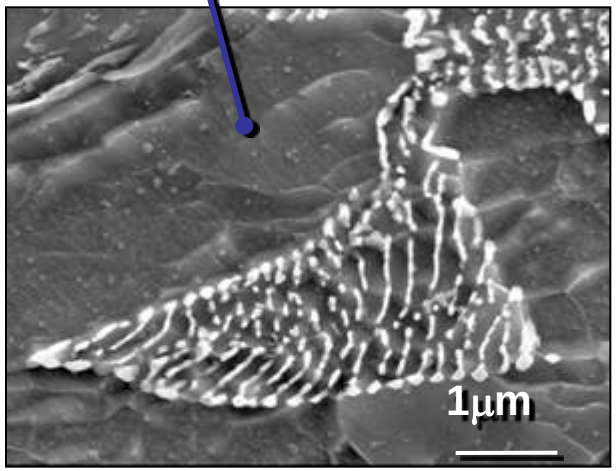

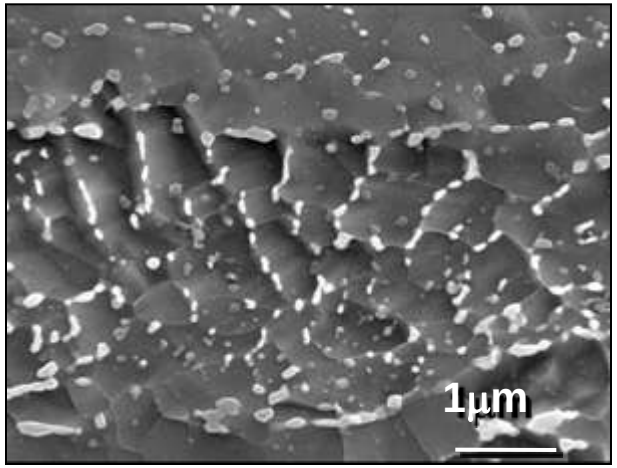

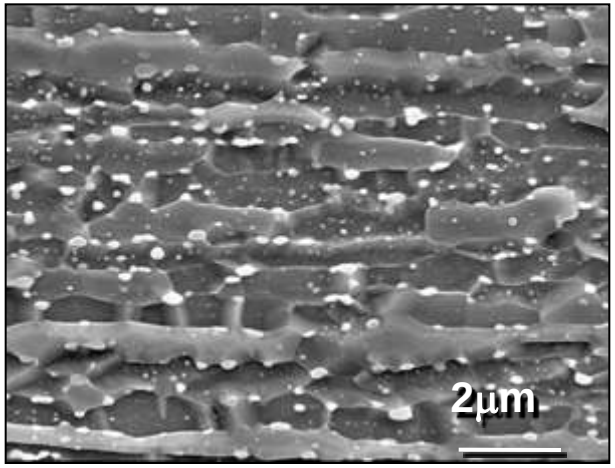

Microstructure development during warm deformation

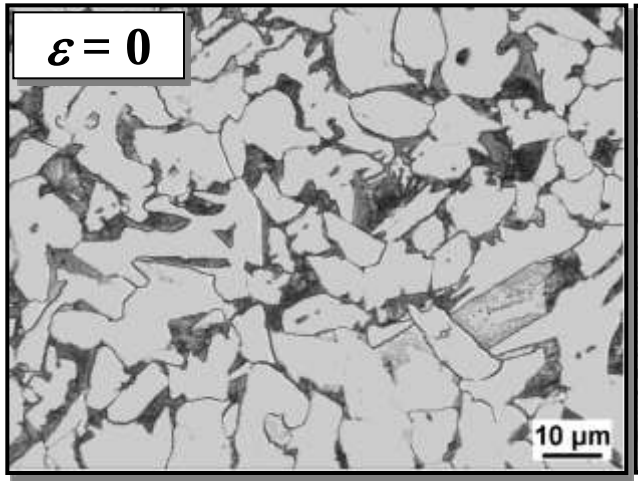

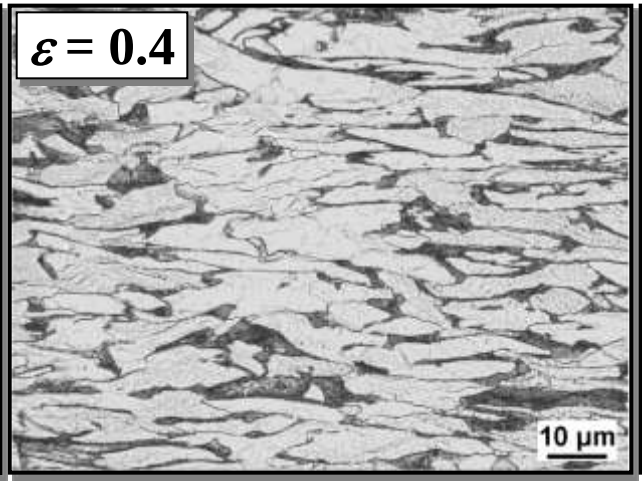

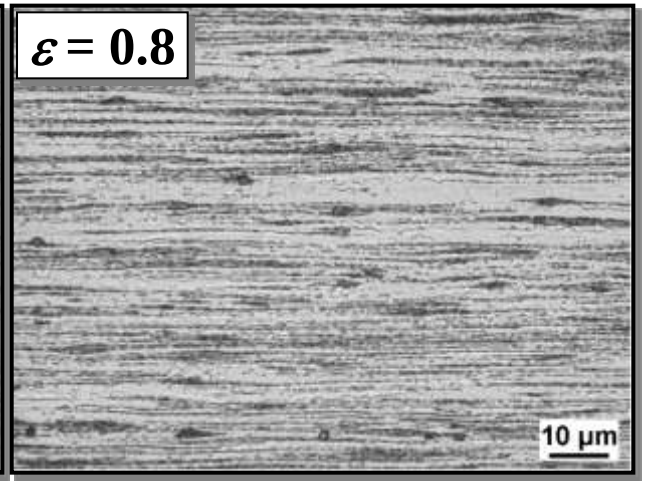

ND

RD

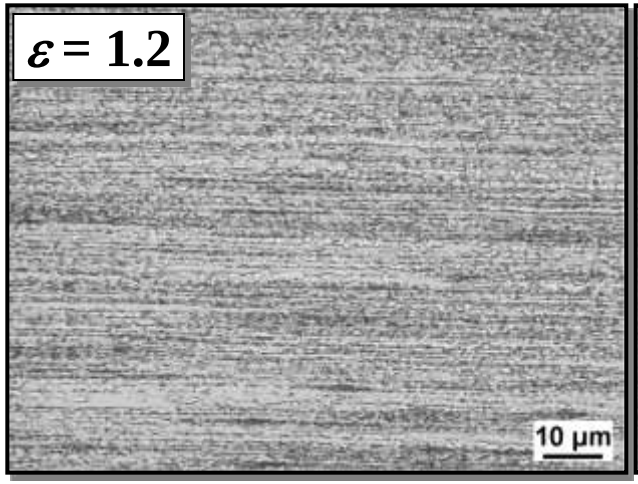

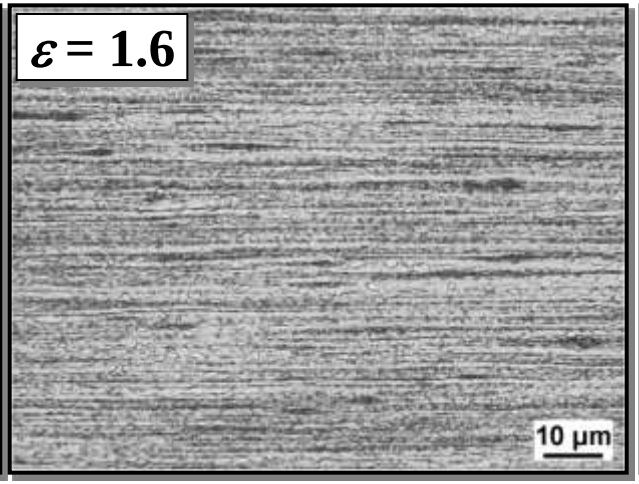

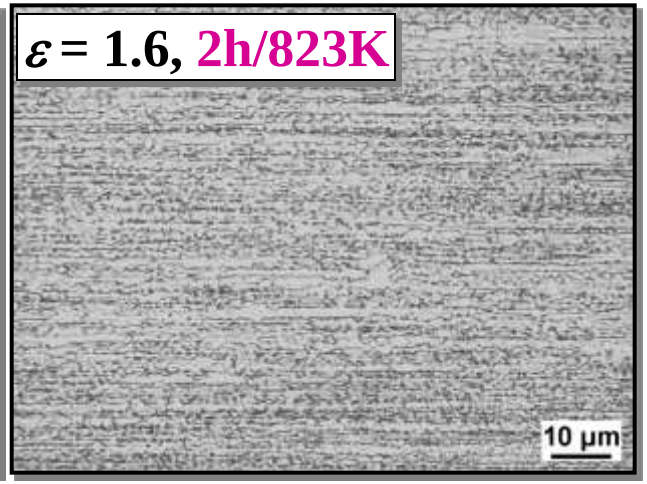

Microstructure development during warm deformation

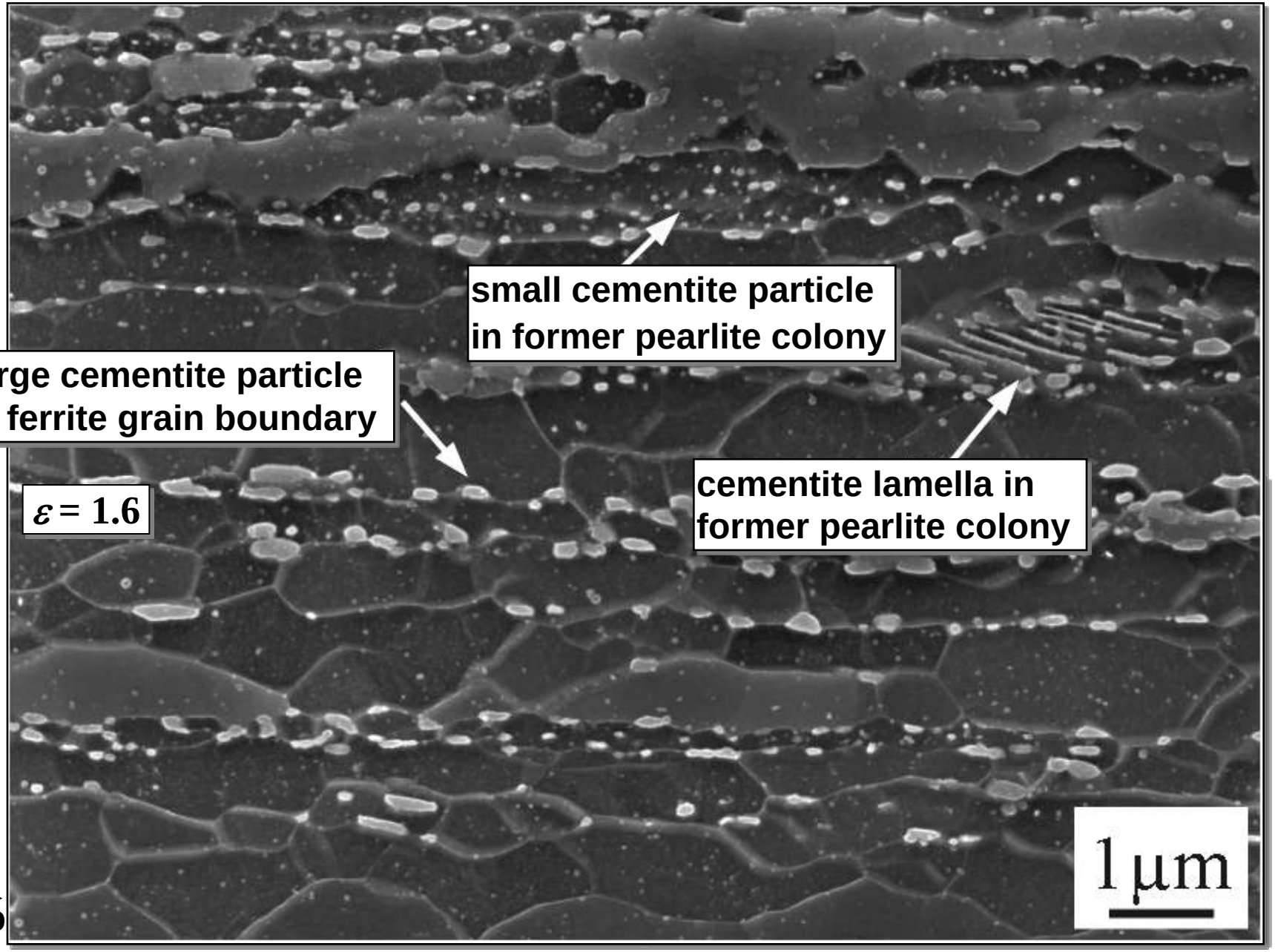

Evolution of grain size and shape during warm deformation

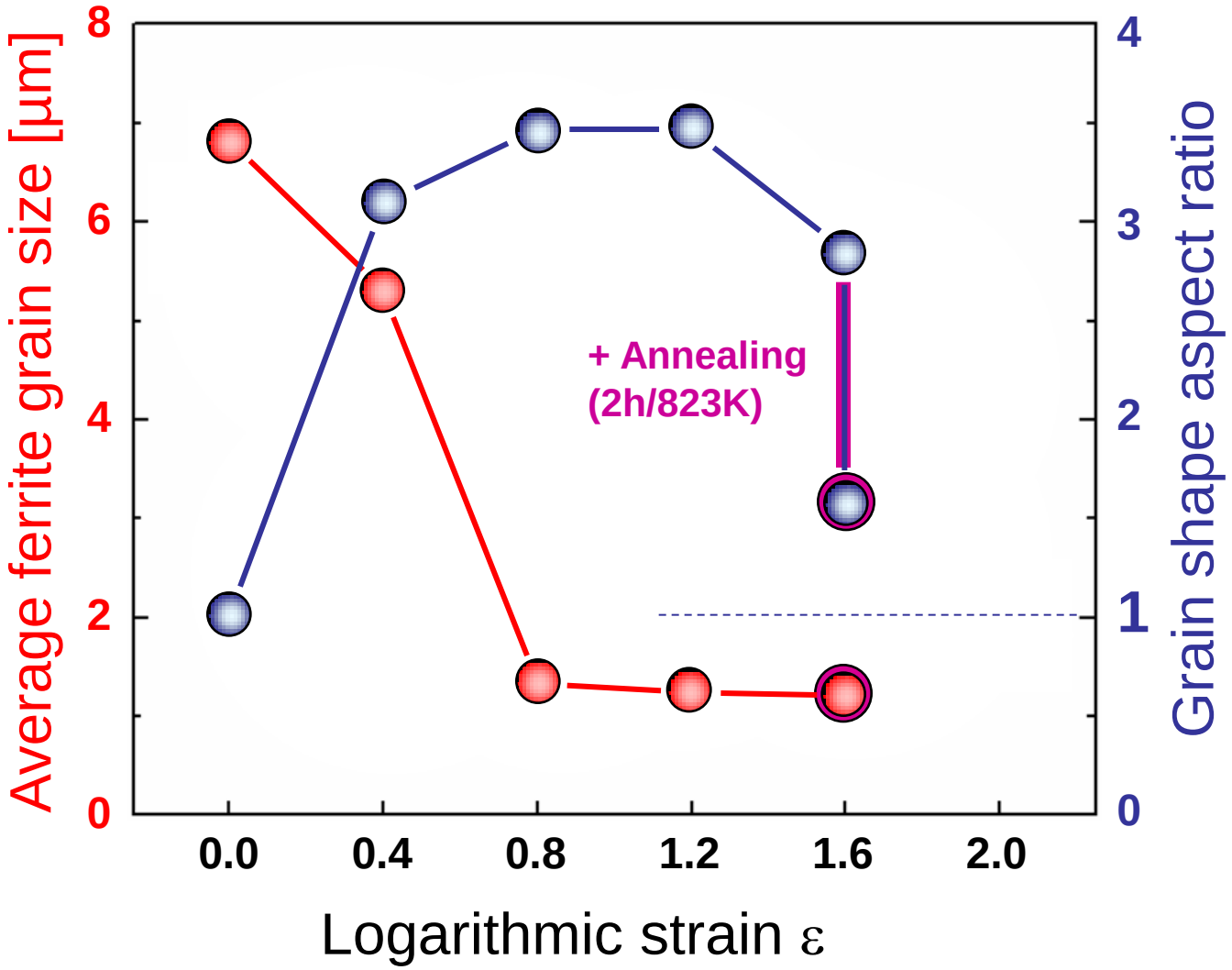

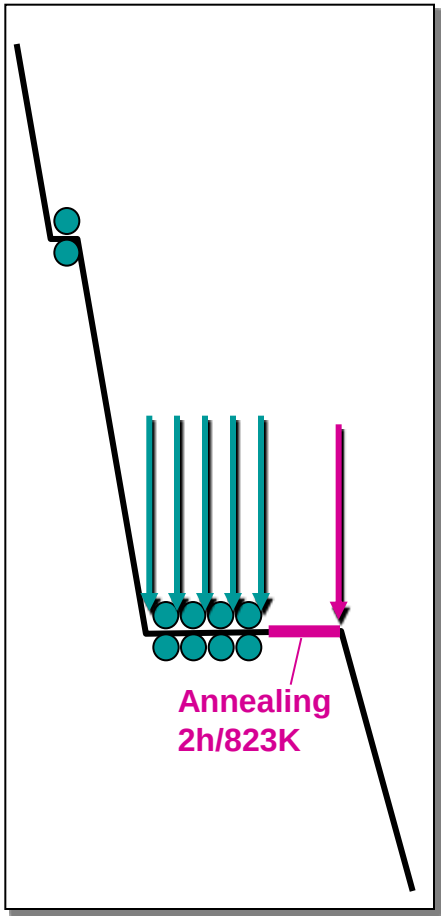

Fraction of High Angle Grain Boundaries (HAGBs)

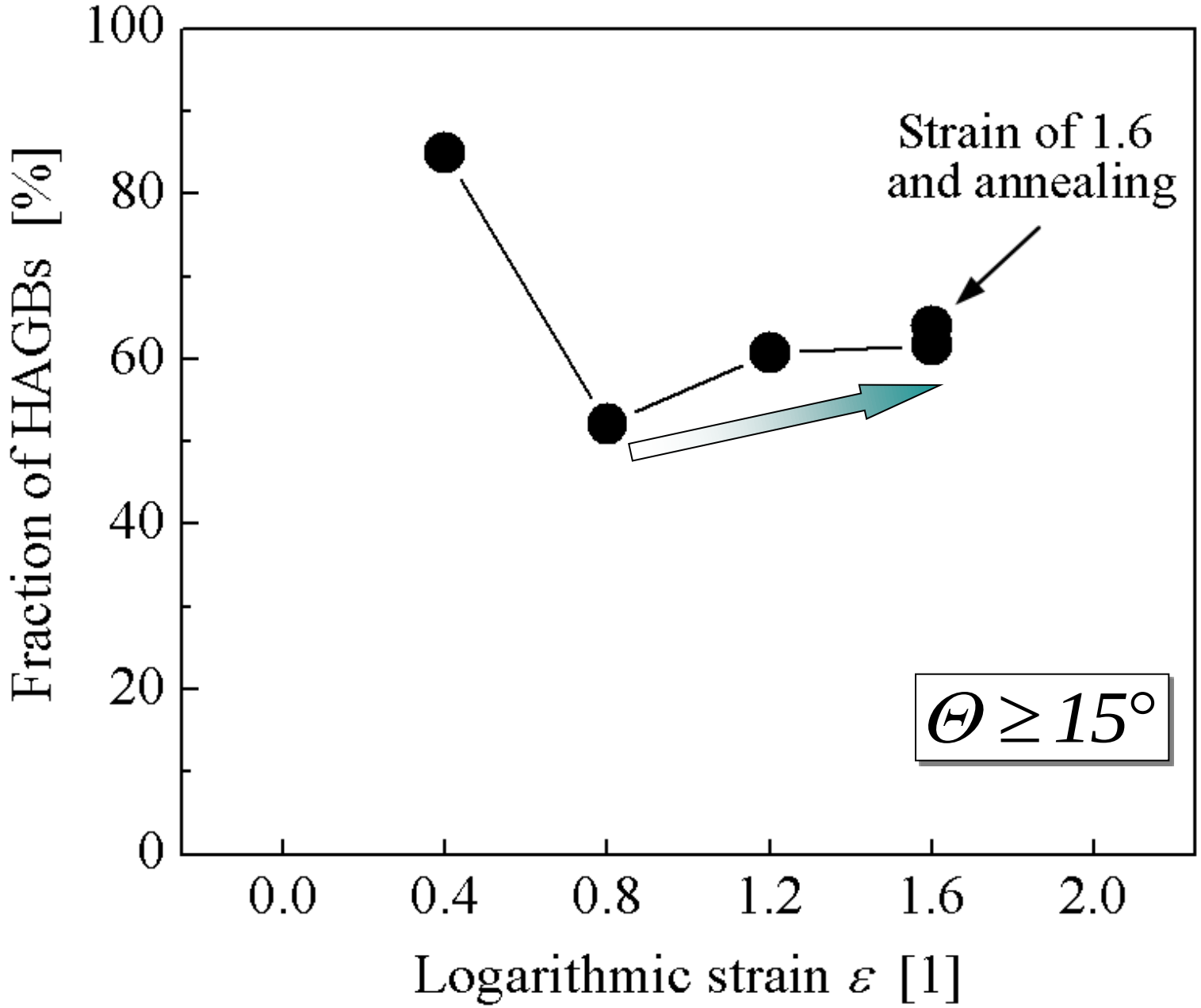

Microstructure before and after Annealing (TEM)

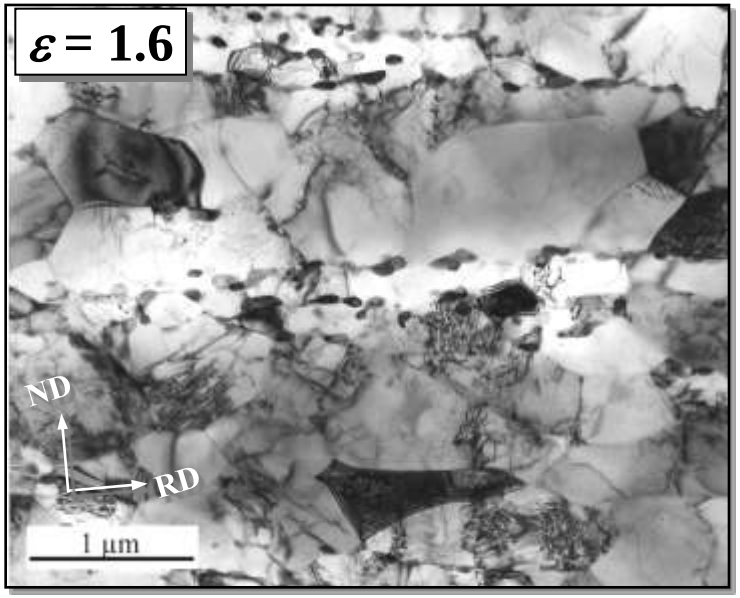

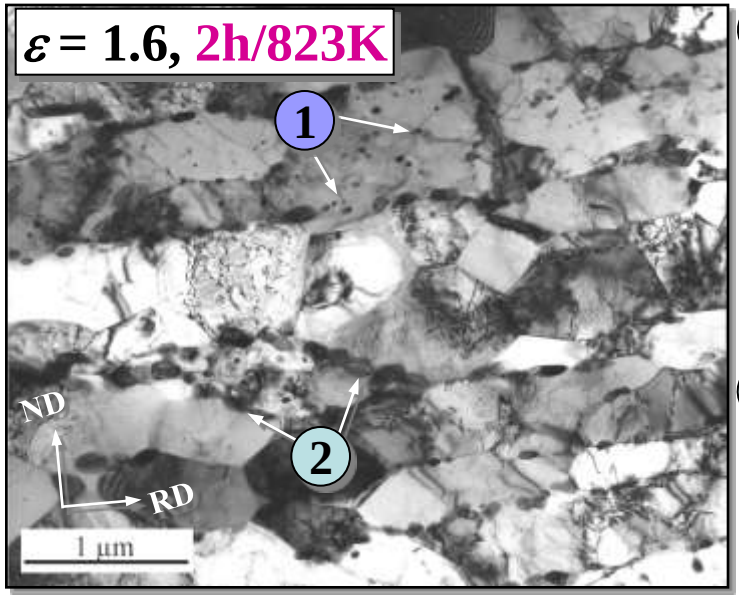

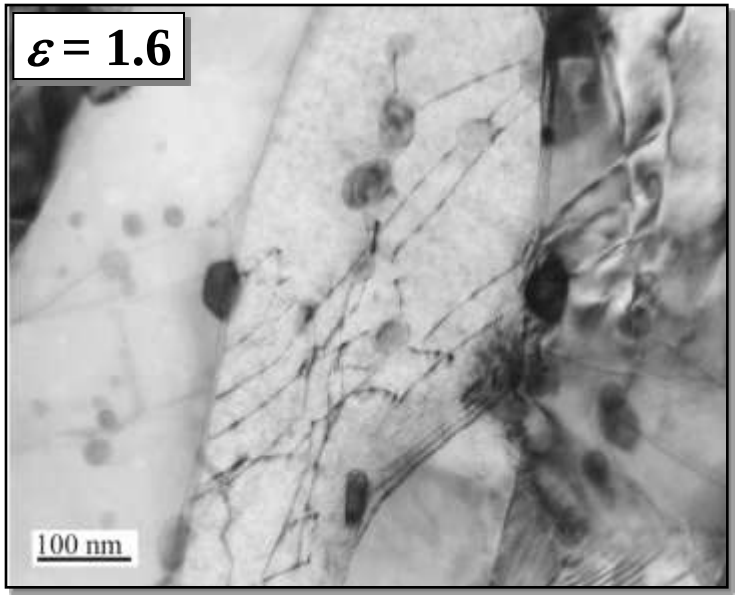

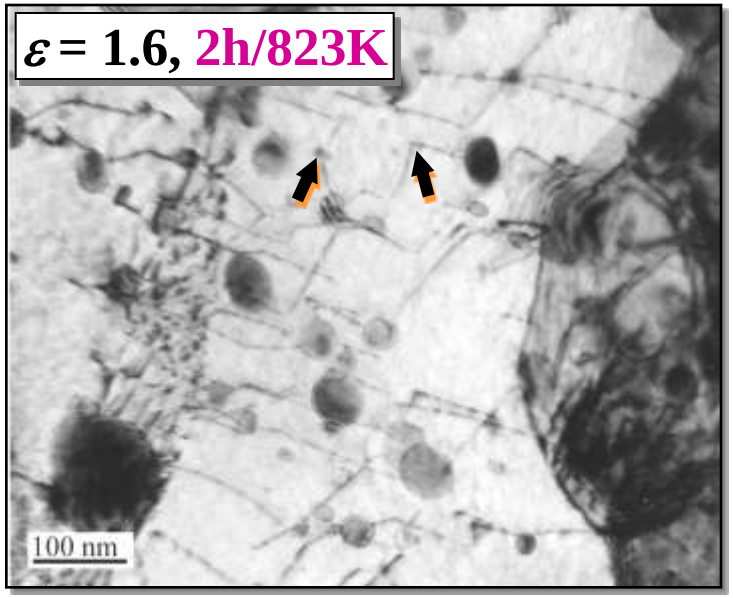

1 Fine cementite particles **(5-90 nm)** inside ferrite grains

2 Coarse cementite particles **(90-350 nm)** at ferrite grain boundaries

Dislocations pinned by cementite particles

Outline Part I (UFG ferrite+cementite)

- Concept
- Physical simulation of processing
- Microstructure and microstructure evolution
- **Impact tests (Effect of microstructure)**
- Effect of C
- Effect of Mn
- Conclusions Part I

Impact test specimen

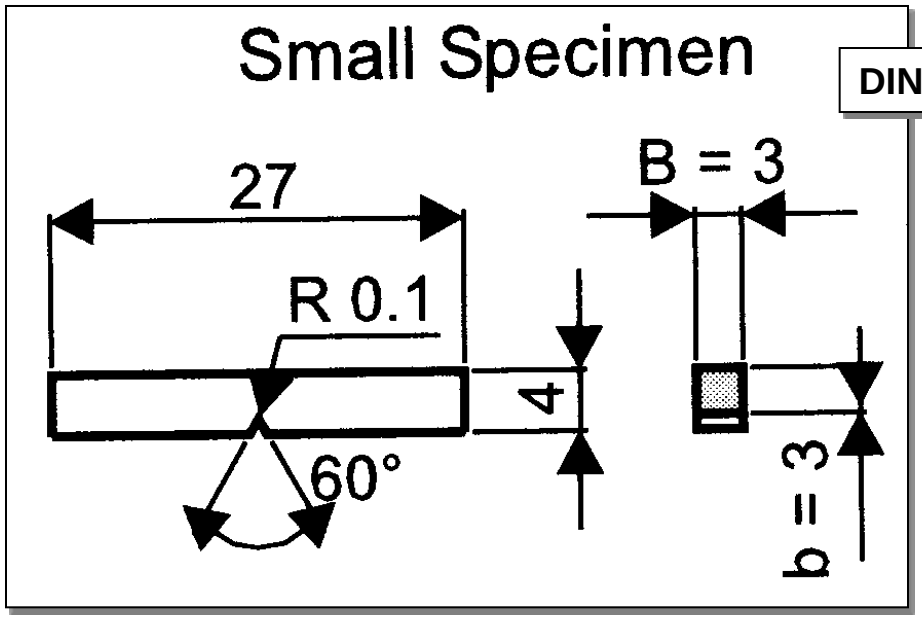

Used in this study

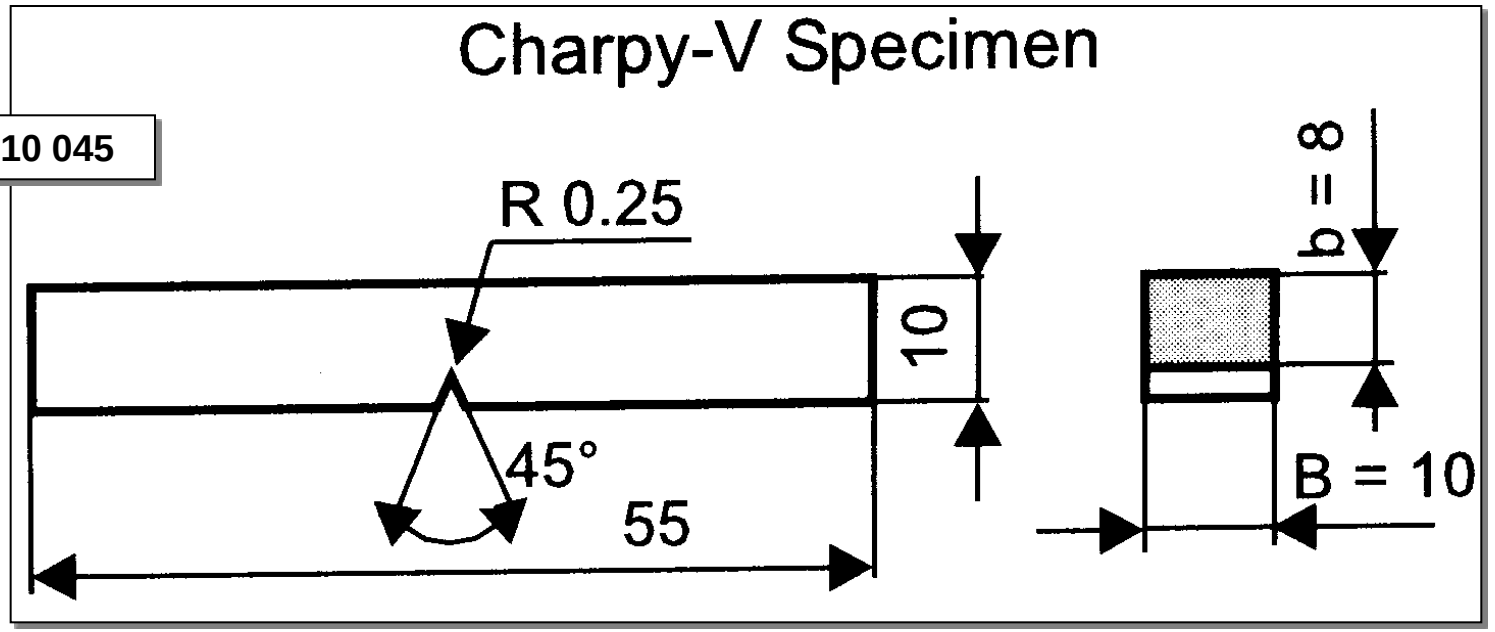

Impact tests: Comparison UFG and CP steels

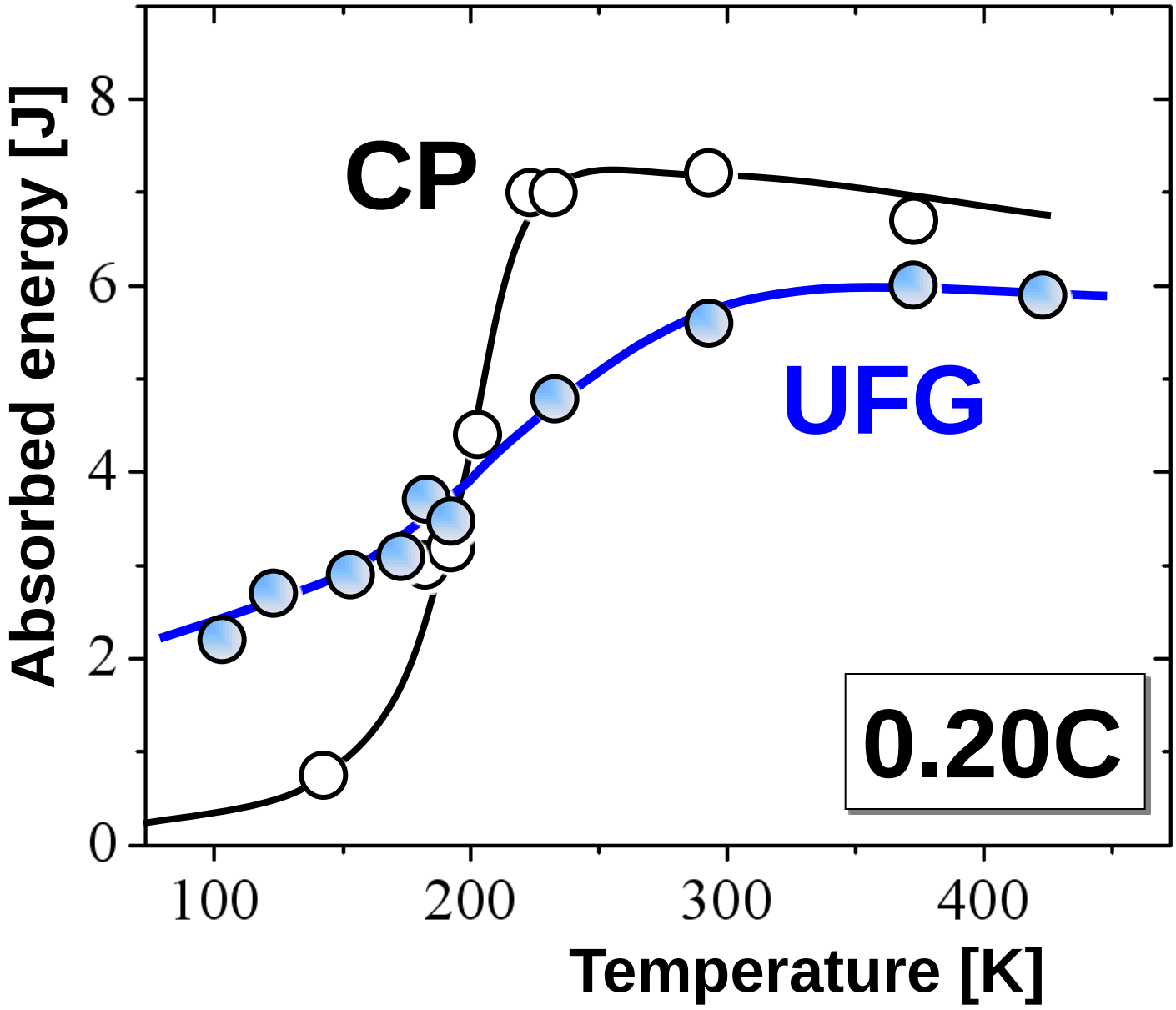

Fracture surfaces of impact specimen

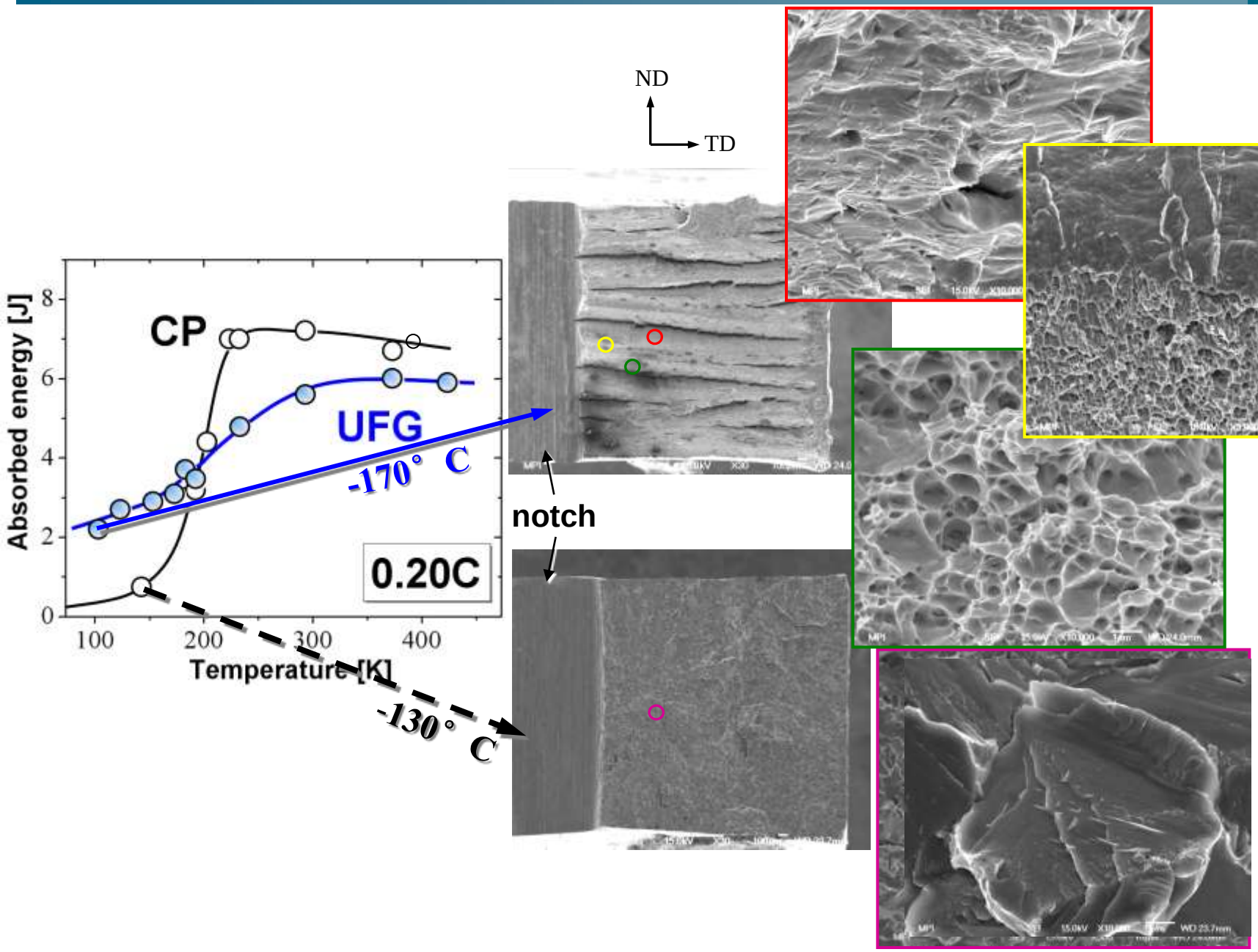

SEM image and ND orientation maps

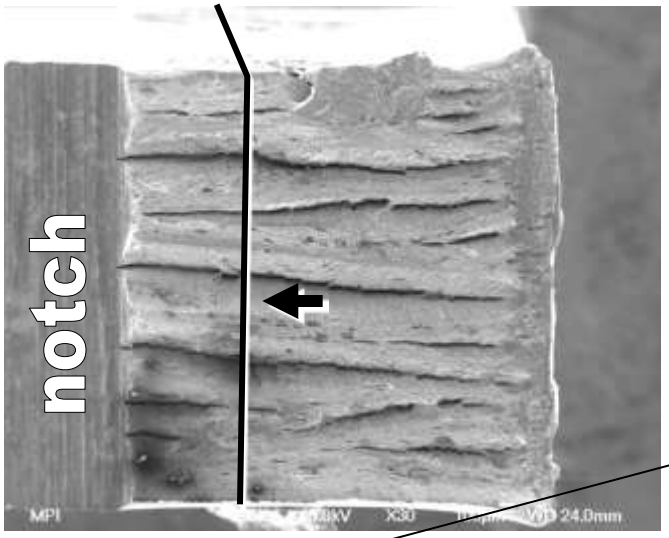

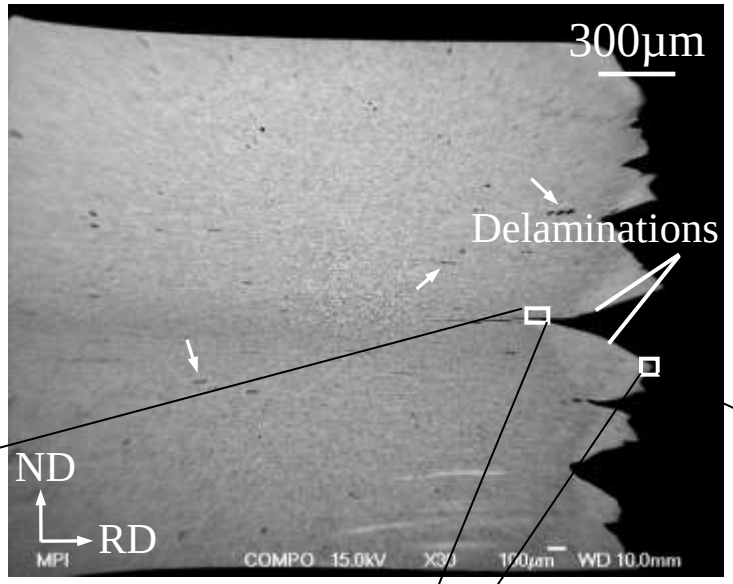

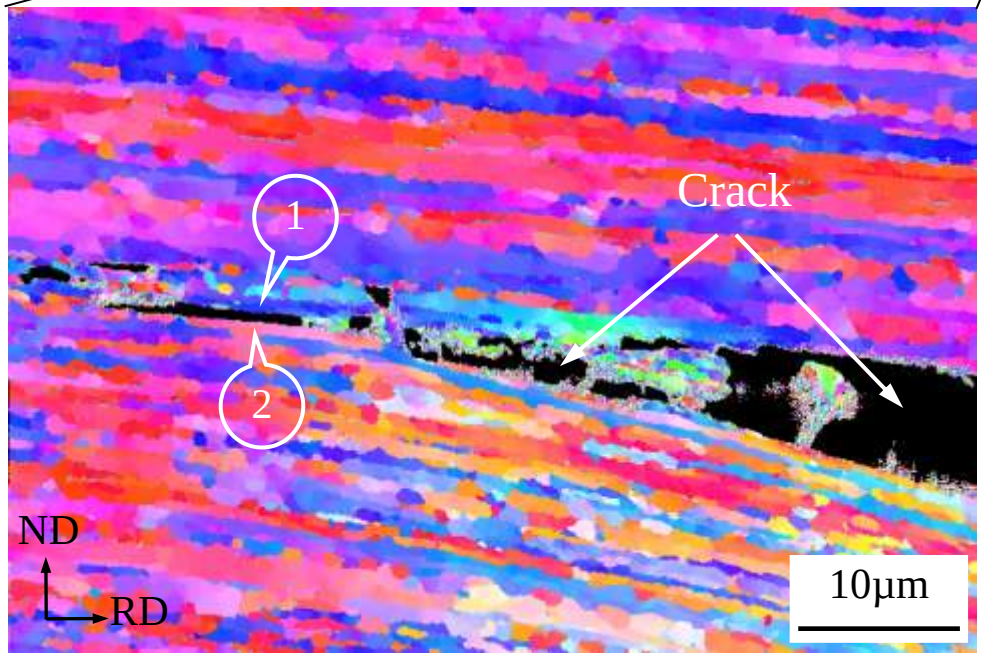

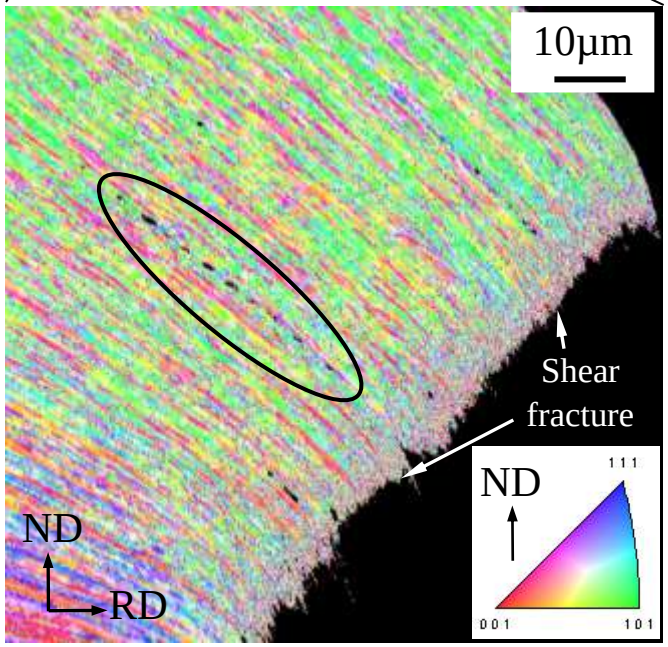

Outline Part I (UFG ferrite+cementite)

- Concept
- Physical simulation of processing
- Microstructure and microstructure evolution
- Impact tests (Effect of microstructure)
- **Effect of C**
- Effect of Mn
- Conclusions Part I

Grain size

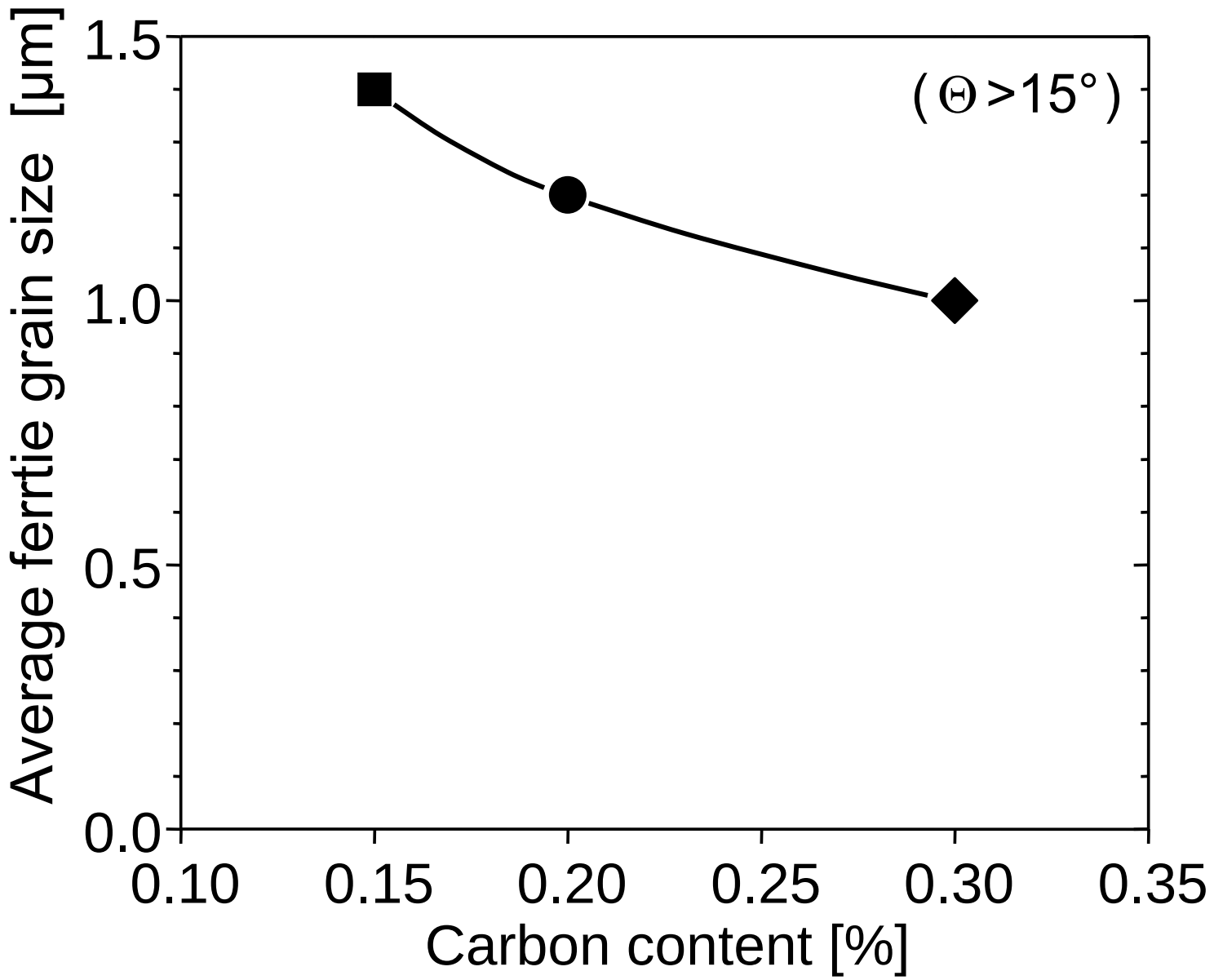
Average ferrtie grain size [μm]
1.5
1.0
0.5
0.0
(Θ>15°)
0.10
0.15
0.20
0.25
0.30
0.35
Carbon content [%]

Tensile ductility

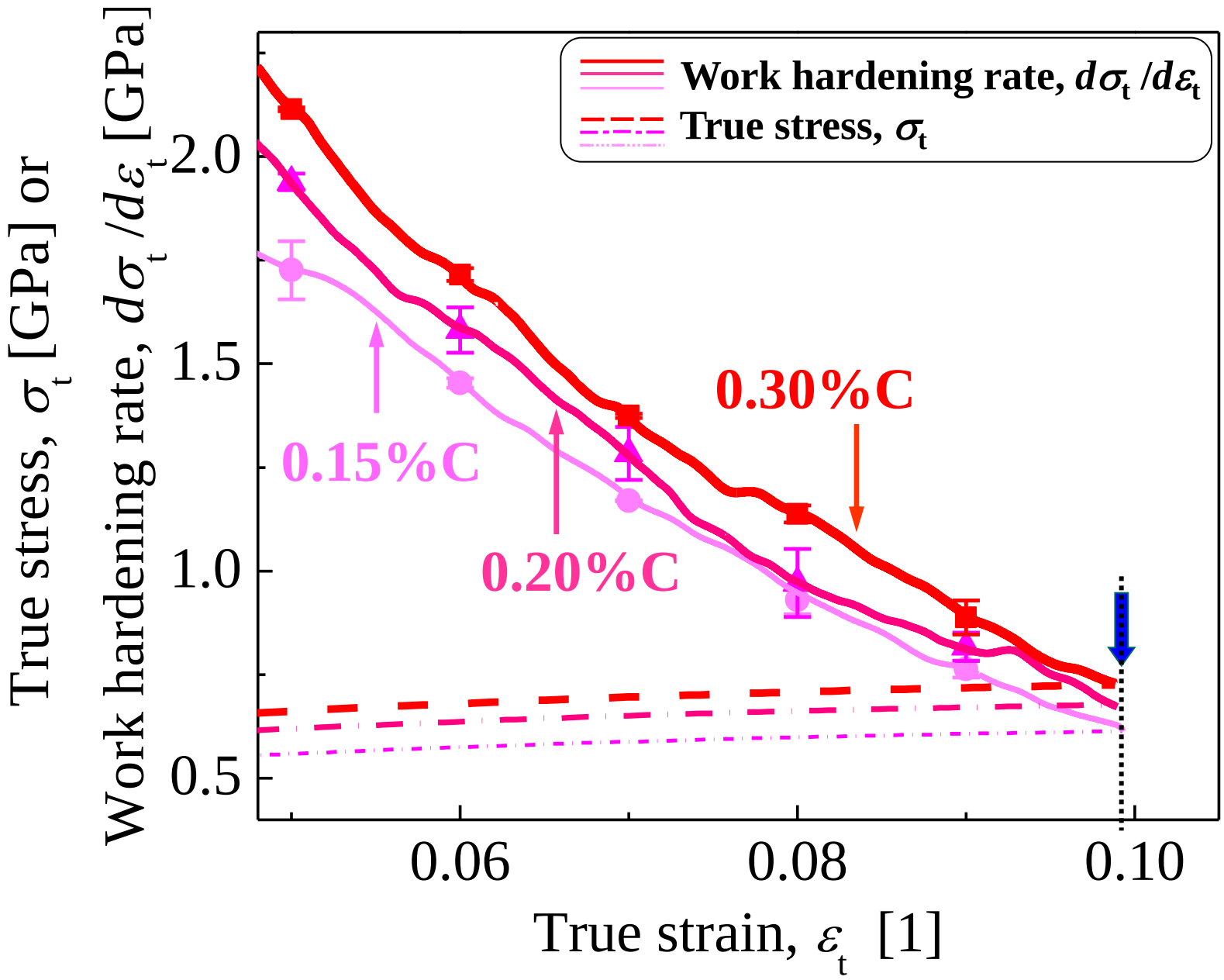

Effect of carbon content on tensile properties

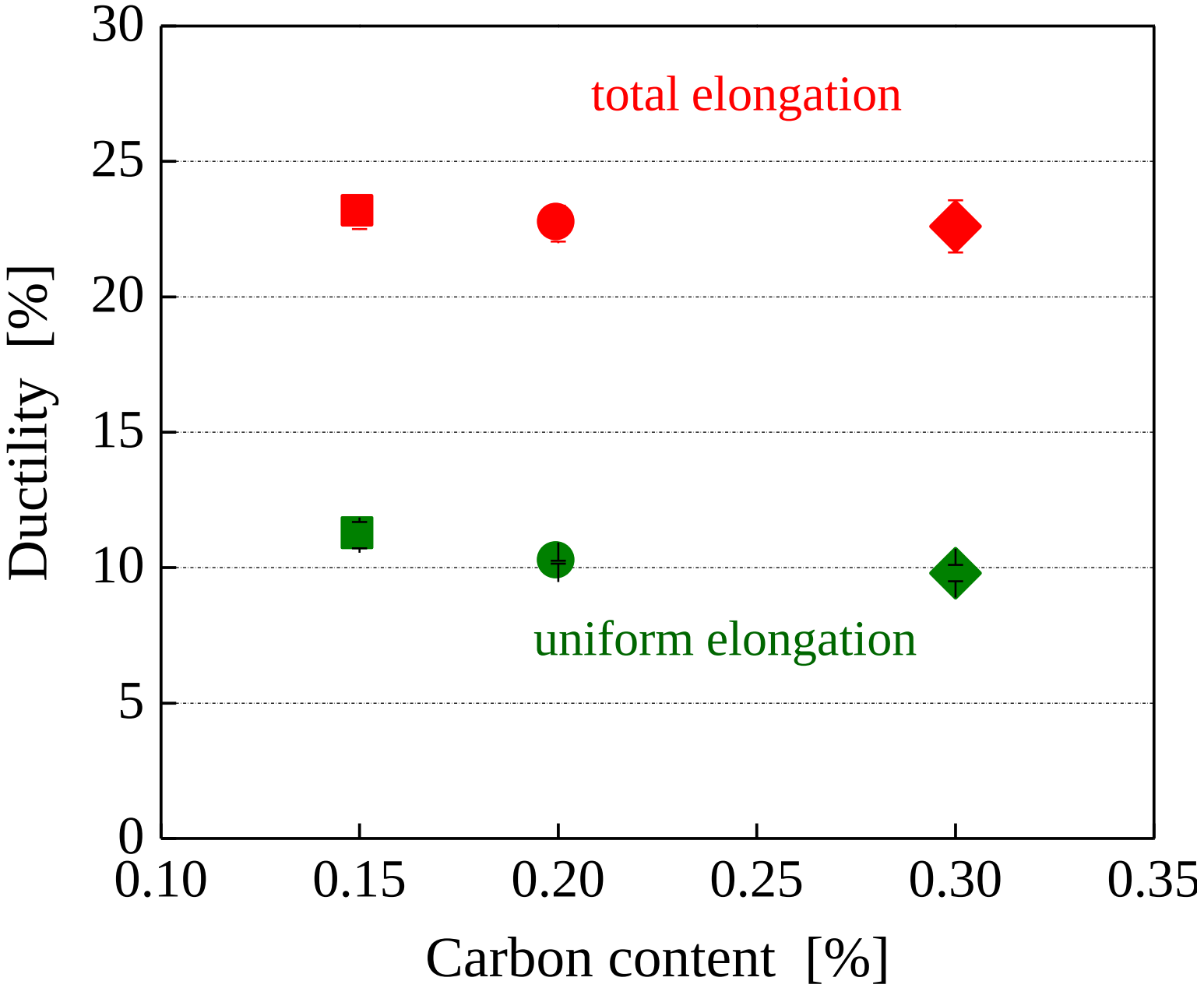

Effect of carbon content on tensile properties

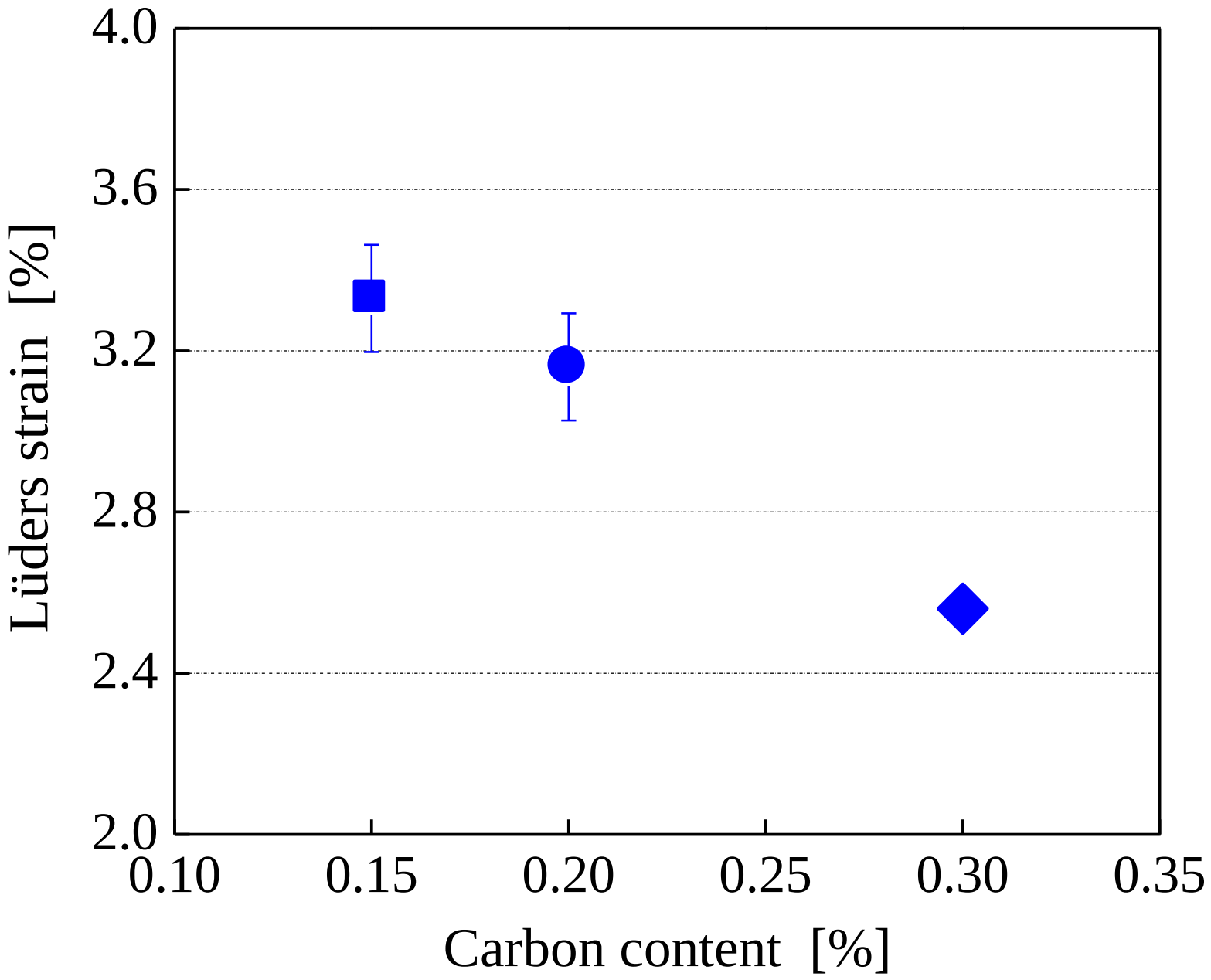

Outline Part I (UFG ferrite+cementite)

- Concept
- Physical simulation of processing
- Microstructure and microstructure evolution
- Impact tests (Effect of microstructure)
- Effect of C
- **Effect of Mn**
- Conclusions Part I

Grain size

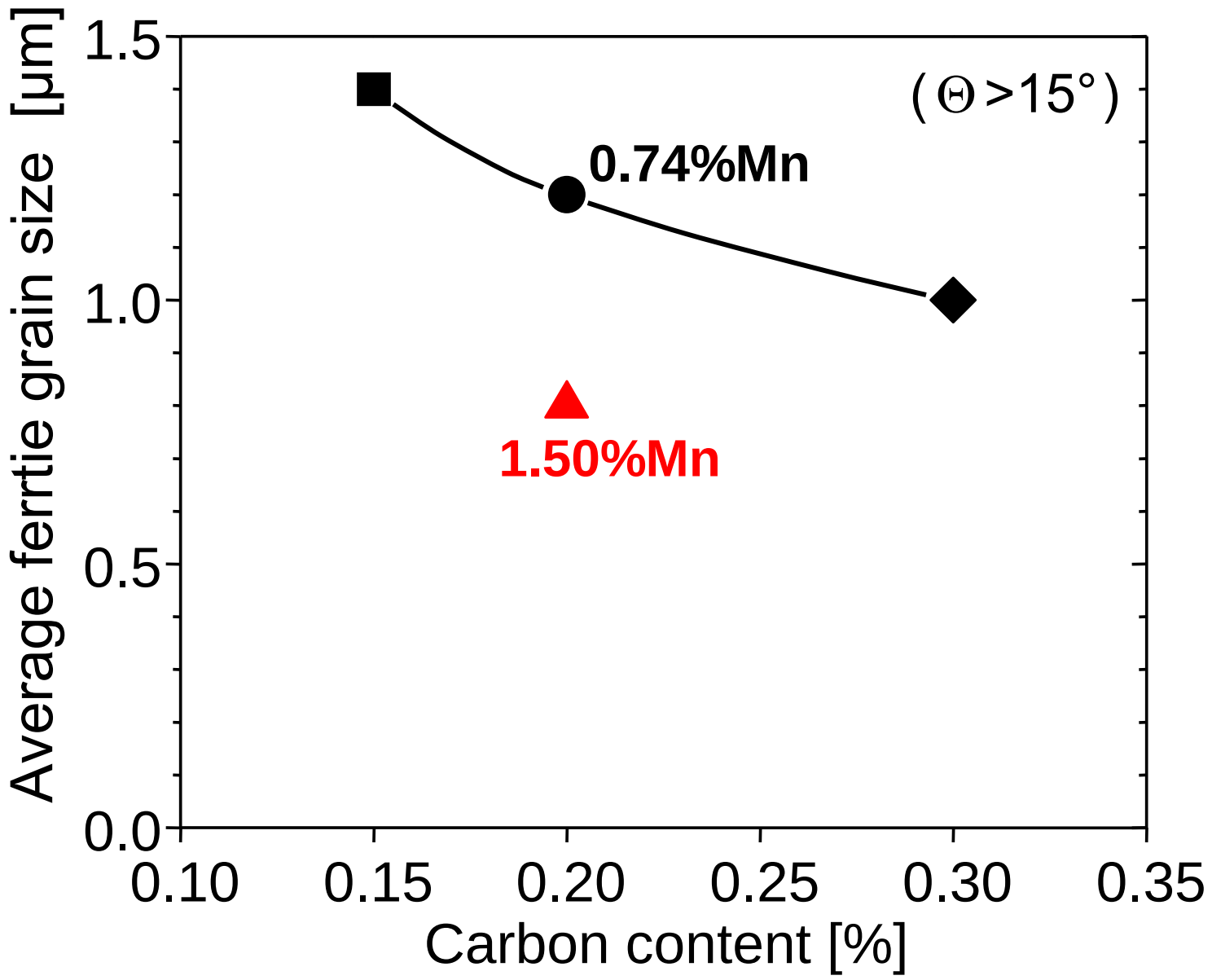
Average ferrtie grain size [μm]
1.5
1.0
0.5
0.0
0.10
0.15
0.20
0.25
0.30
0.35
Carbon content [%]
(Θ>15°)
0.74%Mn
1.50%Mn

Manganese and Carbon Distribution

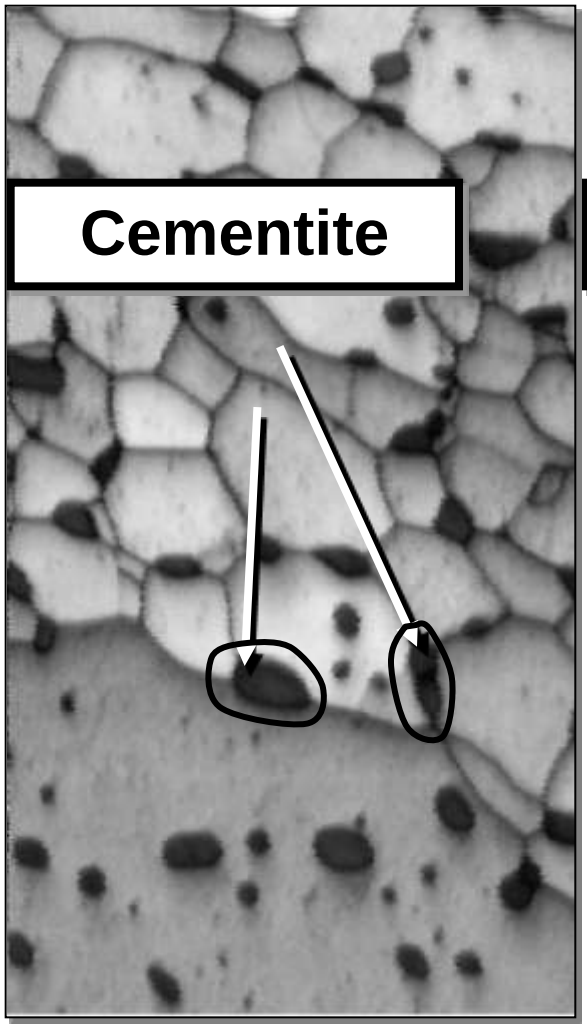

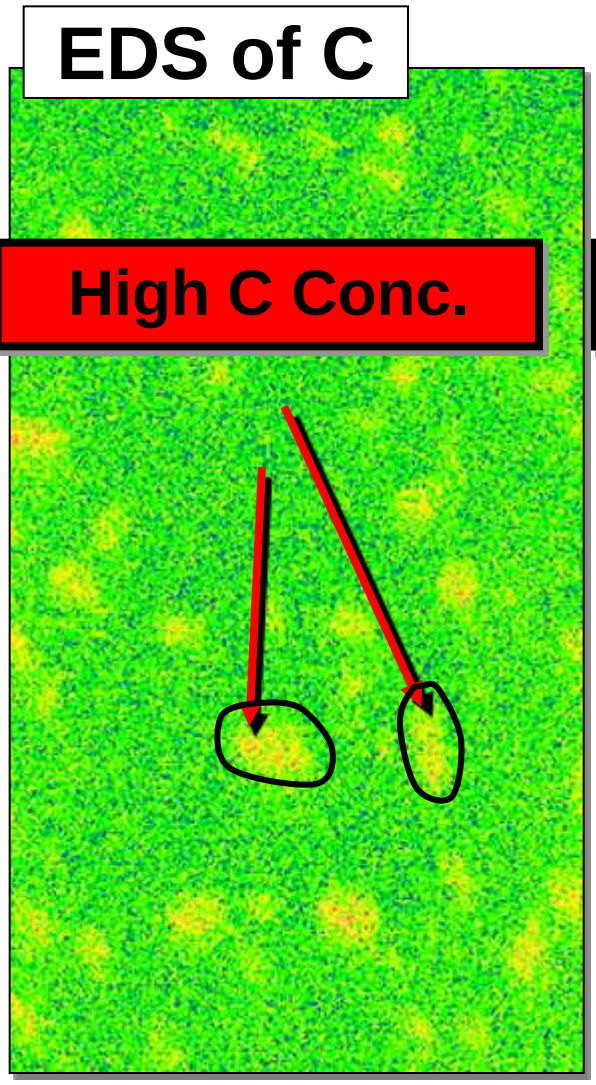

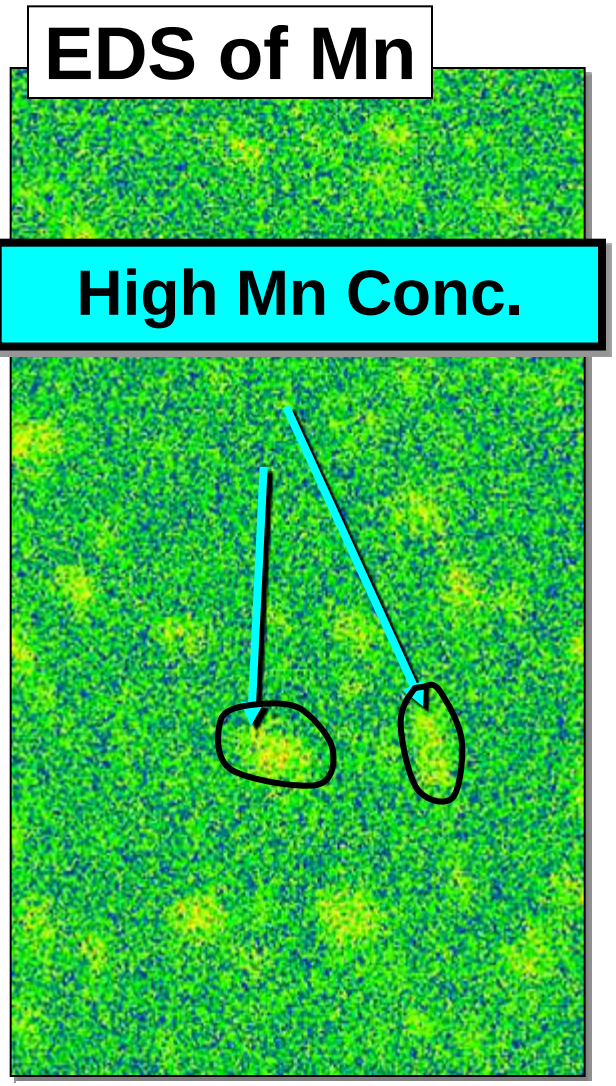

Manganese Distribution

EDS (TEM): matrix and cementite particles

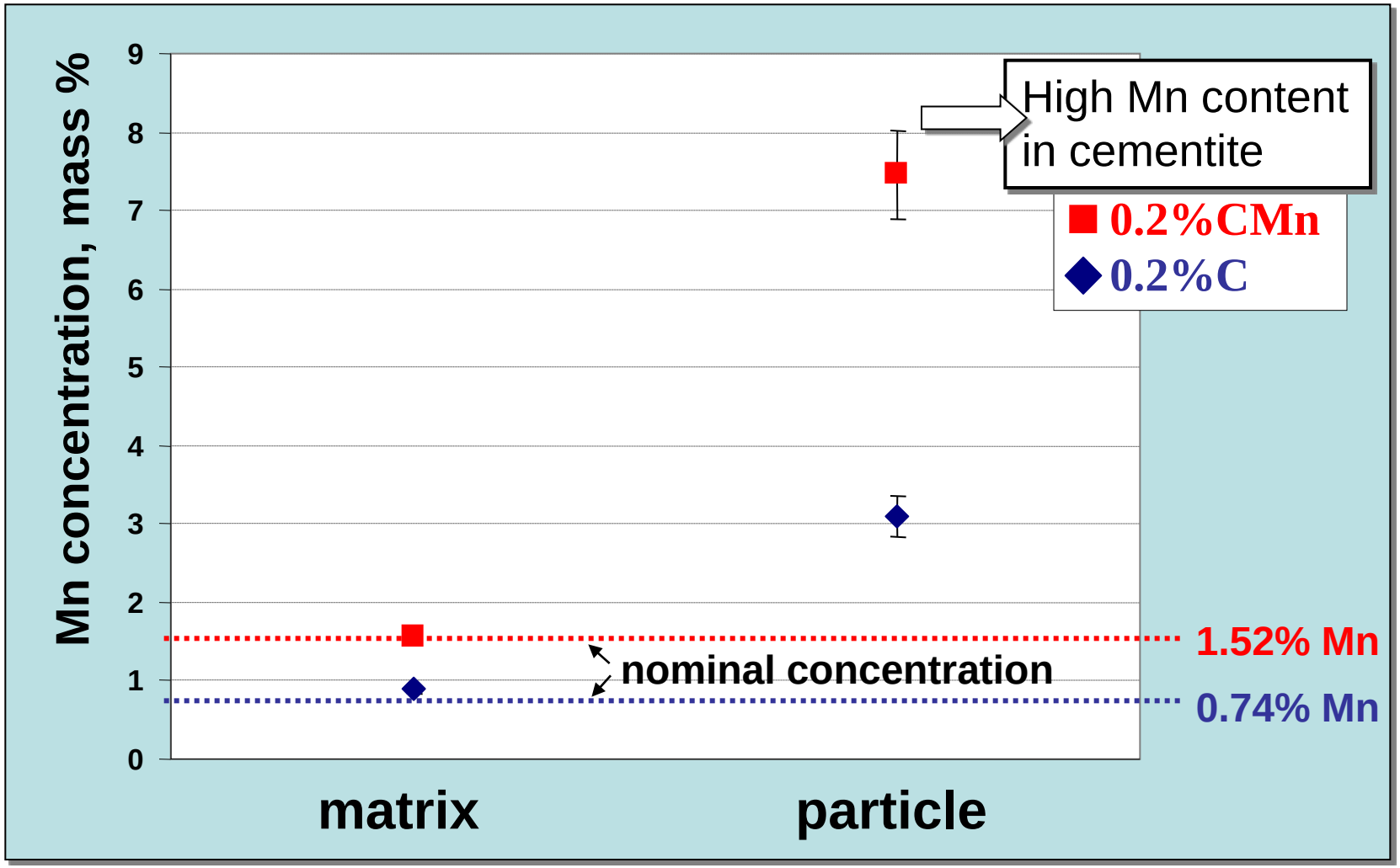

Effect of annealing on microstructure

before annealing

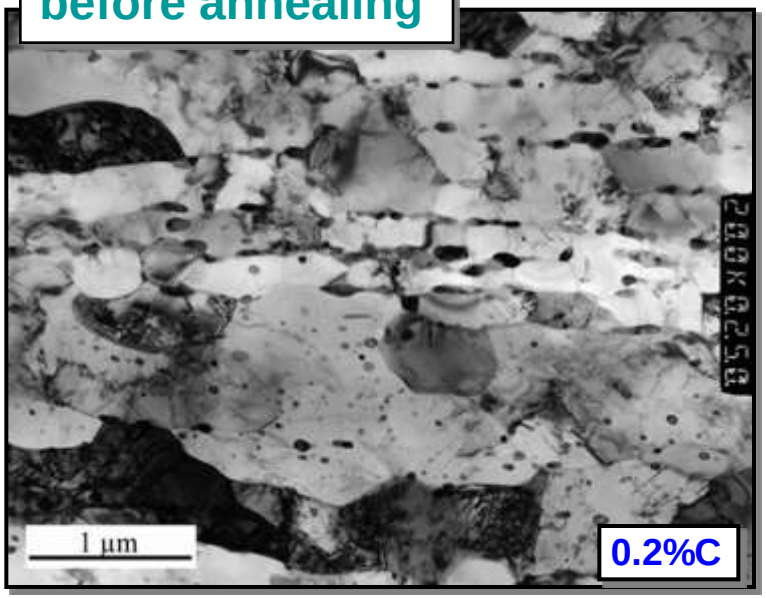

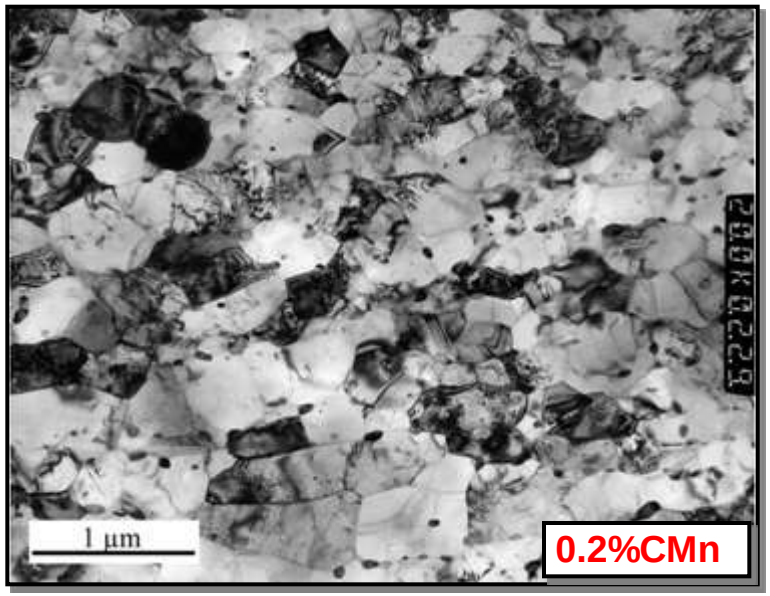

finer cementite in 0.2%CMn

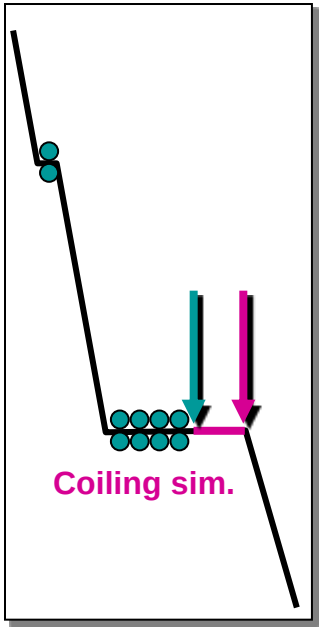

after annealing (coiling sim. 2h/823K)

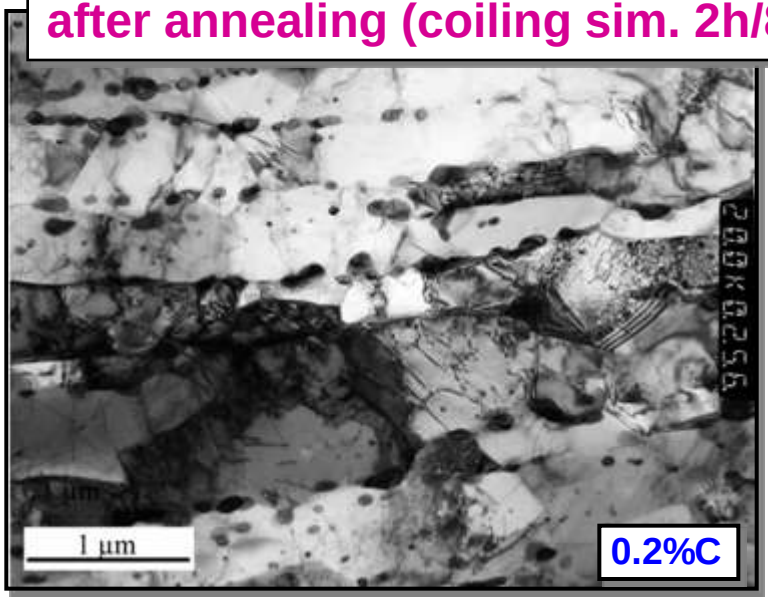

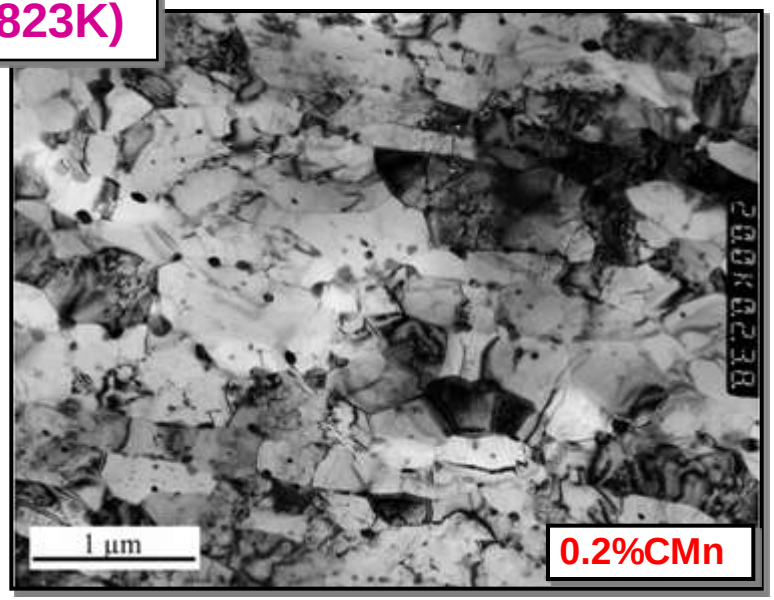

less cementite coarsening during coiling sim. in 0.2C%Mn

Outline Part I (UFG ferrite+cementite)

- Concept
- Physical simulation of processing
- Microstructure and microstructure evolution
- Impact tests (Effect of microstructure)
- Effect of C
- Effect of Mn
- **Conclusions Part I**

Conclusions

- **UFG ferrite (1µm) + fine dispersed cementite**

- **Annealing after warm deformation supports cementite spheroidization and equiaxed grain shape**

- **>60% high angle grain boundaries**

- **Ultra grain refinement increases strength and toughness** (transition temp., lower shelf energy)
  Warm deformation: tendency for delamination

- **Increasing C: Cementite increases strain hardening rate and strength**

- **Mn helps to refine ferrite grains and stabilize cementite (Mn enrichment in cementite)**

Part II

UFG Dual-Phase steel

(Ferrite + Martensite)

M. Calcagnotto, D. Ponge, D. Raabe

Outline Part II (UFG Dual Phase-steel)

- **Concept**
- Fabrication of UFG dual phase steels
  - Effect of Mn on microstructure evolution
  - Effect of intercritical annealing parameters
- Conclusions and future work Part II

Concept

- Increase strain hardening rate

  by introducing **martensite**

- Method: **intercritical annealing** of UFG

  steel with ferrite/cementite

Outline Part II (UFG Dual Phase-steel)

- Concept
- **Fabrication of UFG dual phase steels**
  - Effect of Mn on microstructure evolution
  - Effect of intercritical annealing parameters
- Conclusions and future work Part II

Production of UFG F/M DP steels

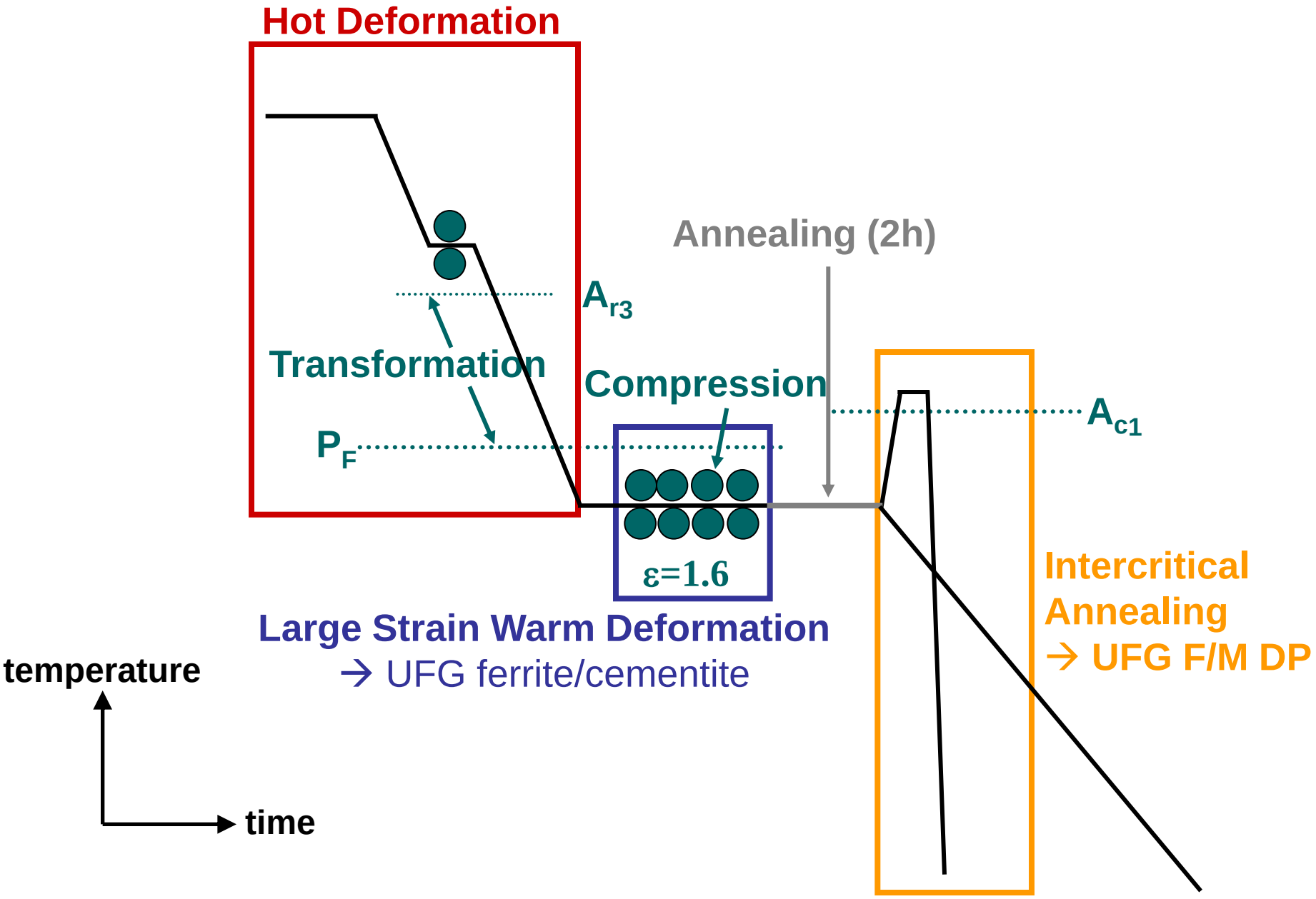

Materials

Compositions, mass%

Steel	Fe	C	Si	Mn	P	S	Al	N
16C	Bal.	0.16	0.27	0.87	0.0021	0.0034	0.037	0.0024
17C-Mn	Bal.	0.17	0.28	1.63	0.0021	0.0038	0.036	0.0025

Dilatometer pretests

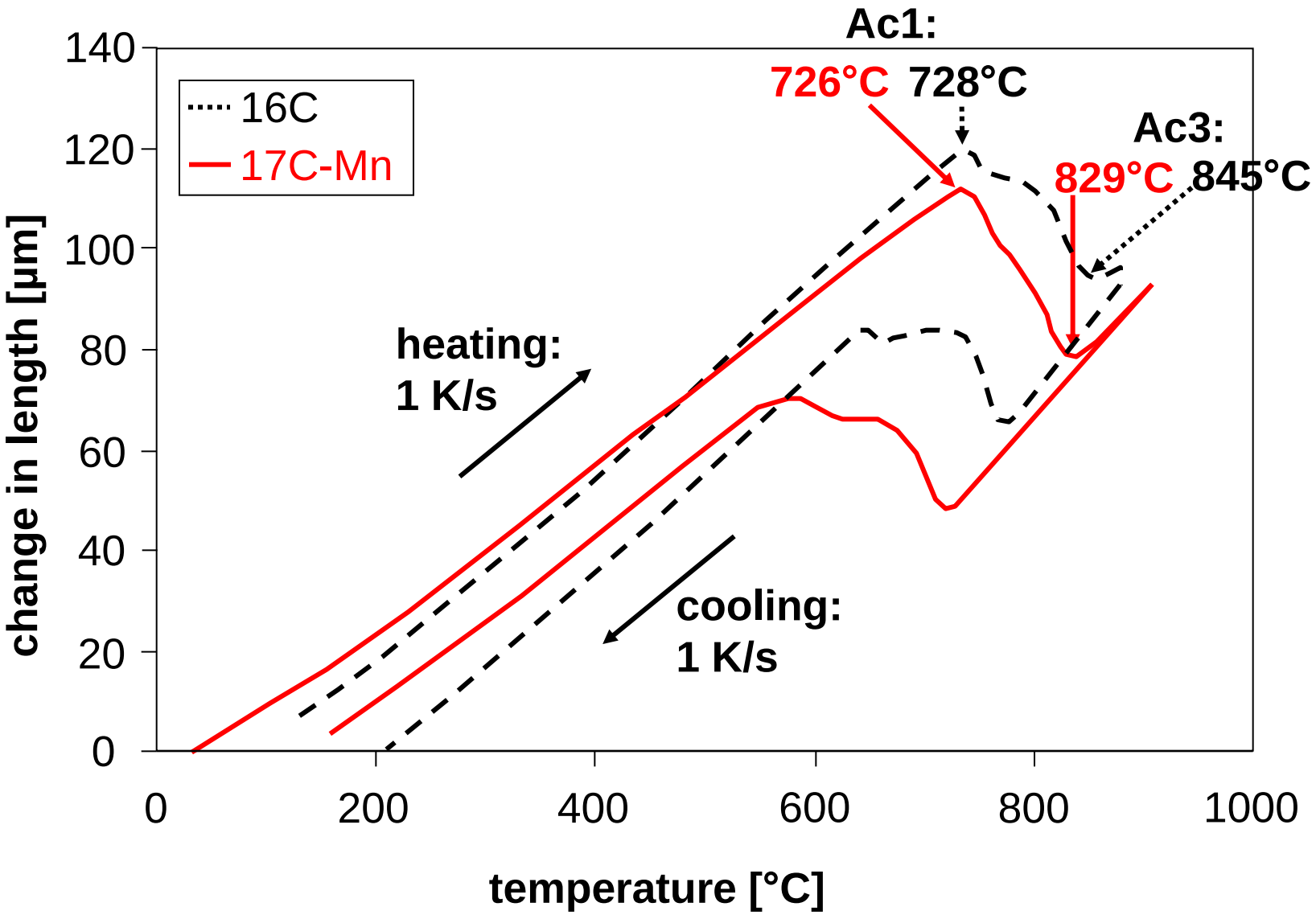

Dilatometer pretests

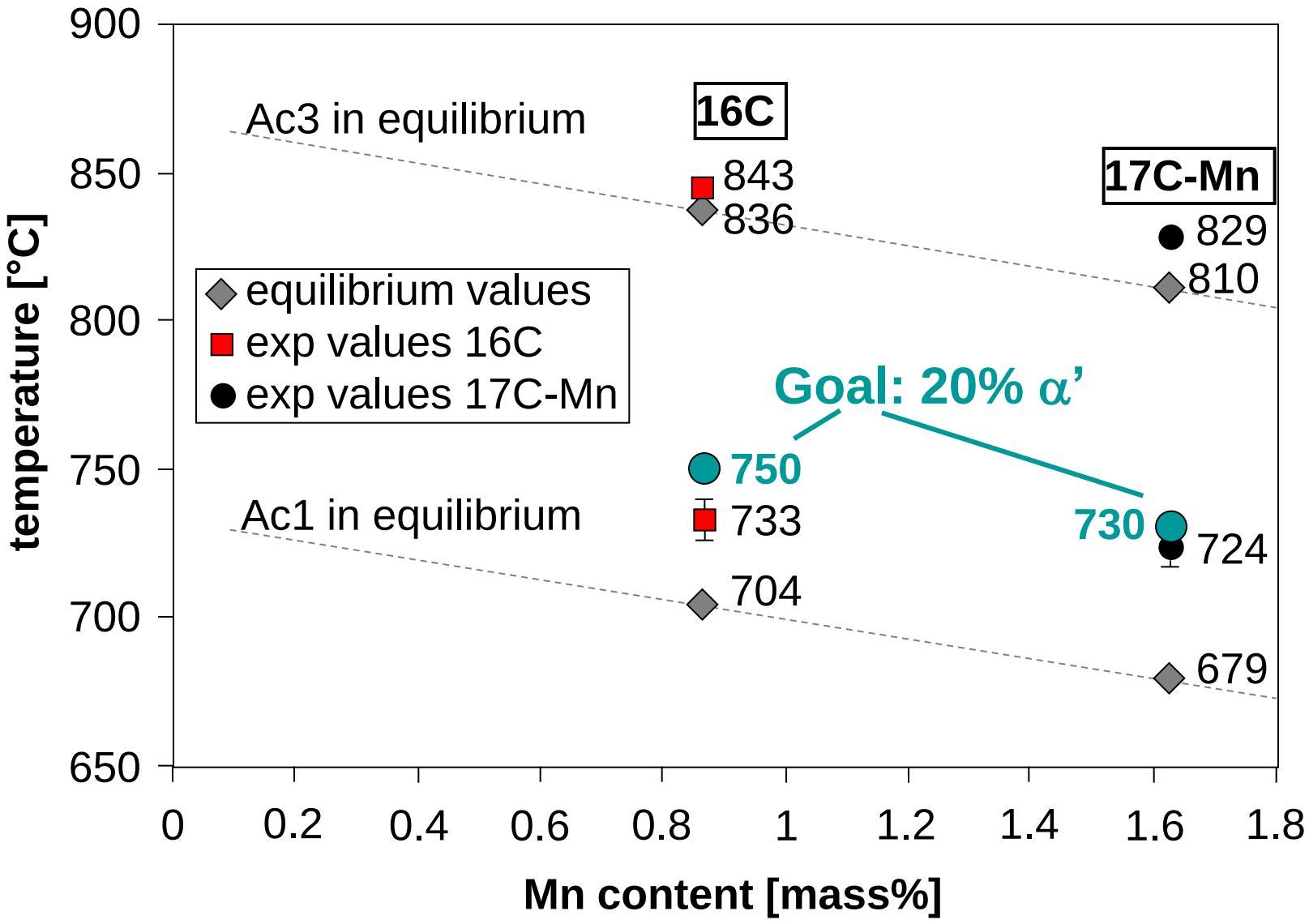

Outline Part II (UFG Dual Phase-steel)

- Concept
- Fabrication of UFG dual phase steels
  - **Effect of Mn on microstructure evolution**
  - Effect of intercritical annealing parameters
- Conclusions and future work Part II

Microstructure after heat treatment, low Mn steel

16C after

warm deformation

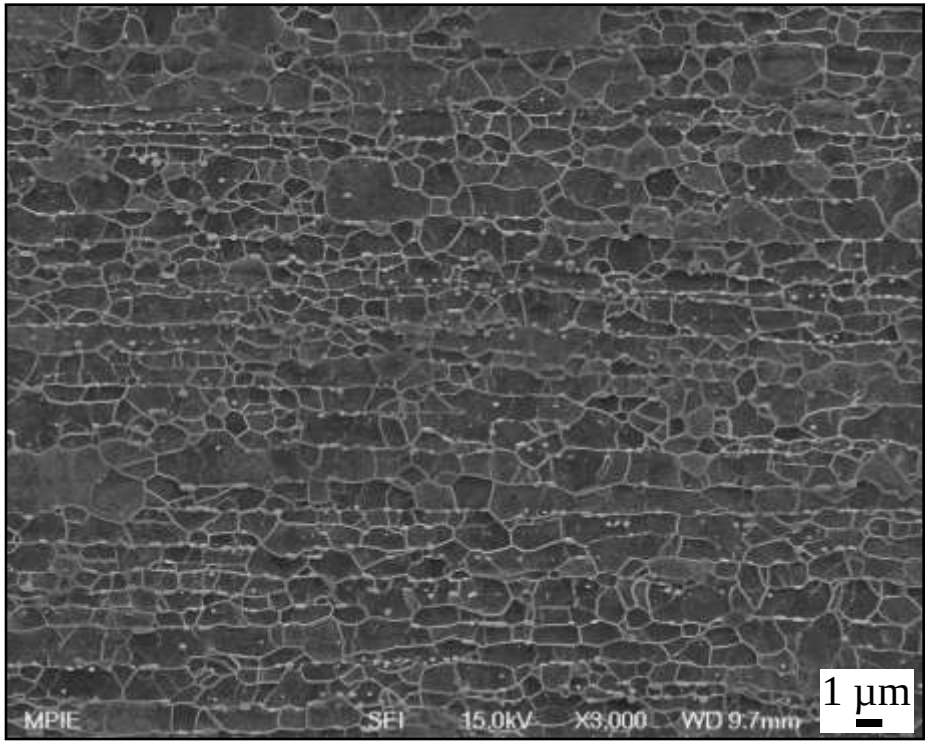

intercritical annealing+H_2 quench*

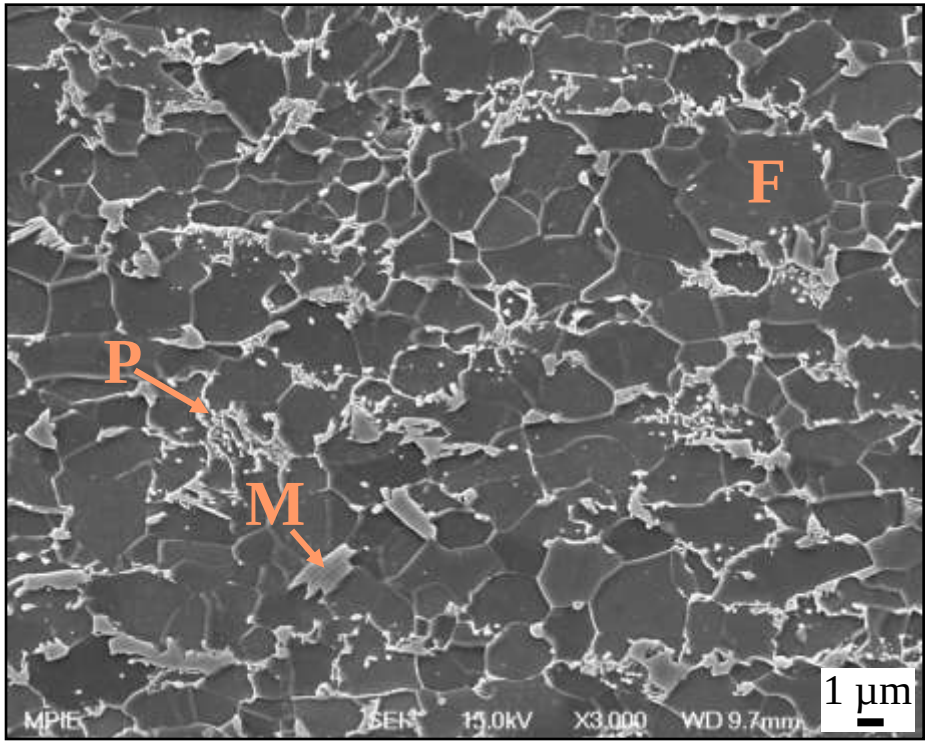

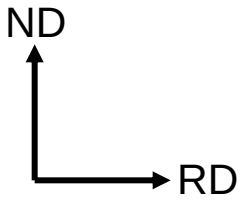

* cooling from 750 to 500°C in 1.8 s (-140 K/s))

Microstructure after heat treatment, high Mn steel

17C-Mn

warm deformation

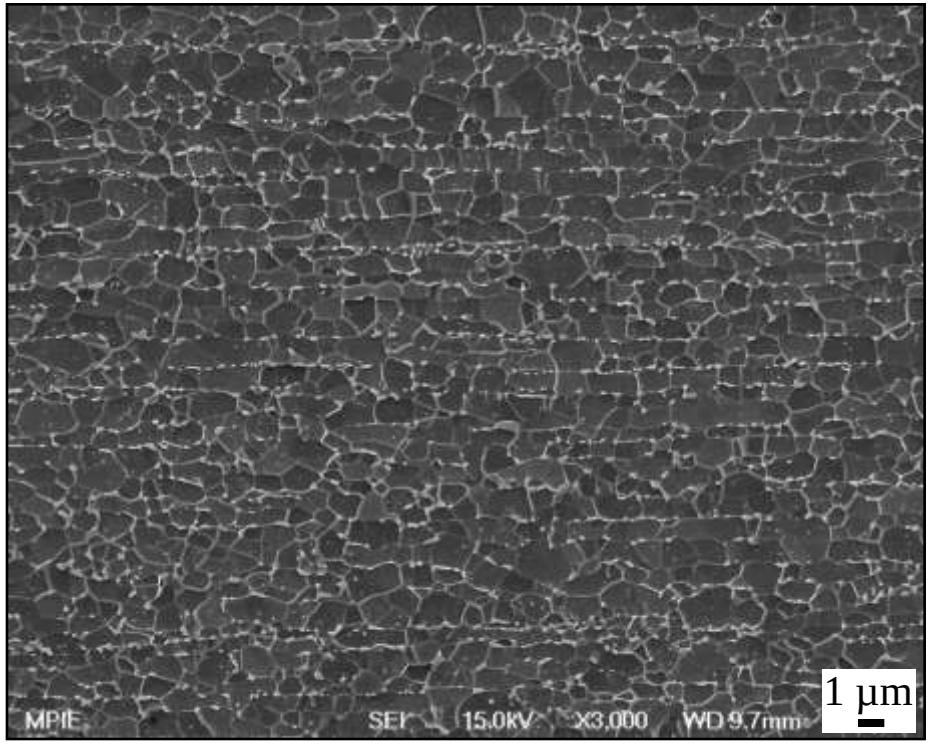

intercritical annealing+H_2 quench*

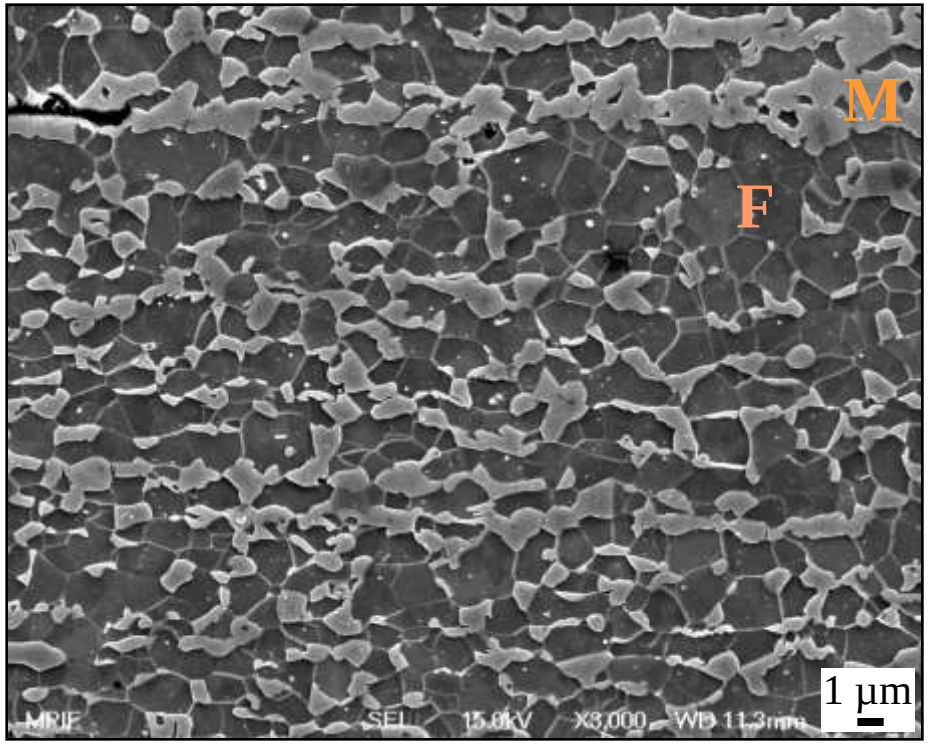

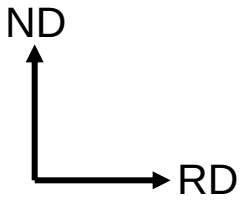

* cooling from 730 to 500°C in 1.6 s (-140 K/s))

Mn enrichment in martensite in 17C-Mn steel

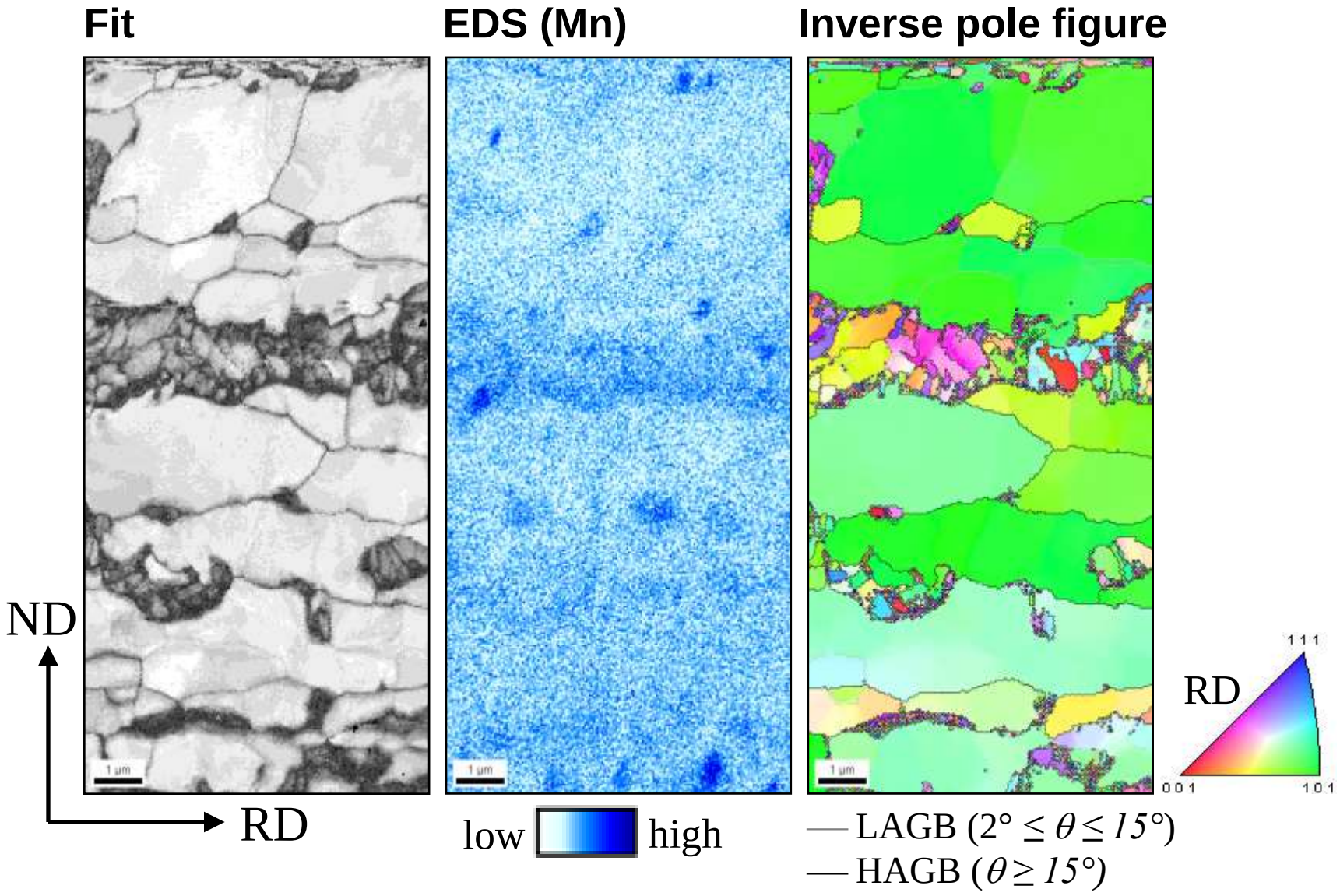

Outline Part II (UFG Dual Phase-steel)

- Concept
- Fabrication of UFG dual phase steels
  - Effect of Mn on microstructure evolution
  - **Effect of intercritical annealing parameters**
- Conclusions and future work Part II

Influence of holding time on microstructure

17C-Mn **holding time**

+20 K/s to 730°C, **held for 2 s**

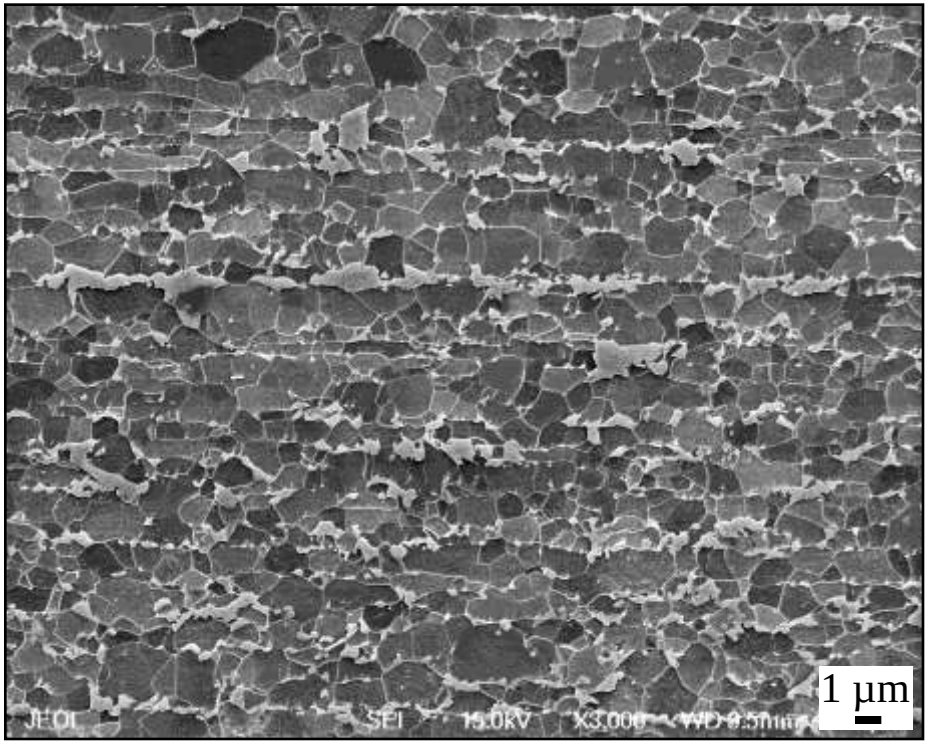

martensite: 8.5%, ferrite MLI: 1.6 µm

+20 K/s to 730°C, **held for 10 min**

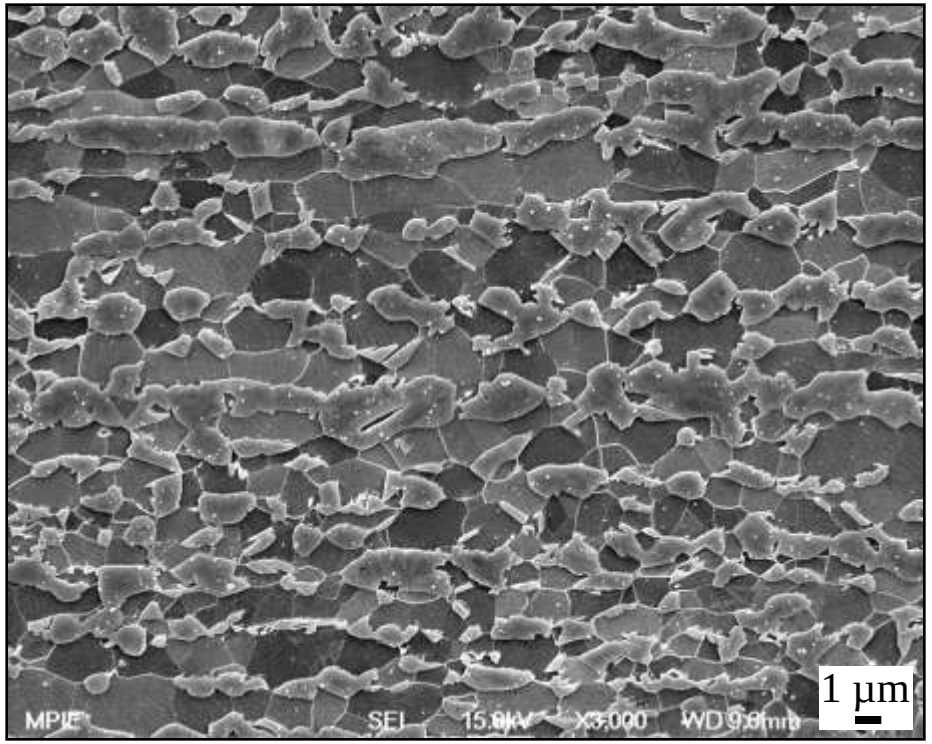

martensite: 41%, ferrite MLI: 1.8 µm

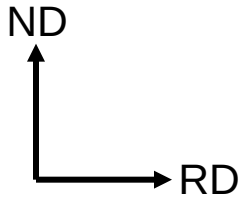

Influence of heating rate on microstructure

17C-Mn **heating rate**

+0.25 K/s to 730°C, held for 1 min

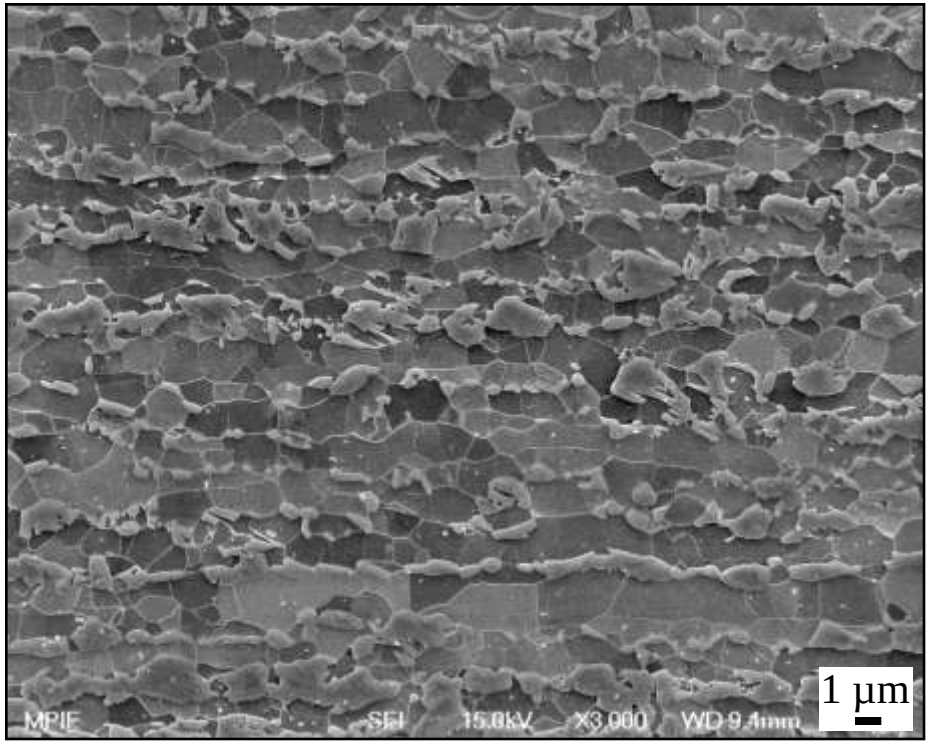

martensite: 23.4%, ferrite MLI: 1.12 µm

+100 K/s to 730°C, held for 1 min

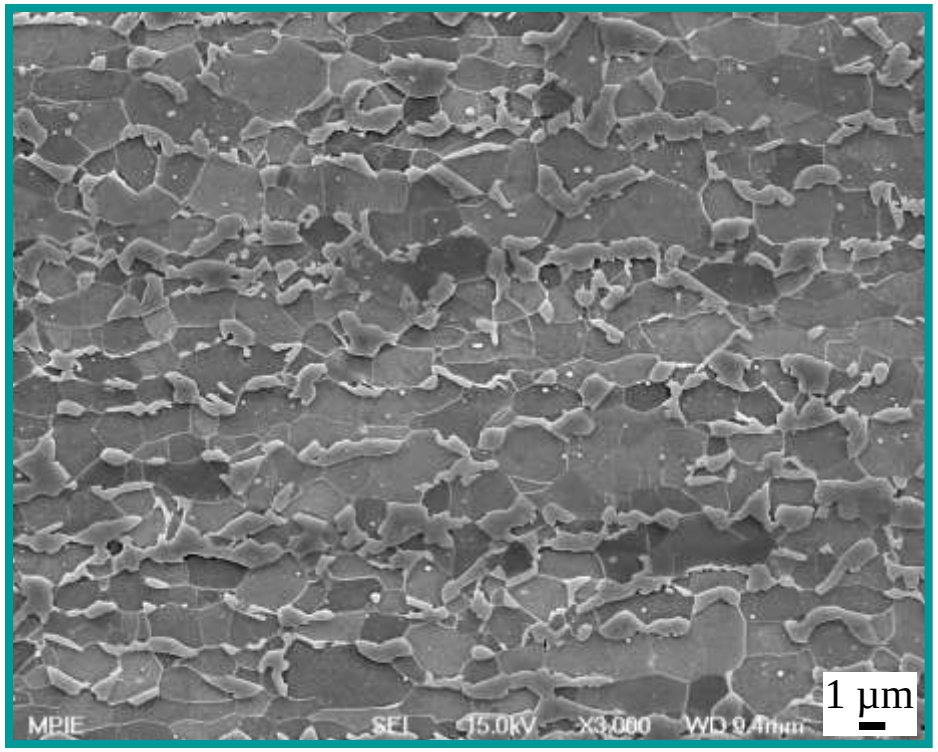

martensite: 24.5%, ferrite MLI: 0.98 µm

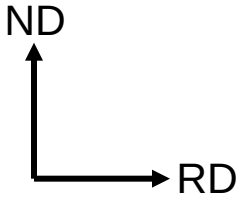

Final heat treatment

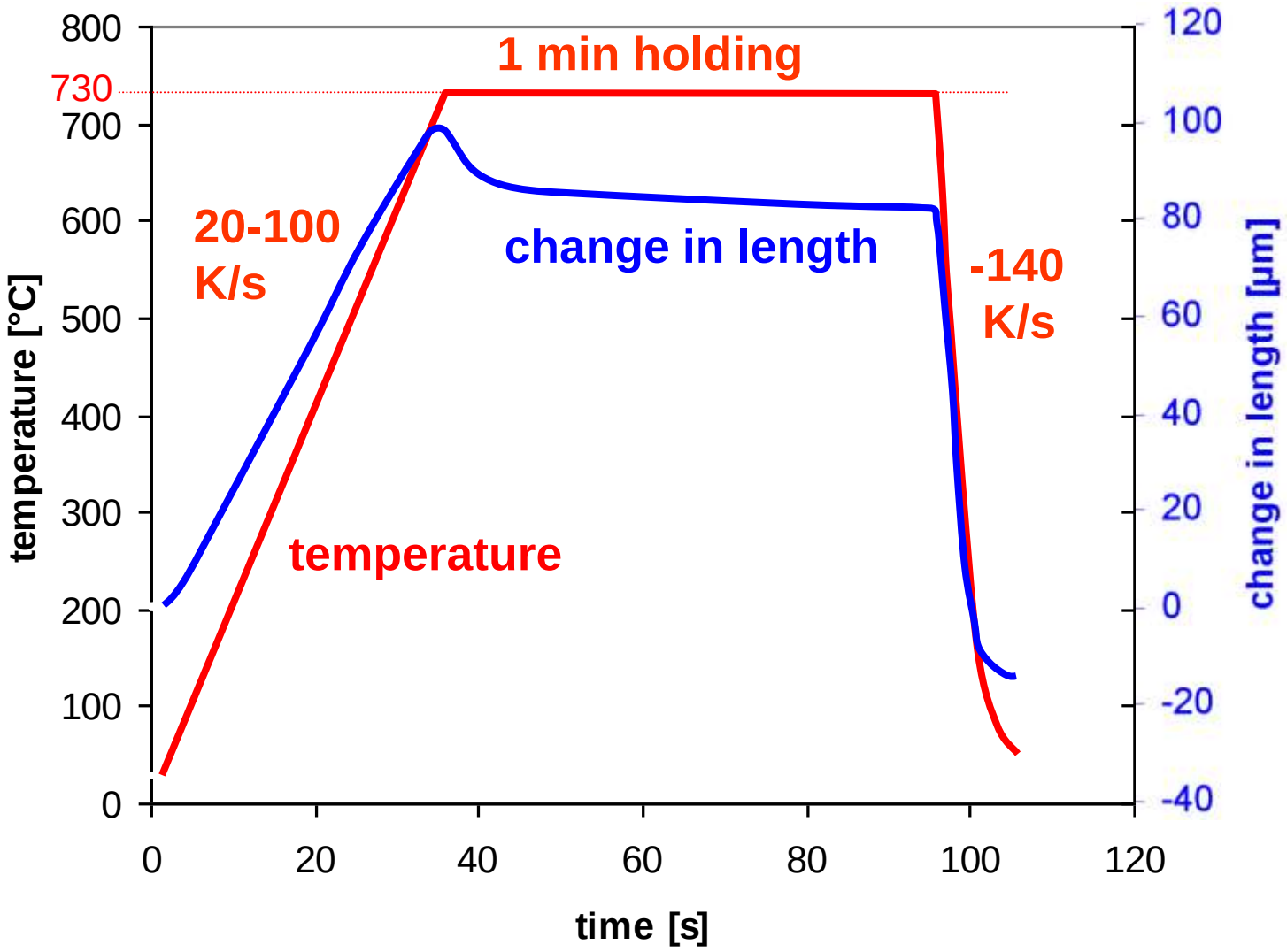

Grain boundary character distribution

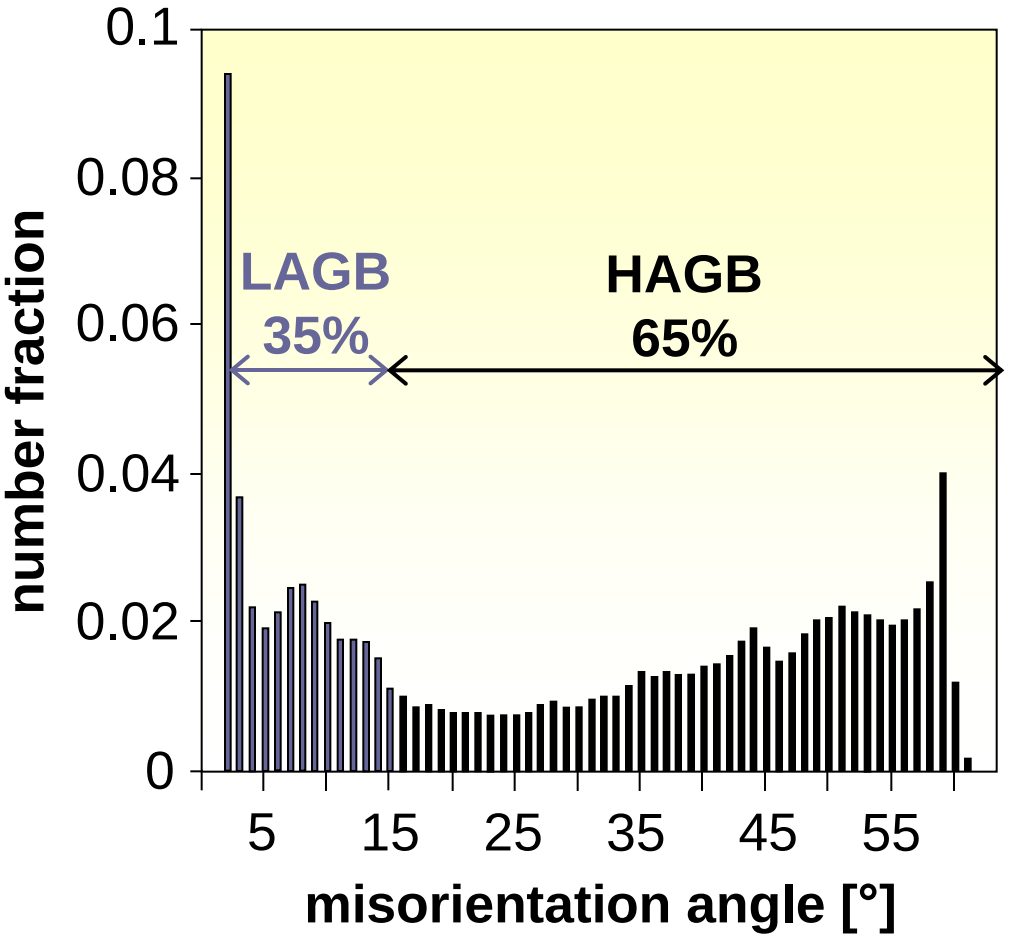

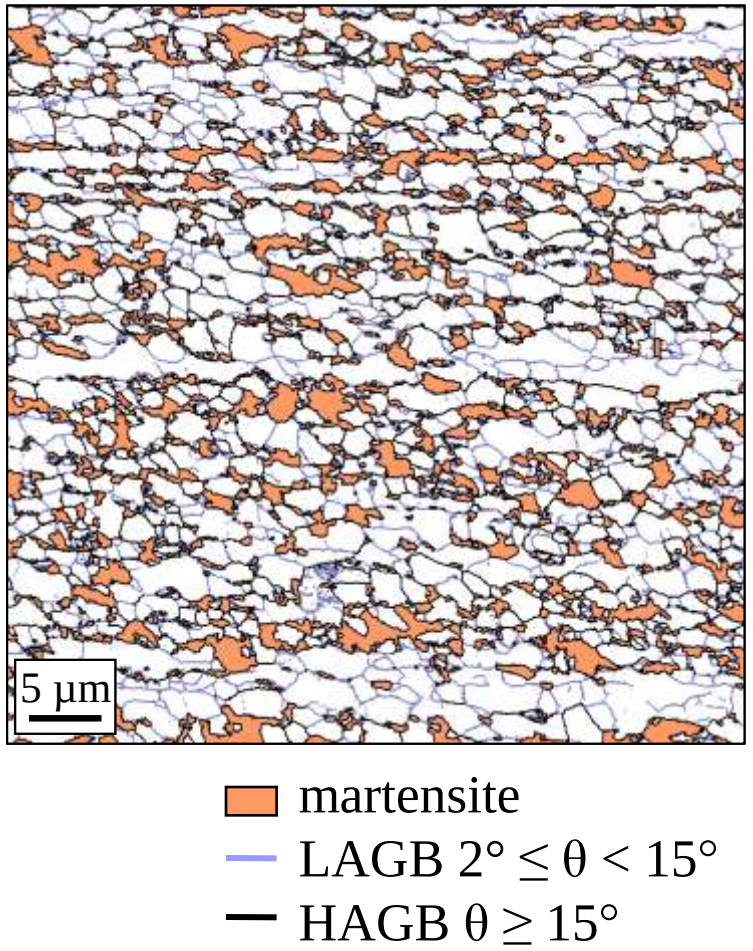

Retained austenite

Phase map

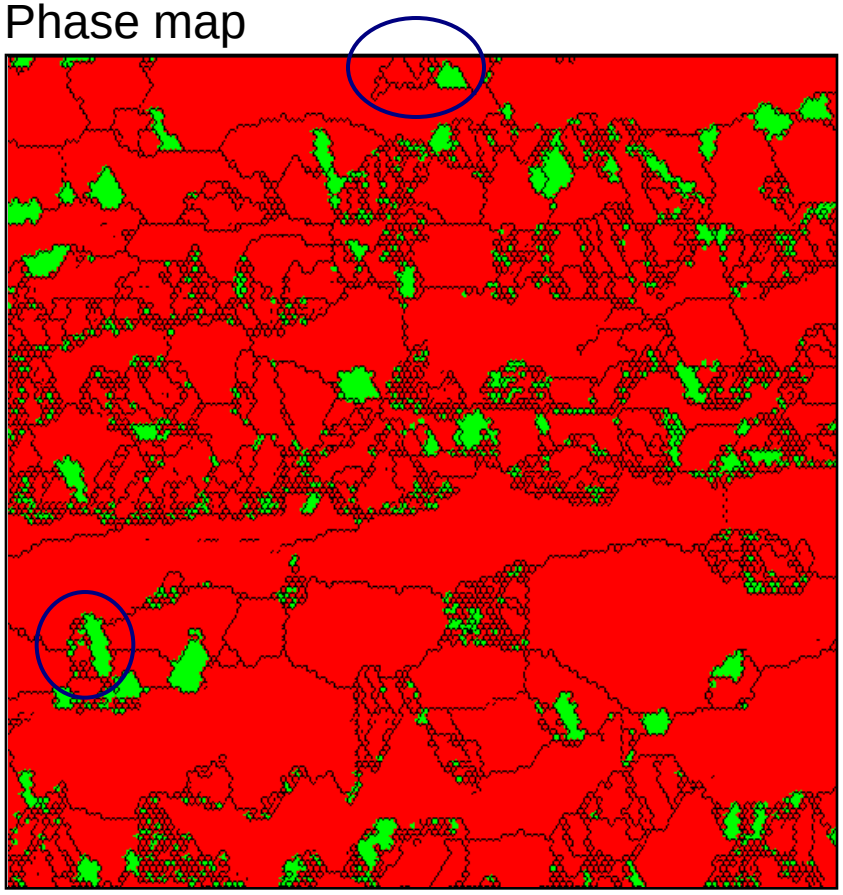

Phase	Total Fraction	Partition Fraction
Iron - Alpha	0.941	0.941
Iron - Gamma	0.059	0.059

Fit map

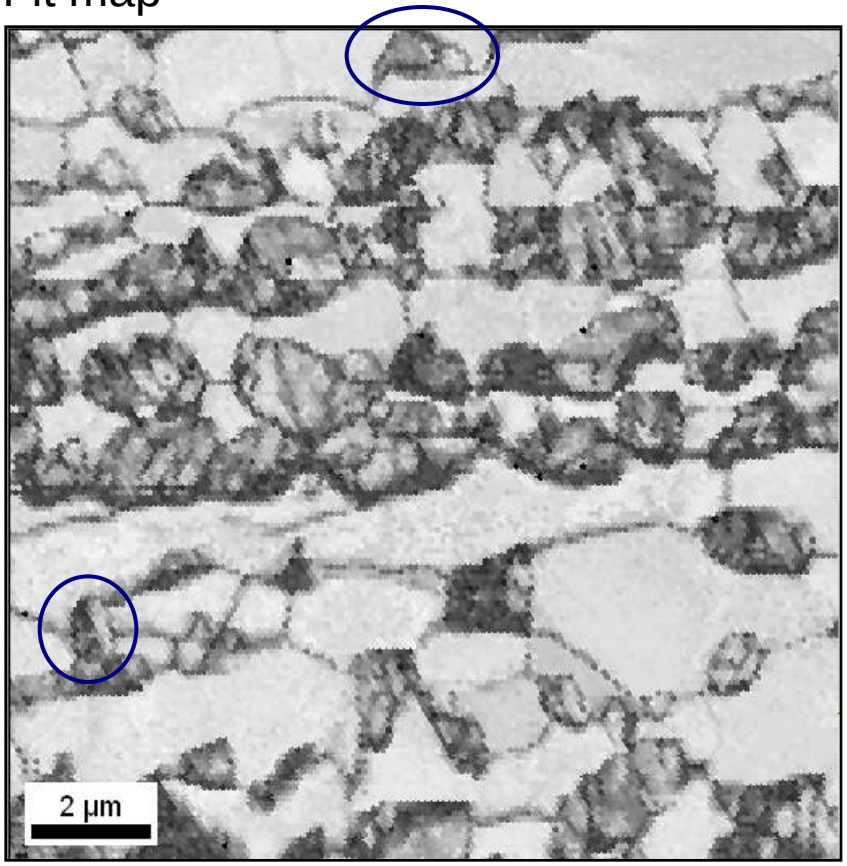

Outline Part II (UFG Dual Phase-steel)

- Concept
- Fabrication of UFG dual phase steels
  - Effect of Mn on microstructure evolution
  - Effect of intercritical annealing parameters
- **Conclusions and future work Part II**

Conclusions and future work

Conclusions

- Large strain warm deformation + intercritical annealing is efficient to produce an UFG DP steel.
- Higher Mn content beneficial: higher Mn enrichment in cementite and austenite: higher hardenability
- Ferrite grain size largely stable during intercritical annealing (rarely sensitive to intercritical heating rate and holding time)

Future work

- determination of mechanical properties
- investigation of fracture behaviour and damage mechanisms

Effect of carbon content on tensile properties

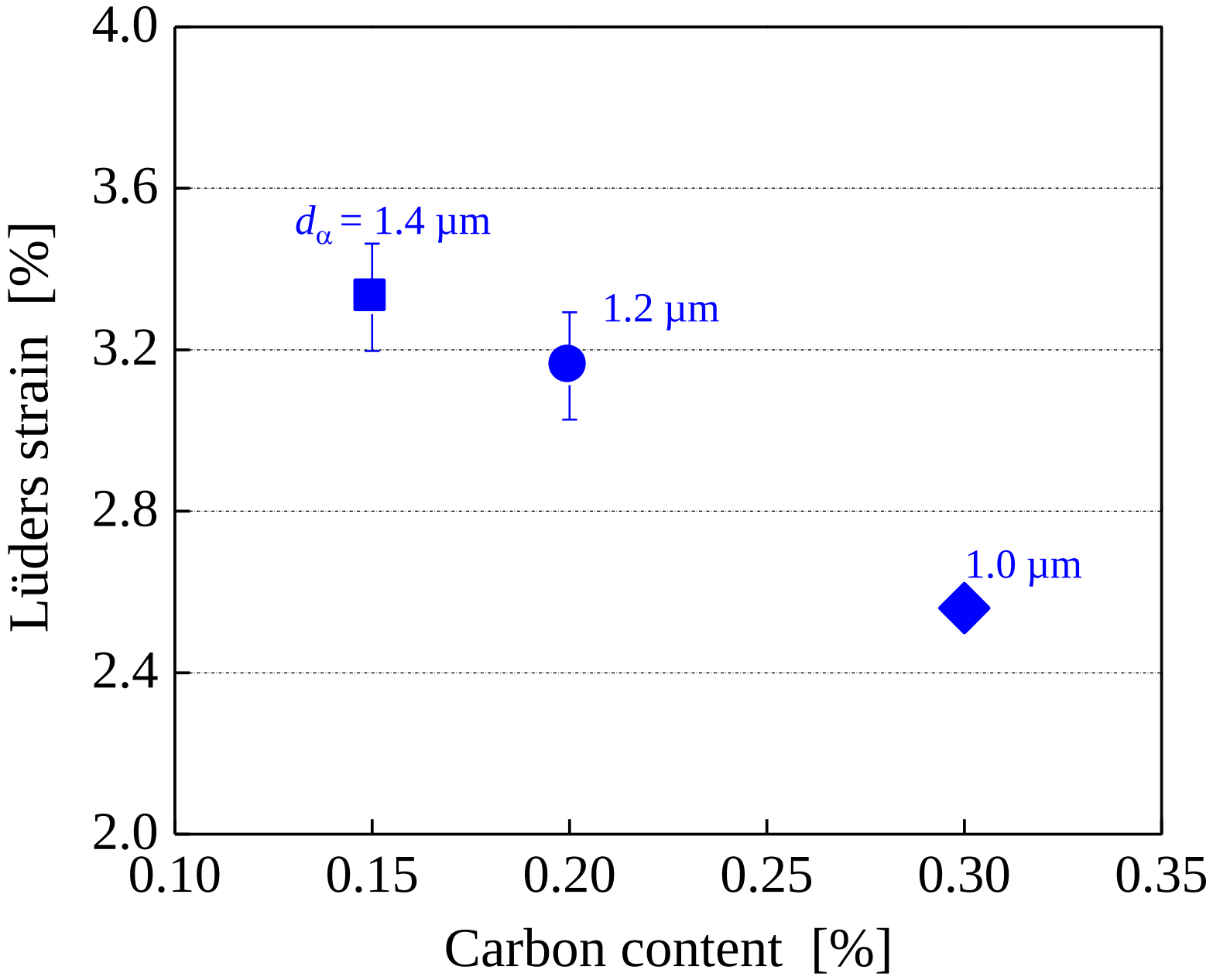

Grain size

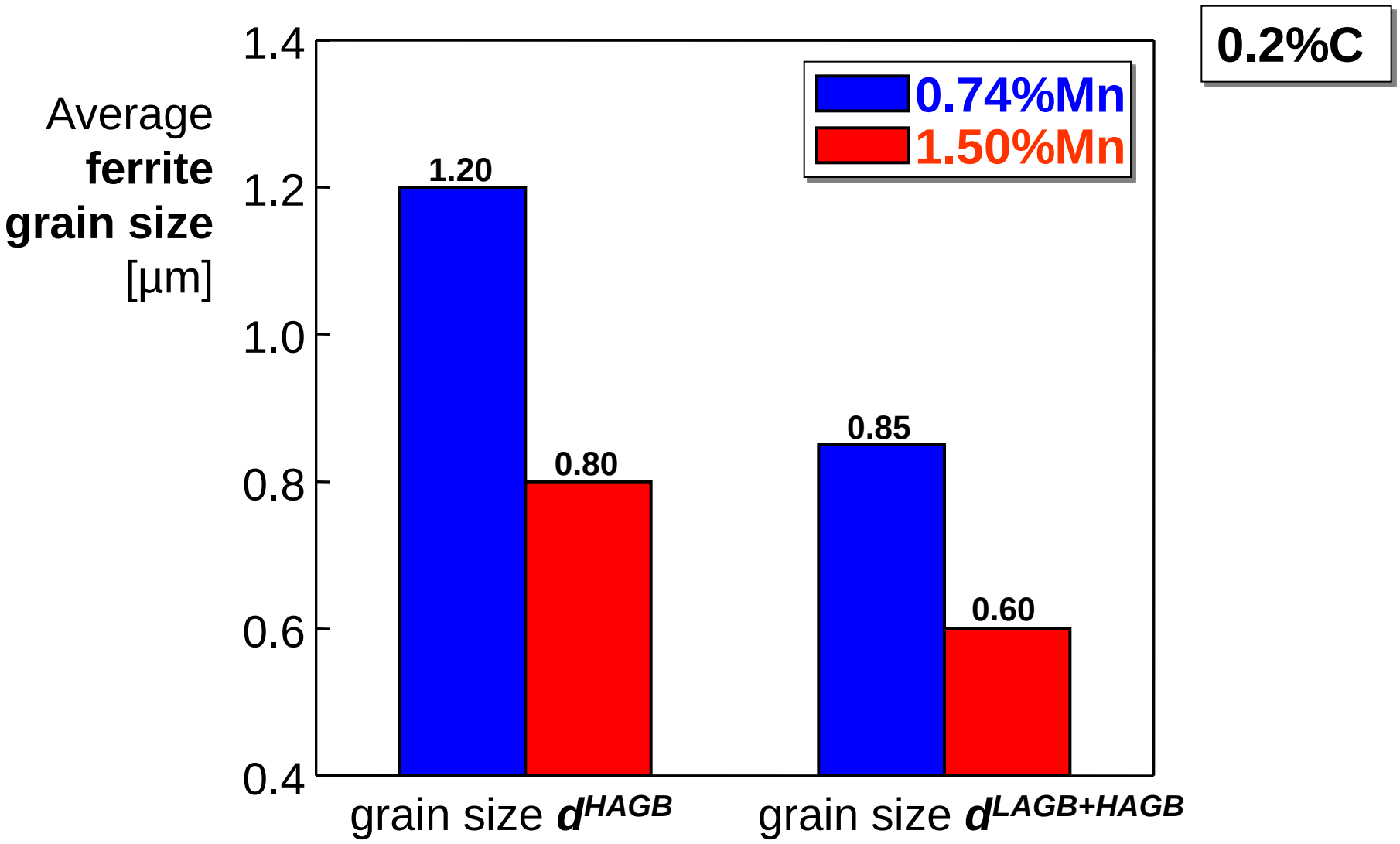

Mean linear intercept $\Theta_{min} \geq 15°$ $\Theta_{min} \geq 2°$

Tensile Tests: Comparison UFG and CP steels

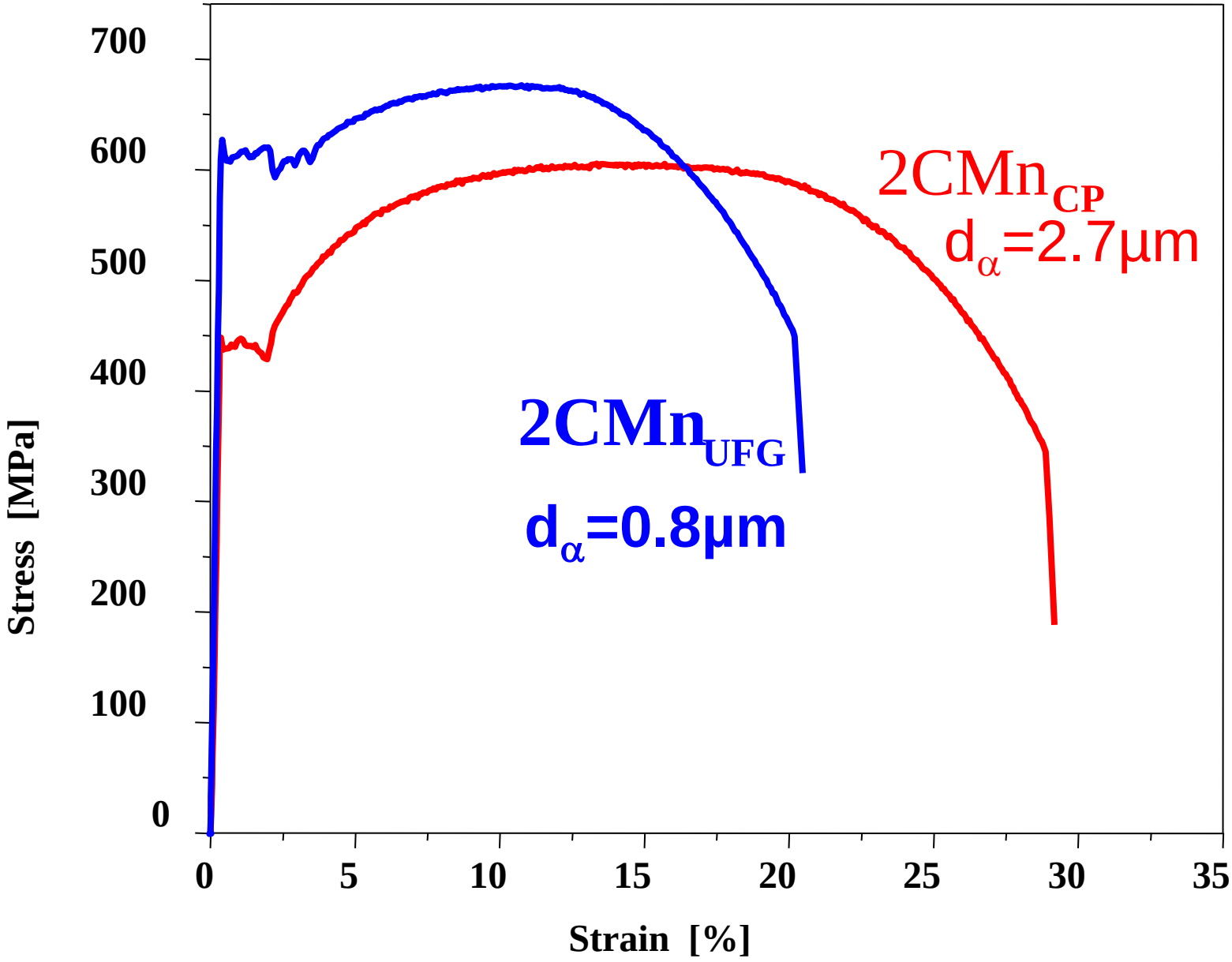

Work hardening rate

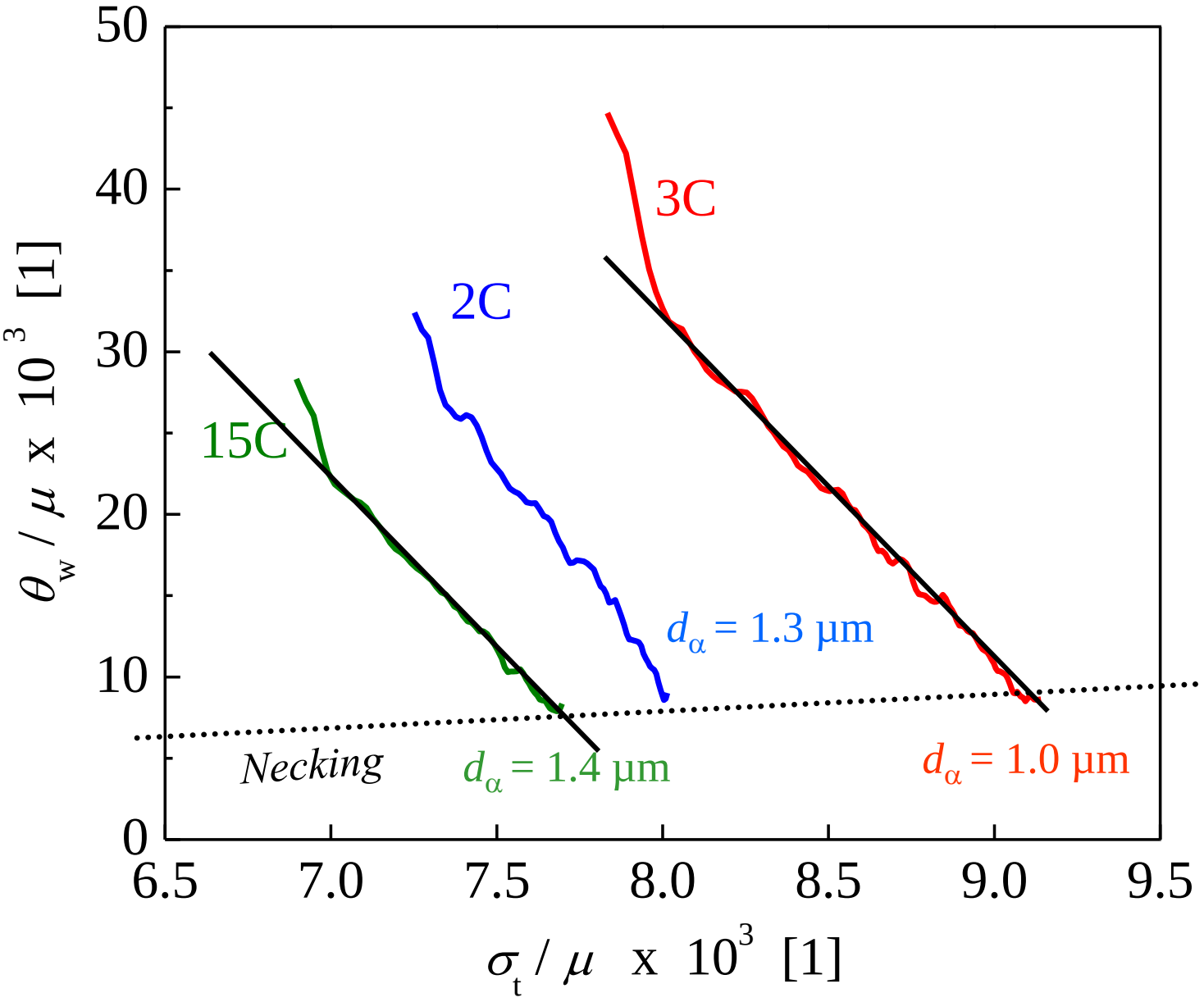

Comparison UFG and Q&T condition (3C)

QT: quenched and tempered at 670°C

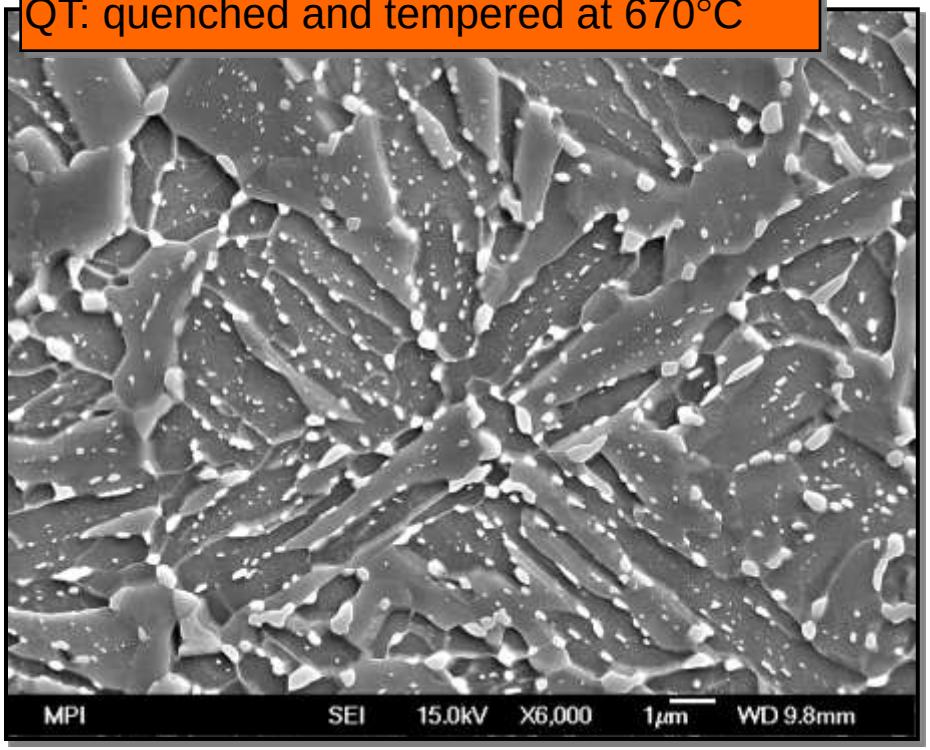

HWR: heavy warm rolling / coiling at 670°C

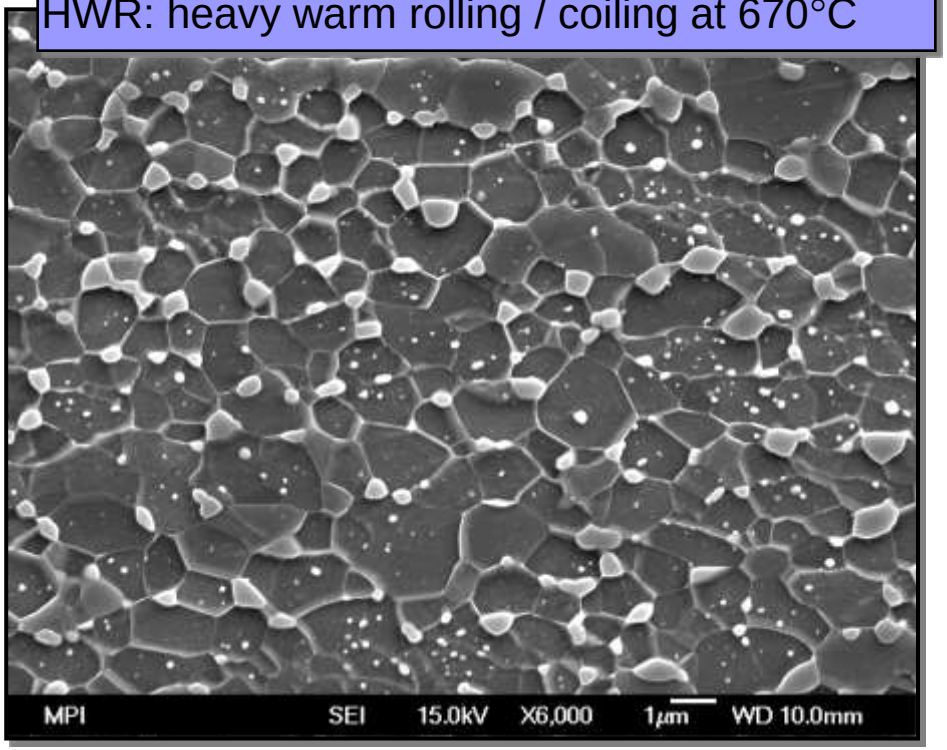

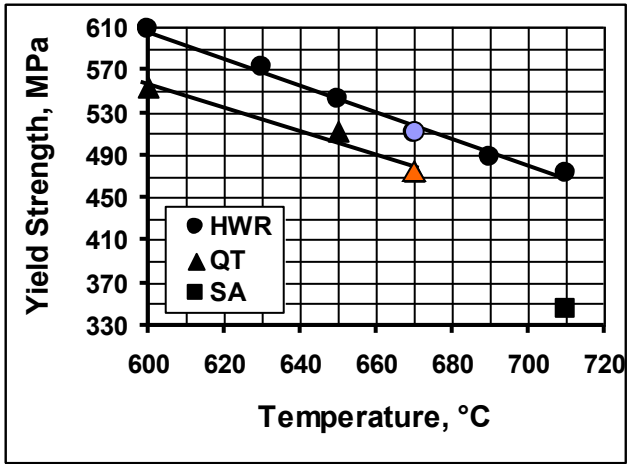

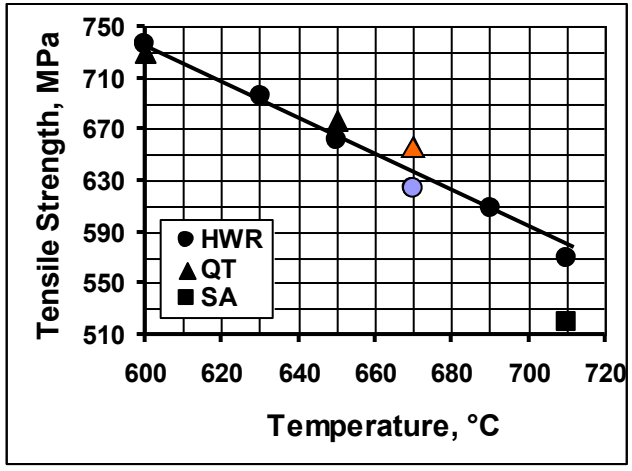

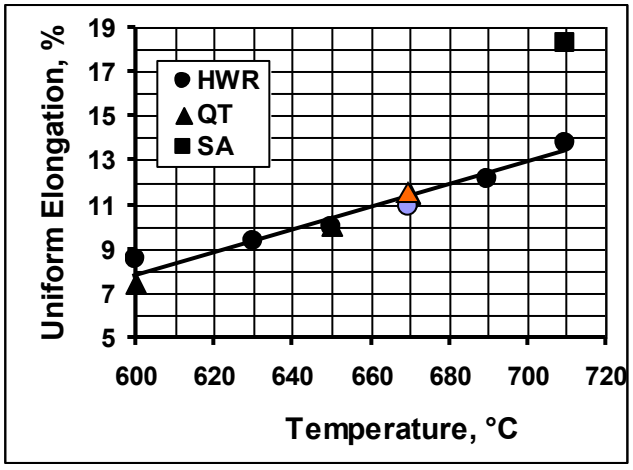

Comparison of the microstructure and texture

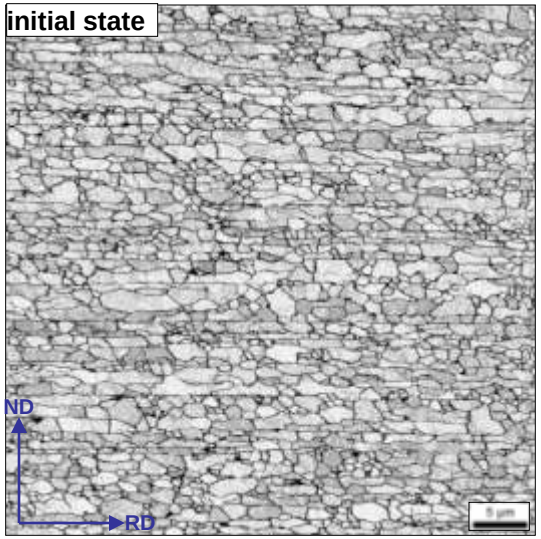

cementite fraction: 2%
ferrite grain size: 1.5 µm

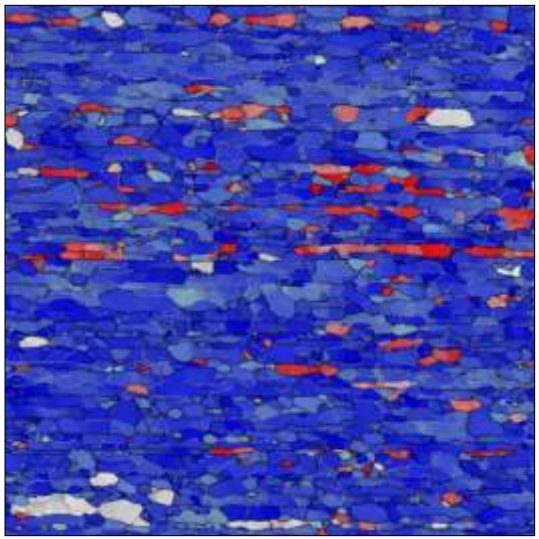

- (110)||(100): 90.7%
- (111)||(001): 7.1%

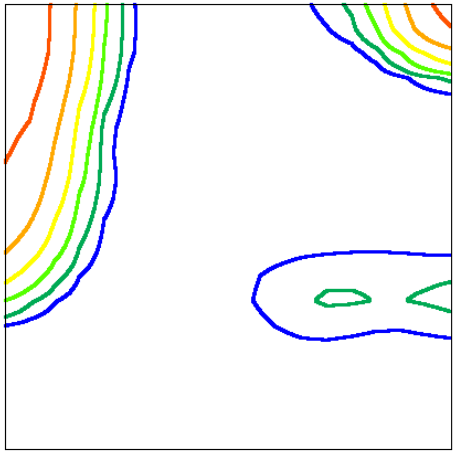

45°

$f(g)_{max}$ = 24

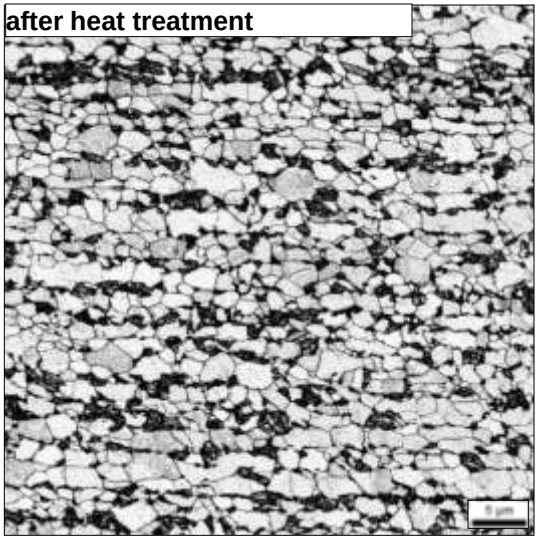

martensite fraction: 16%
ferrite grain size: 1.2 µm

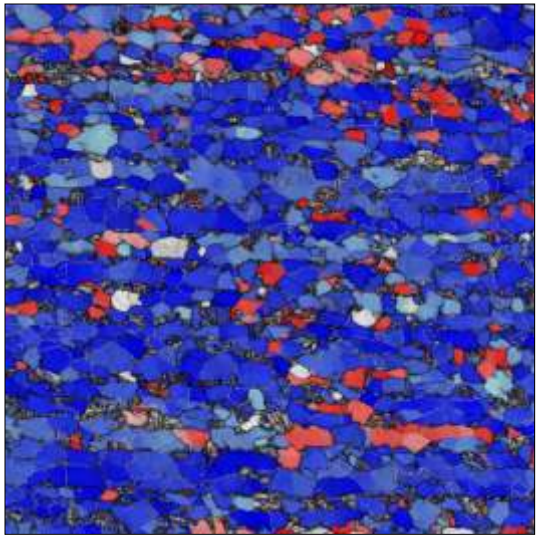

- (110)||(100): 78.3%
- (111)||(001): 13.5%

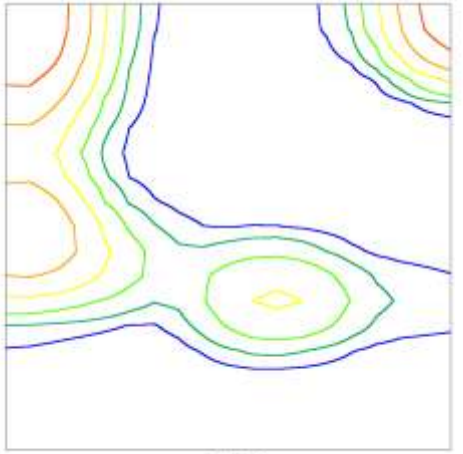

45°

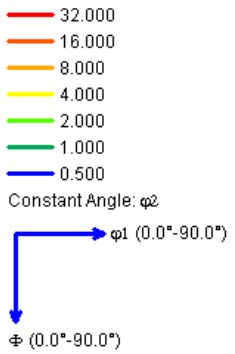

$f(g)_{max}$ = 29

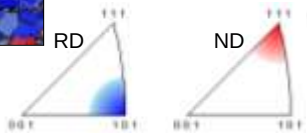

Materials Science and Engineering A 527 (2010) 2738–2746

Contents lists available at ScienceDirect

Materials Science and Engineering A

journal homepage: www.elsevier.com/locate/msea

Orientation gradients and geometrically necessary dislocations in ultrafine grained dual-phase steels studied by 2D and 3D EBSD

Marion Calcagnotto*, Dirk Ponge, Eralp Demir, Dierk Raabe

Max-Planck-Institut für Eisenforschung, Max-Planck-Str. 1, 40237 Düsseldorf, Germany

ARTICLE INFO

Article history:
Received 1 July 2009
Received in revised form
22 December 2009
Accepted 6 January 2010

Keywords:
Dual-phase steel
Grain refinement
Orientation gradient
GND
3D EBSD

ABSTRACT

We study orientation gradients and geometrically necessary dislocations (GNDs) in two ultrafine grained dual-phase steels with different martensite particle size and volume fraction (24 vol.% and 38 vol.%). The steel with higher martensite fraction has a lower elastic limit, a higher yield strength and a higher tensile strength. These effects are attributed to the higher second phase fraction and the inhomogeneous transformation strain accommodation in ferrite. The latter assumption is analyzed using high-resolution electron backscatter diffraction (EBSD). We quantify orientation gradients, pattern quality and GND density variations at ferrite–ferrite and ferrite–martensite interfaces. Using 3D EBSD, additional information is obtained about the effect of grain volume and of martensite distribution on strain accommodation. Two methods are demonstrated to calculate the GND density from the EBSD data based on the kernel average misorientation measure and on the dislocation density tensor, respectively. The overall GND density is shown to increase with increasing total martensite fraction, decreasing grain volume, and increasing martensite fraction in the vicinity of ferrite.

1. Introduction

Dual-phase (DP) steels are low-carbon low-alloy materials with 20–30 vol.% martensite in a ductile ferrite matrix. As they combine high strength and good formability at low production costs they are widely used for automotive applications [1]. In response to the increasing demand for fuel efficiency and occupant safety, it was shown that grain refinement is an effective tool to strengthen dual-phase steels without raising alloying costs or allowing a decrease in ductility [2–5]. In this study, ultrafine grained DP steels with different martensite fractions were fabricated by large strain warm deformation of a plain C–Mn ferrite–pearlite steel and subsequent intercritical annealing.

Various studies aimed at a better understanding of the excellent mechanical properties of dual-phase steels [6–34]. There is broad consensus that the low elastic limit (defined as the first deviation from Hooke's law in the stress–strain curve), the continuous yielding and the high strain hardening rate are a consequence of the austenite-to-martensite transformation which involves a volume expansion. In our materials, the volume expansion is approximately 2.9% at the martensite start temperature.[1] The strains produced by the transformation result in residual stresses in the surrounding ferrite [6,7]. These internal stresses are assumed to facilitate plastic flow and hence, reduce the elastic limit. Furthermore, the volume change induces plastic deformation of adjacent ferrite grains and, therefore, creates a high density of unpinned dislocations in the vicinity of martensite [8–10] as was qualitatively studied by transmission electron microscopy (TEM) [11–13]. These dislocations are assumed to be (at least partly) mobile during the early stages of deformation and contribute to work hardening. The heterogeneous distribution of dislocations is supposed to control continuous yielding in dual-phase steels. It is assumed that the deformation starts in ferrite areas with low dislocation densities and spreads with increasing plastic strain into regions with higher dislocation densities [14].

At least a part of the adjacent ferrite grains has to deform plastically owing to the volume expansion during austenite-to-martensite transformation. During this deformation, geometrically necessary dislocations (GNDs) are required for maintaining lattice continuity [35–37] and statistically stored dislocations (SSDs) evolve from random trapping processes [36]. After such transformation-induced deformation, residual stresses remain due to the inhomogeneity of the plastic deformation throughout the

* Corresponding author. Tel.: +49 211 6792 416; fax: +49 211 6792 333.
E-mail addresses: m.calcagnotto@mpie.de (M. Calcagnotto), d.ponge@mpie.de (D. Ponge), e.demir@mpie.de (E. Demir), d.raabe@mpie.de (D. Raabe).

[1] The calculation of the volume expansion is based on the equilibrium chemical composition of austenite at the intercritical annealing temperature calculated using ThermoCalc, and the approximate equations for the martensite start temperature and for austenite-to-martensite volume expansion given in Refs. [23,24], respectively.

0921-5093/$ – see front matter © 2010 Elsevier B.V. All rights reserved.
doi:10.1016/j.msea.2010.01.004

grains [38]. Yet, it is still not understood to what extent geometrically necessary dislocations (GNDs), statistically stored dislocations (SSDs), and the associated residual stresses contribute to the yielding behavior of dual-phase steels. To address this question, a detailed quantification of the in-grain distribution of dislocations is necessary. However, corresponding findings presented to date are mainly based on coarse grained DP steels using theoretical calculations and TEM observations. While these works improved our understanding of local dislocation accumulation in the vicinity of ferrite–martensite interfaces, TEM investigations have the shortcoming that only a small area can be observed and that sample preparation can create defects or recovery of the microstructure. By means of high-resolution electron backscatter diffraction (HR-EBSD) it is possible to obtain information in a representative area even in ultrafine grained materials [39–41]. Individual crystallographic orientations as well as polarized arrays of dislocations with the same sign can be studied. By using automated orientation imaging microscopy (OIM), the electron beam scans the area inspected and records for each point the crystallographic orientation and a value for the quality of the Kikuchi pattern, viz. the Image Quality (IQ). The latter quantity is linked to lattice imperfections. Local changes in the lattice orientation reflect lattice curvature and can be used to calculate GND densities. In this study, two methods will be introduced to retrieve GND densities from the HR-EBSD data. In addition, we use 3D EBSD tomographic measurements to obtain information about the grain volume and about the true distribution of martensite in order to quantify their effects on GNDs. In contrast to TEM, EBSD does not depict individual dislocations and also, the angular and spatial resolution is lower. However, the resolution obtained here (around 0.3° and 50 nm, see below) is high enough to describe phenomena occurring on a tens of nm to μm scale.

2. Methods

2.1. Materials processing, metallography and mechanical testing

The investigated steel contains 0.17%C, 1.63%Mn, 0.28%Si, 0.036%Al, 0.0021%P, 0.0038%S and 0.0025%N (wt.%). The cast ingot was cut into samples of 50 mm × 40 mm × 60 mm. A 2.5 MN hot press was used for processing [42]. After 3 min austenitization, a one-step deformation pass was imposed for obtaining fully recrystallized austenite (Fig. 1). By controlled cooling, a ferrite–pearlite microstructure was obtained. For grain refinement to the μm-scale, large strain warm deformation was performed by exerting a four-step flat compression series (550 °C, total strain: 1.6). Subsequently, a heat treatment of 2 h at 550 °C was applied. The resulting microstructure was an ultrafine grained ferrite matrix with homogeneously distributed spheroidized cementite particles. Further processing and microstructure details are given in [43].

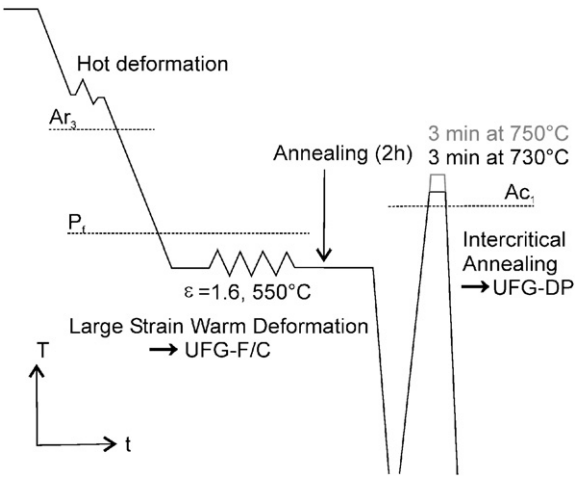

Fig. 1. Complete processing route for the production of ultrafine grained ferrite/martensite dual-phase steel (DP) from ultrafine grained ferrite/cementite (UFG-F/C) steel.

The final ferrite/martensite dual-phase structure was produced by short intercritical annealing in the ferrite/austenite region followed by quenching to transform all reversed austenite into martensite. The determination of the intercritical annealing parameters and their effect on the microstructure are described elsewhere [44,45]. Intercritical annealing was performed in a salt-bath furnace on samples of 12 mm × 10 mm × 75 mm. One sample (hereafter referred to as sample 730-DP) was held in the salt-bath at 730 °C for 3 min before it was water quenched to room temperature. For the second sample (750-DP) we used a temperature of 750 °C and the same holding time. With this procedure different martensite fractions were obtained in the two specimens to study the effects of the martensite particle size and of retained cementite on local orientation gradients. The phase fractions were determined on SEM micrographs. The ferrite grain size was investigated using the mean linear intercept method. Stress–strain curves were determined using flat tensile specimens with a cross-section of 3.5 mm × 5 mm and a gauge length of 10 mm (room temperature, constant cross-head speed with an initial strain rate of $0.5 \times 10^{-3}\ s^{-1}$).

2.2. Experimental setup for 2D EBSD

EBSD specimens were prepared by grinding, polishing, and electropolishing (Struers electrolyte A2; voltage: 30 V; flow rate 12 s^{-1}). EBSD maps were taken on a JEOL JSM 6500F electron microscope (SEM) equipped with field emission (FEG). The small beam diameter and its high brightness yield high-contrast Kikuchi patterns so that information about small orientation deviations even in areas with high dislocation densities like phase or grain boundaries was obtained. A high-speed DigiView CCD camera was used for pattern acquisition. Data were recorded at 50 nm step size and analyzed using the TSL software [46]. By choosing the highest possible image resolution for pattern processing and by optimizing the Hough transform parameters, an angular resolution of about 0.3° can be obtained [46,47]. The lateral resolution of the system is around 30 nm parallel to the tilt axis and around 90 nm perpendicular to the tilt axis, determined on iron at 15 kV [48]. Martensite was indexed as bcc ferrite and distinguished from ferrite by its significantly lower Image Quality and Confidence Index.

2.3. Experimental setup for 3D EBSD

For microstructure characterization in 3D we used automated serial sectioning via focused ion beam (FIB) combined with EBSD orientation microscopy in each section [49,50]. Our system consists of a Zeiss-Crossbeam XB 1540 FIB-SEM equipped with a Gemini-type FEG and an EDAX-TSL EBSD system. The ion beam column is mounted 54° from the vertical. The EBSD camera is placed on the opposite site. The sample is prepared by grinding and polishing of two perpendicular faces to produce a sharp rectangular edge. FIB milling (Ga^+ ions, accelerated at 30 kV) is performed on one surface starting from this edge. After milling, the sample is automatically shifted to the 70° EBSD position by tilting it 34° and adjusting the *y* position. EBSD is performed on the milled surface, before the sample is tilted back to the FIB position. For precise positioning between the steps, a marker is set. After each tilt, this marker is detected via image recognition. This software governs the beam shift which brings the sample to its reference position.

The step size and milling depth for the 3D maps was 100 nm. The scan size in each slice was 20 μm × 20 μm. The scan height is restricted by curtaining effects of the FIB milling which occur from

a certain distance below the top edge and deteriorates the EBSD pattern quality. To avoid shadow effects on the EBSD camera, additional surface areas had to be milled adjacent to the measured area. These areas were milled with 2 nA, as they do not require good surface finish. The fine milling of the scan area was conducted using a 500-pA beam. The total time for mapping 42 slices, including camera movement and image recognition, adds up to 23 h, which is within the long-term stability time of the instrument. The camera settings and the Hough parameters were set such that a pattern acquisition rate of 70 fps was obtained without significant decrease in pattern quality. Using these high-speed parameters the angular resolution is around 0.5°. A minor drawback of FIB milling DP steels is that very small amounts of retained metastable austenite may transform into martensite under the influence of the ion beam. However, the austenite distribution is not crucial for our analysis. Details about the 3D EBSD setup and its accuracy are given in [51–53]. Related studies on 3D reconstruction from EBSD data were presented in [54–58].

2.4. Calculating GND densities from EBSD data

Two approaches to calculating GND densities were applied and compared. The first one follows Kubin and Mortensen [59]. Based on the strain gradient model by Gao et al. [60], the authors define a GND array for simple cylinder torsion. Assuming a series of twist subgrain boundaries in the cylinder, each containing two perpendicular arrays of screw dislocations, the misorientation angle ϑ is related to the GND density ρ_{gnd},

$$\rho_{gnd} = \frac{2\vartheta}{ub}, \tag{1}$$

where u is the unit length and b is the magnitude of the Burgers vector. As a first order approach, the kernel average misorientation (KAM), which is retrieved directly from EBSD data, was chosen as a measure for the local misorientations. The KAM quantifies the average misorientation around a measurement point with respect to a defined set of nearest or nearest plus second-nearest neighbor points. Values above a predefined threshold (here it is 2°) are excluded from the calculation, because these points are assumed to belong to adjacent grains or subgrains (Fig. 2a).

The second method to evaluate GND densities is based on the calculation of the full dislocation density tensor as recently suggested in [61]. The components of that tensor α_{pi} are found using the neighbor-to-neighbor orientation gradients $g_{ij,k}$

$$\alpha_{pi} = e_{pkj} g_{ij,k} \tag{2}$$

where "e" indicates the permutation symbol. The orientation gradients are obtained from the EBSD orientation maps. First, the minimum misorientation between two adjacent points is calculated by applying the 24 crystal symmetry operators to both orientations. Then, the orientation gradient is calculated as the misorientation between the points divided by their distance. The orientation gradients are related to GNDs by use of a Frank's loop construction, Eq. (3). GNDs are characterized by the Burgers vector b (slip direction) and the tangent vector t (dislocation line direction). For simplicity, only the $\{1\,1\,0\}$ slip planes were used for the calculation [62,63]. Hence, there are 16 possible GND configurations in ferrite: 4 $\langle 1\,1\,1 \rangle$ edge dislocations and 4×3 $\langle 1\,1\,2 \rangle$ screw dislocations. As an ambiguity arises when relating 16 GND densities to nine dislocation tensor components, an energy minimization method was applied. Details of this approach are given in [61].

$$\alpha_{ij} = \sum_{a=1}^{9} \rho_{gnd}^{a} b_i^a t_j^a \tag{3}$$

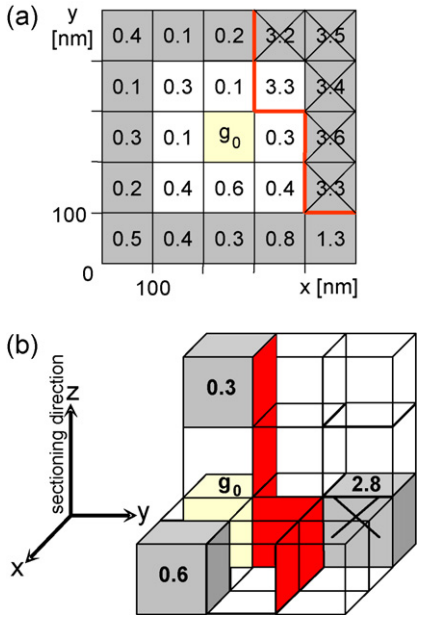

Fig. 2. Principles of the GND density calculation based on the kernel average misorientation (a) and the dislocation tensor (b) for the case of a 2nd neighbor evaluation and a step size of 100 nm. Grain boundaries are marked in red. Misorientations that exceed the minimum threshold value of 2° are excluded from the calculation of the average misorientation of neighboring points to a given measurement point g_0 and from the calculation of orientation gradients.

The calculation was done for each EBSD point and the orientation gradients were calculated with respect to its 2nd neighbors in 3D (Fig. 2b). If one of the three gradients exceeded the threshold angle of 2°, it was discarded and the GND density was calculated on the basis of the two other orientation gradients. For a physically meaningful GND density determination, the rank of the neighbor considered for the misorientation calculation is critical. The following points have to be considered when choosing the distance between two measurement points: (1) the distance has to be low enough to allow detailed information to be obtained; (2) the distance has to be high enough to average out scatter due to EBSD spatial resolution limits; and (3) to perform the calculations with misorientations above the angular EBSD resolution limits.

Fig. 3 shows a comparison of the two calculation methods (same EBSD data set) and the influence of the neighbor rank on the GND density calculation. The Image Quality (IQ) map shows the location of the grain boundaries and the martensite. In all maps, the misorientations along the grain boundaries and in the martensite exceed those in the ferrite grain interior. As the simple KAM values are not normalized by spacing, the KAM values increase with increasing neighbor rank. This is not the case for the calculated GND densities, as these values are distance normalized. Comparing the respective GND densities obtained for the 1st and 2nd neighbor sets reveals that the contrast between high and low GND density areas increases with increasing neighbor rank. Hence, from the 2nd neighbor GND maps, the location of grain boundaries and martensite can be more clearly distinguished. In the 1st neighbor sets the scatter is too high to yield distinct results. For this reason, a distance of 200 nm, which corresponds to the 2nd neighbor rank in the case of 3D EBSD measurements and to the 4th neighbor rank in the case of 2D EBSD measurements, was chosen for the GND calculations.

In general, both calculation methods yield very consistent results although the values obtained from the KAM-based calculation method tend to be a little lower. Moreover, this method

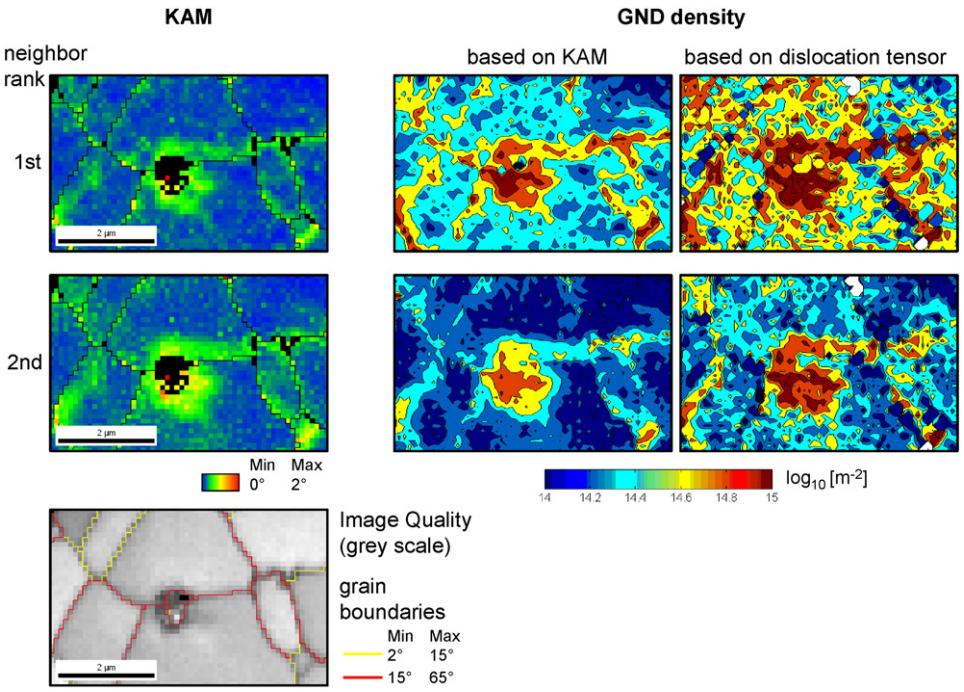

Fig. 3. The calculation of the GND densities based on the kernel average misorientation (KAM) and the dislocation tensor yield similar results. The 2nd neighbor rank, corresponding to a distance of 200 nm, is most suitable to obtain scatter-free information.

leads to a more even distribution of the GND densities. This can be attributed to the better statistics associated with the KAM-based method. Using the KAM, the local misorientation is calculated as an average of up to 16 values (in the 2nd neighbor configuration), whereas the maximum number of orientation gradients used for the formation of the dislocation tensor is 3 (Fig. 2). It can be concluded that both methods are appropriate to calculate GND densities from EBSD data sets.

It must be mentioned that the threshold value of 2° which is physically reasonable for ferrite does not apply for martensite. Due to the lattice distortion during martensite formation, misorientations above 2° can be present inside a single martensite variant. In fact, orientation gradients of up to 5° at a distance of 200 nm occurred frequently in our EBSD data. These misorientations were excluded from the calculations. Therefore, the GND density in the martensite might be slightly underestimated in our analysis. Moreover, the GND density distribution in martensite appears to be uniform, as most of the values considered for the calculation are slightly below 2°. However, the true GND density in martensite is not critical for the present investigation.

3. Results and discussion

3.1. Microstructure and mechanical properties

The initial ferrite/cementite (UFG-F/C) steel consists of an ultrafine grained ferrite matrix and finely dispersed spheroidized cementite particles distributed mostly along ferrite grain boundaries (Fig. 4a). Sample 730-DP is characterized by a ferrite matrix with 24 vol.% mostly isolated martensite particles and 2 vol.% cementite (Fig. 4b) The average ferrite grain size is 1.4 μm. Increasing the intercritical temperature to 750 °C leads to the complete dissolution of cementite and to an increase in the martensite fraction to 38 vol.% (Fig. 4c). The ferrite grain size decreases slightly to 1.2 μm due to progressive austenite grain growth.

Fig. 5 shows the engineering stress–strain curves of the two dual-phase steels. For comparison, the starting material (UFG-F/C) is included. The UFG-F/C steel exhibits the common features of this material, i.e. relatively high yield strength, pronounced Lüders straining and a low strain hardening rate. The replacement of cementite by martensite leads to a significantly lower yield ratio and to continuous yielding, whereas total elongation is decreased.

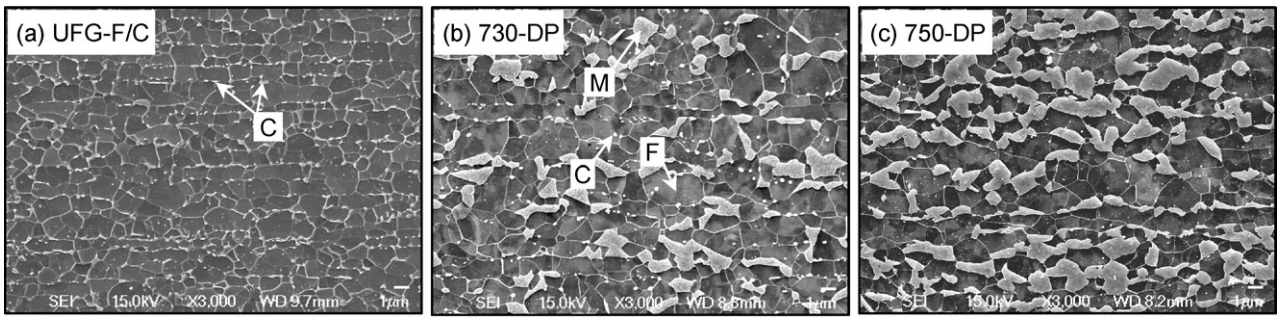

Fig. 4. SEM micrographs of the samples discussed in this study. (a) Ultrafine grained ferrite/cementite (UFG-F/C) steel obtained after large strain warm deformation. (b and c) Ferrite/martensite dual-phase structure obtained by subsequent intercritical annealing at 730 °C (730-DP, 24 vol.% martensite) and 750 °C (750-DP, 38 vol.% martensite), respectively. F: ferrite, M: martensite, C: cementite.

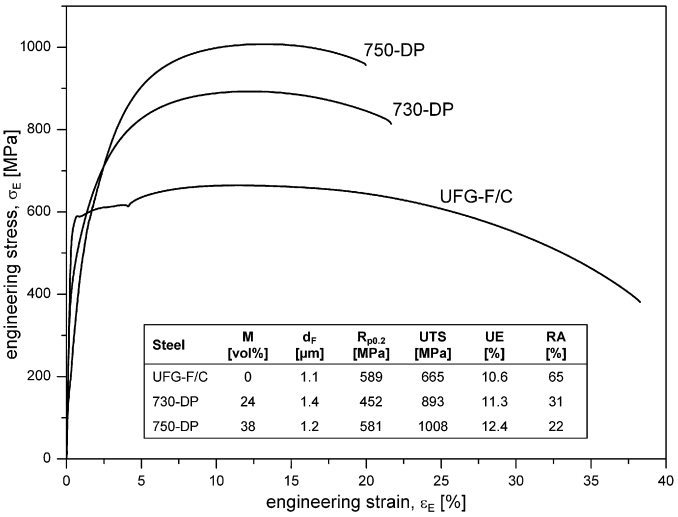

Steel	M [vol%]	d_F [μm]	$R_{p0.2}$ [MPa]	UTS [MPa]	UE [%]	RA [%]
UFG-F/C	0	1.1	589	665	10.6	65
730-DP	24	1.4	452	893	11.3	31
750-DP	38	1.2	581	1008	12.4	22

Fig. 5. Engineering stress–strain curves of the starting ultrafine grained ferrite/cementite steel (UFG-F/C) and the two dual-phase steels annealed at 730 °C (730-DP) and at 750 °C (750-DP) containing 24 vol.% and 38 vol.% martensite, respectively. M: martensite, d_F: average ferrite diameter, UTS: ultimate tensile strength, UE: uniform elongation, RA: reduction in area. Initial strain rate: 0.5×10^{-3} s^{-1}.

Increasing the martensite fraction leads to a lower elastic limit. This effect was explained in terms of residual stresses [21,31]. As the fraction of ferrite–martensite interfaces increases with increasing martensite fraction, a higher fraction of ferrite is affected by the martensitic phase transformation and hence, higher residual stresses are introduced into the matrix. This might be the reason why the elastic limit in ferrite is locally reached earlier during tensile deformation which is reflected by the lower initial slope of the curve with higher martensite fraction (750-DP). As both DP steels were stored at room temperature before tensile straining, dislocation locking by segregation of solute carbon does not occur, and the reoccurrence of a yield point is suppressed. The 750-DP sample has a tensile strength of 1003 MPa (table in Fig. 5) which is about 100 MPa above that of the 730-DP steel. The offset 0.2% offset yield strength ($R_{p0.2}$) is higher, too. The higher strength levels are generally attributed to the higher phase fraction of the hard second phase and can be approximated by a volumetric linear rule of mixtures [15,17]. The uniform elongation is hardly affected by the martensite fraction. Yet, as the plastic strain of the martensite phase is negligible, the total elongation to fracture is reduced with increasing martensite fraction. The initial strain hardening rate in both dual-phase steels is very high. This behavior is commonly interpreted in terms of local dislocation accumulation [18,30] introduced by the martensitic transformation.

The three curves show how strong the influence of martensite on plastic behavior of ferrite is and hence, how important it is to obtain quantitative information about the in-grain misorientations caused by the martensitic phase transformation.

3.2. Orientation gradients and GNDs in 2D

The enhanced dislocation density around martensite (athermal transformation) compared to cementite (diffusional transformation) can be visualized by using a high-resolution EBSD analysis placing emphasis on local orientation gradients at interfaces. Fig. 6 shows two such EBSD maps of sample 730-DP (a,c) and 750-DP (b,d). In these maps, the grey scale maps correspond to the Image Quality (IQ). The darker the color, the lower is the IQ value and the higher the lattice distortion. This measure allows one to distinguish the martensite clearly from the matrix as it exhibits higher lattice distortion. The color maps show the kernel average misorientation (KAM). Here, the average misorientation of an EBSD point is calculated with respect to all neighbors at 300 nm distance (values above 2° are excluded). As expected, the largest orientation gradients are found within the martensite islands. These KAM values are even underestimated due to the low threshold value of 2° (see discussion above). More importantly, the KAM maps reveal considerable orientation gradients spreading from the ferrite–martensite (FM) phase boundaries into the ferrite grain interior as was shown, yet not quantified, by the authors in a previous paper [64]. Each martensite particle is surrounded by at least one distinct orientation gradient in one of its neighboring ferrite grains, independent of the martensite particle size. One could expect that larger par-

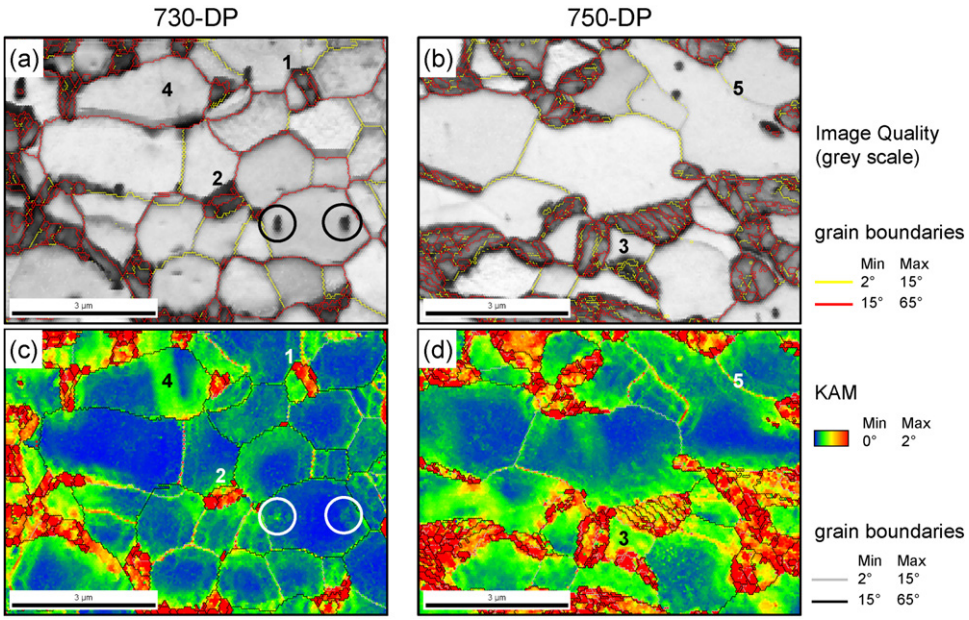

Fig. 6. Orientation gradients near ferrite–ferrite grain boundaries, ferrite–cementite phase boundaries and ferrite–martensite phase boundaries in the dual-phase (DP) steels containing 24 vol.% martensite (730-DP) and 38 vol.% martensite (750-DP). (a and b) Image Quality maps, where light values indicate high Image Quality, hence low lattice distortions. (c and d) Respective kernel average misorientation (KAM) maps. Distinctive features are numbered and described in the text.

ticles affect larger volume fractions of the adjacent ferrite grains, because the absolute volume increase is higher during transformation. However, even very small martensite particles cause strong local plastic deformation. A possible explanation is that smaller austenite particles have higher carbon content and, hence, undergo larger volume expansion [65]. Another aspect is the distribution of martensite around the ferrite grain. The more of the ferrite grain is surrounded by martensite, the higher the resulting in-grain orientation gradients. Cementite (encircled in Fig. 6) is not surrounded by notable orientation gradients. This confirms the experimental accuracy of the approach. The region affected by martensite is not necessarily distributed homogeneously around martensite particles, as can be seen when comparing the particles numbered (1) and (2). It is noteworthy, that orientation gradients are visible in ferrite grains of all sizes, even in very small ferrite grains with diameters of only 500–1000 nm. In case of a high number of martensite neighbors, these grains are sometimes entirely affected by the shape accommodation, i.e. the whole grain is work-hardened after martensitic phase transformation (grain number 3). There are also some minor dislocation accumulations visible at the ferrite–ferrite (FF) grain boundaries. Yet, the frequency of these gradients is scarce and less pronounced than at the FM interfaces. Furthermore, it is possible that the gradients arise from martensite particles present below or above the FF grain boundary (see 3D analysis below). Subboundaries with misorientation below 2° appear as regions of high misorientations (numbers 4 and 5) which must not be attributed to the martensitic phase transformation. The overall GND density in the ferrite was calculated on the basis of two HR-EBSD scans sized 10 μm × 20 μm. It is 1.9×10^{14} m^{-2} for the 730-DP and 2.4×10^{14} m^{-2} for the 750-DP. We see that the overall dislocation density in ferrite is increased with increasing martensite fraction, i.e. a higher ferrite fraction experiences local plastic deformation due to the martensitic phase transformation. The introduction of additional dislocations decreases the average spacing between dislocations, which is linked to the yield strength of the material [66]. The EBSD results thus provide an experimental explanation for the higher $R_{p0.2}$ yield strength of the 750-DP. Regarding the Hall-Petch relationship, another reason for the higher strength levels in the 750-DP might be the slightly smaller ferrite grain size (1.2 μm compared to 1.4 μm for the 730-DP). Beside the higher martensite fraction, another reason for the lower GND density in the 730-DP could be the presence of cementite which lowers the carbon content of austenite and thus reduces the transformation strain. Due to the low-alloy content, precipitations are unlikely to occur and therefore do not contribute to the strength increase.

In order to obtain more quantitative information about orientation gradients a number of misorientation profiles were retrieved from the texture maps at both the FF and FM interfaces. The starting point of each profile vector is the respective interface and the end point is the grain center. An example is shown in Fig. 7. The position of the two profile vectors is indicated in the KAM map. The misorientation profile shows the misorientation of a point with respect to the origin. The misorientation profiles do not depend on the overall martensite fraction. Therefore, this analysis includes both the 730-DP and the 750-DP. The FF curve shows a sudden step in the initial misorientation to a value of 0.5°, which can be attributed to lattice imperfections in the immediate vicinity of the FF grain boundaries. After this initial step there is no further increase and the misorientation values remain in the normal scatter range resulting from the spatial resolution of the EBSD system. The misorientation profile starting from the FM interface increases more gradually compared to the FF profile and reaches a much higher value of 1.4° at a distance of around 2 μm from the FM interface. In order to obtain a statistically more robust result, 20 misorientation profiles from different scans were analyzed for a set of different FF and FM interfaces. They all show the same tendencies described above. To obtain a simple yet clear measure for the local orientation gradients emanating from the two types of interfaces, the average misorientation at a distance of 1 μm was determined. It is in average 0.6° in front of FF grain boundaries and 1.2° in front of FM boundaries. The values are included in Fig. 7a (on the x-axis at 1 μm) together with the overall standard deviation for either case. For the FF interfaces the scatter is in the range of the angular resolution of the EBSD system (~0.3°). This indicates that the misorientation profiles reflect a pure grain boundary effect, which is consistently observed. In contrast, the scatter for the FM interfaces is larger. The main reason for this scatter is the inhomogeneity of the in-grain arrangement of the orientation gradients in the ferrite grains, i.e. shape accommodation due to the volume expansion during austenite-to-martensite transformation is realized inhomogeneously in the ferrite grains. Besides the angular resolution, another reason for the influence of the scatter in both profiles is the overall low values of the misorientations. In all cases, however, the orientation gradients emanating from FF boundaries are generally smaller by a factor of two when compared to those stemming from FM interfaces.

From the KAM values, the GND density was calculated (Fig. 7c). The values vary from about 2.5×10^{14} m^{-2} close to the martensite

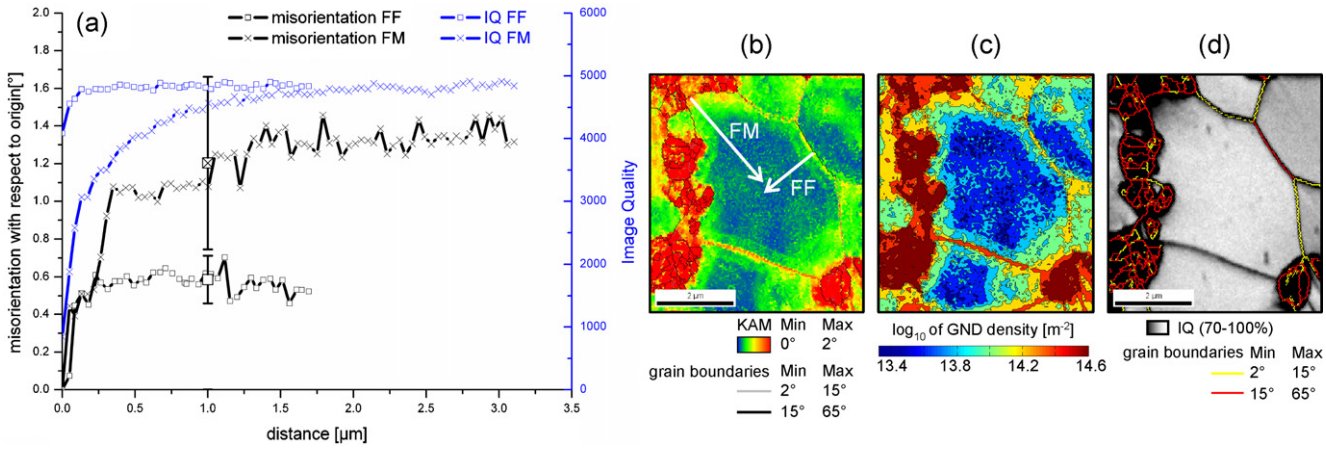

Fig. 7. (a) Misorientation and Image Quality (IQ) evolution from grain boundary to grain center obtained from 2D profile vectors starting from ferrite–martensite (FM) interfaces and ferrite–ferrite interfaces (FF) indicated in (b). Error bars show the statistical result obtained from a range of misorientation profiles. (b) Kernel average misorientation (KAM) map and grain boundaries. (c) GND density calculated from kernel data. (d) IQ map showing the gradual decrease of dislocations from the ferrite–martensite boundaries to the center.

particles to around 2.5×10^{13} m^{-2} in the grain interior. The boundary in the lower left part of the image is a subgrain boundary with a misorientation <2°, so that the GND density calculated in this area is extraordinarily high. The calculated GND densities coincide well with the data reported in the literature based on TEM [14,67] and on theoretical investigations [20]. The TEM studies [14,67] yield dislocation densities which are somewhat higher than the ones presented in this study. The reason is that statistically stored dislocations are additionally counted when evaluating TEM images.

As described above, the Image Quality of the diffraction patterns is also a suitable though qualitative indicator for the total defect density since it reflects the influence of both GNDs and SSDs on the distortion of the diffraction pattern. The in-grain change in the IQ value (Fig. 7d) is demonstrated exemplarily on the basis of the two profile vectors indicated in Fig. 7b. The IQ profile curves show the change in the IQ values with respect to the origin. They run nearly parallel to the respective misorientation profiles (Fig. 7a). The FF IQ profile shows a step close to the grain boundary before it becomes horizontal. In contrast, the FM IQ profile starts with a much lower IQ value and increases gradually up to maximum values in the interior of the ferrite grain. The sudden step of the IQ in the FF profile is due to the overlapping of the Kikuchi patterns along the grain boundary. In the FM IQ curve, this effect is clearly overlaid by the additional dislocations and plastic strains introduced by the martensitic phase transformation. As the pattern quality (IQ) is much more sensitive to surface preparation, surface roughness, contamination, chemical composition, and system calibration than the kernel average misorientation, the values obtained from it must be regarded as qualitative in nature and are hence not used for further calculations. Yet, as an additional evidence for the transformation-induced microstructure inhomogeneity inside the ferrite grains, the pattern quality measure deserves consideration.

In general, the orientation gradients emanating from both FF and FM boundaries are relatively small. However, they reveal important information about the distribution of lattice defects inside the ferrite. The misorientation and pattern quality profiles reveal that the ferrite grains abutting the FM interfaces experience larger values and wider regions of lattice distortion and an enhanced dislocation density than the corresponding areas in the vicinity of the FF grain boundaries.

3.3. Orientation gradients and GNDs in 3D

The 2D analysis revealed important information about the in-grain accommodation of transformation strains in ferrite grains. As a range of grains was analyzed in 2D, statistical errors are small and the findings are reliable. However, the true distribution of martensite and its effect on the GND distribution in the ferrite cannot be resolved by 2D sections alone. For example, an enhanced KAM value is expected all around the martensite particle. Hence, it is possible to observe high dislocation densities in ferrite in 2D sections, which arise from a martensite islands lying below or above this section. This effect is demonstrated in Fig. 8a where the IQ maps and respective KAM maps of two successive sections, separated by 100 nm, are shown. In the first section, considerable misorientations are detected in the center although no martensite is present (arrows). The next slice reveals that those misorientations stem from the martensite particle lying below the first section. The 3D cut along the indicated rectangle reveals the true distribution of the orientation gradients around the martensite (Fig. 8b). The 3D view demonstrates that the orientation gradients observed in 2D do not result from artifacts due to sample preparation. Furthermore, the previous observation from the 2D sections, that the GNDs are distributed inhomogeneously throughout the ferrite grains is found true also in the 3rd dimension (Fig. 8c).

By using a set of such 3D maps, information about grain volume characteristics can be obtained, namely, first, the effect of the ferrite grain volume on its average GND density and second, the effect of the martensite topology on the GND density in the ferrite. For this analysis, a set of complete ferrite grains was selected from the 3D EBSD data. In each slice, the grain size, the average KAM value, and the fraction of the interface covered by martensite were determined for each of the selected grains. This information was used to calculate grain volume, GND density, and the fraction of ferrite–martensite (FM) interfaces covering the grain. In total, 60 ferrite grains were analyzed in full 3D in this way. The number of evaluated large grains is limited due to the restricted total volume investigated (1680 μm^3). Furthermore, large grains containing subboundaries (see Fig. 6, number 4) or martensite particles in the grain interior were excluded from the statistics as these features pretend a higher GND density.

As a general trend, it was found that the average GND density in the ferrite decreases when the grain volume increases (Fig. 9). To understand this tendency, one has to consider that the interfaces (both FM and FF boundaries) enhance the nearby dislocation density, albeit to a different extent. The grain interior is supposed to have a low dislocation density as the material has undergone pronounced recovery during processing [43]. For this reason, the GND density (as well as the total dislocation density) increases with increasing ratio of boundary area to volume, hence, with decreas-

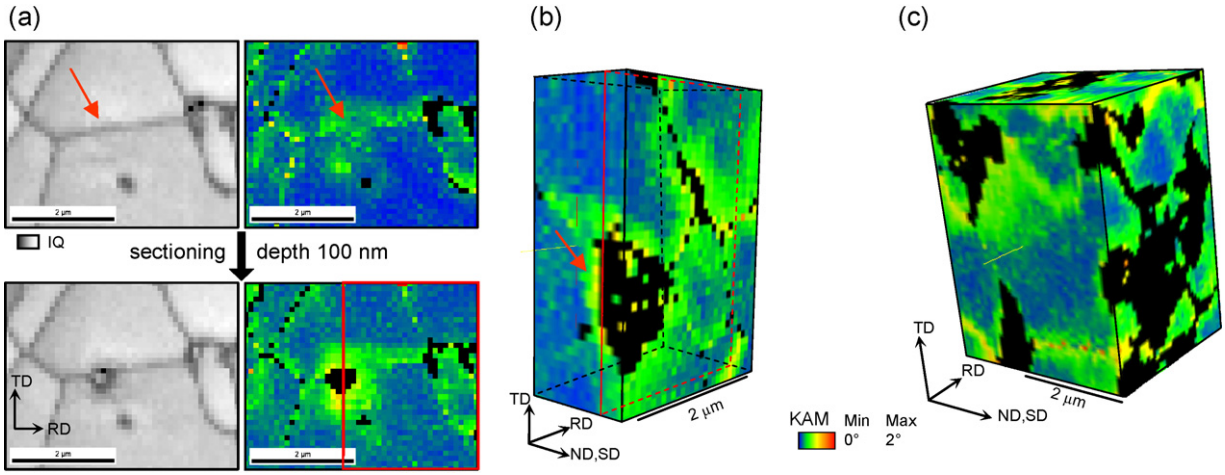

Fig. 8. (a) The Image Quality (IQ) and kernel average misorientation (KAM) maps (martensite is marked in black) of two successive slices reveal the enhancement of local misorientations in ferrite (arrows) due to martensite formation in three dimensions. The 3D view cut along the red rectangle illustrates this effect (b). 3D EBSD investigations in other areas further confirm that orientation gradients are distributed inhomogeneously throughout the ferrite grains (c). SD: sectioning direction.

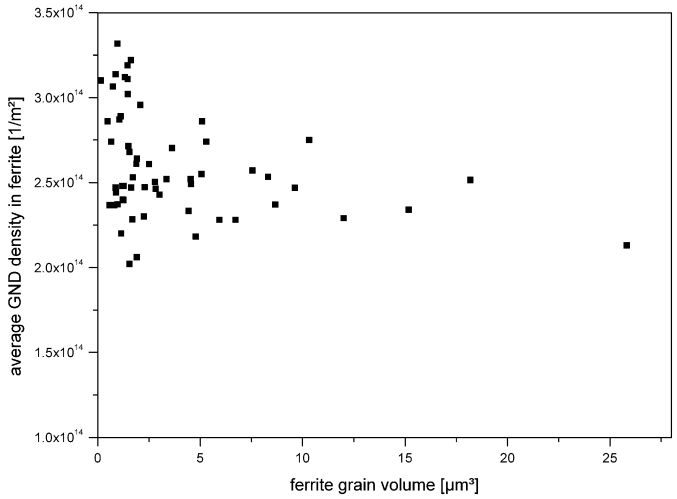

Fig. 9. Effect of grain volume on the average GND density in ferrite obtained from the 3D EBSD analysis. The data are taken from 60 ferrite grains. The overall decreasing tendency is overlaid by the effect of the fraction of ferrite–martensite interface which is resolved in Fig. 10.

ing grain size. Though meaningful, this diagram is incomplete as it does not account for the influence of the martensite distribution around a ferrite grain on the GND density. This is most evident when looking at the GND densities for small grains around 1 μm^3, where the scatter is remarkable. When correlating the GND densities with the respective interface fraction covered by martensite, it turns out that low GND densities correspond to grains with a low FM interface fraction and high GND densities to those with a high FM interface fraction.

For this reason, a second diagram was plotted to demonstrate this effect more clearly (Fig. 10). The grains were divided into classes of different grain sizes. Then, the average GND density of a grain is plotted as a function of the interface fraction covered by martensite. This diagram reveals that GND density is proportional to the FM interface fraction. In particular, smaller grains are more affected by a higher interface fraction of martensite (in terms of their average GND density) than larger grains. This is due to the fact that the volume affected by the martensitic phase transformation is restricted to areas adjacent to the phase boundary. This means that small grains can be entirely deformed when a high interface

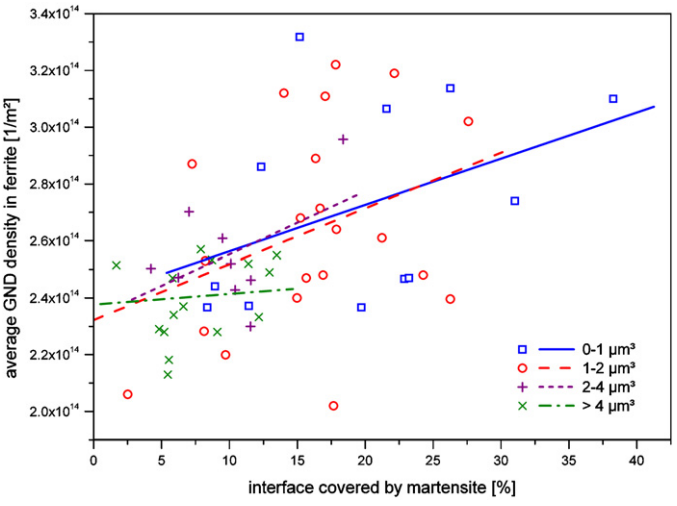

Fig. 10. The average GND density in a ferrite grain volume is proportional to the interface fraction covered by martensite. This effect is more pronounced for grain smaller than 4 μm^3. Data are taken from 60 ferrite grains based on 3D EBSD analysis.

fraction is covered by martensite (Fig. 6, number 3). In large grains, the effect of increasing FM interface fraction is less pronounced because the volume influenced by martensite is small compared to the total grain volume. This effect is only visible when comparing the lower three grain classes with the coarser grains. Thus, this grain size effect becomes relevant for grain volumes larger than 4 μm^3. The scatter of the data is quite high. This is explained by the inhomogeneous accommodation of the transformation strain in ferrite as was also revealed by the 2D EBSD scans. The scatter hence can be attributed to the different factors controlling local strain accommodation, namely ferrite grain size and orientation, as well as grain size and phase distribution of the surrounding grains.

4. Conclusions

Two ultrafine grained dual-phase steels with different martensite fractions were produced by large strain warm deformation and subsequent intercritical annealing. The effect of the volume expansion during martensitic phase transformation on orientation gradients and GNDs in ferrite was analyzed using high-resolution EBSD in 2D and 3D. The main conclusions are

- Orientation gradients originating from ferrite–martensite interfaces are distinctly higher than those initiated at ferrite–ferrite interfaces. The average misorientation at a distance of 1 μm from the boundary was 1.2° for ferrite–martensite interfaces, and 0.6° for ferrite–ferrite grain boundaries.
- Orientation gradients are generally present around each martensite particle, irrespective of particle size. The accommodation of transformation strain is realized inhomogeneously within the ferrite grains.
- The average GND density in the steel with 24 vol.% martensite is $1.9 \times 10^{14}\ m^{-2}$ compared to $2.4 \times 10^{14}\ m^{-2}$ for the steel containing 38 vol.% martensite. The higher fraction of immobile dislocations might contribute to the higher $R_{p0.2}$ yield strength of the latter steel. The enhanced dislocation density around martensite particles was verified by evaluating the Image Quality maps.
- The average GND density of a ferrite grain is proportional to the ferrite–martensite interface fraction surrounding it. This effect is most pronounced for ferrite grain volumes below 4 μm^3. In case of a high number of martensite neighbors, very small grains <1 μm^3 can be entirely work-hardened due to the martensitic phase transformation.
- High-resolution 2D and 3D EBSD is an appropriate tool to obtain information about the local distribution of dislocations in dual-phase steels. The GND density can be calculated both on the basis of the kernel average misorientation and on the dislocation tensor.

References

[1] K. Hulka, Mater. Sci. Forum 414–415 (2003) 101–110.
[2] P.H. Chang, A.G. Preban, Acta Metall. 33 (1985) 897–903.
[3] Z. Jiang, Z. Guan, J. Lian, Mater. Sci. Eng. A 190 (1995) 55–64.
[4] P. Tsipouridis, E. Werner, C. Krempaszky, E. Tragl, Steel Res. Int. 77 (2006) 654–667.
[5] K. Mukherjee, S. Hazra, P. Petkov, M. Militzer, Mater. Manuf. Process 22 (2007) 511–515.
[6] T. Sakaki, K. Sugimoto, T. Fukuzato, Acta Metall. 31 (1983) 1737–1746.
[7] Q. Chen, R. Kaspar, O. Pawelski, Z. Metallkd. 76 (1985) 348–352.
[8] R.G. Davies, Metall. Trans. A 10 (1979) 1549–1555.
[9] M.S. Rashid, in: A.T. Davenport (Ed.), Formable HSLA and Dual-phase Steels, The Metallurgical Society of AIME, New York, 1979, pp. 1–24.
[10] J.M. Rigsbee, J.K. Abraham, A.T. Davenport, J.E. Franklin, J.W. Pickens, in: R.A. Kot, J.W. Morris (Eds.), Structure and Properties of Dual-phase Steels, The Metallurgical Society of AIME, New York, 1979, pp. 304–329.
[11] D.K. Matlock, G. Krauss, L.F. Ramos, G.S. Huppi, in: R.A. Kot, J.W. Morris (Eds.), Structure and Properties of Dual-phase Steels, The Metallurgical Society of AIME, New York, 1979, pp. 62–90.

[12] A.M. Sherman, R.G. Davies, W.T. Donlon, in: R.A. Kot, B.L. Bramfitt (Eds.), Fundamentals of Dual-phase Steels, The Metallurgical Society of AIME, New York, 1981, pp. 85–94.
[13] D.A. Korzekwa, D.K. Matlock, G. Krauss, Metall. Trans. A 15 (1984) 1221–1228.
[14] A.M. Sarosiek, W.S. Owen, Mater. Sci. Eng. 66 (1984) 13–34.
[15] R.G. Davies, in: A.T. Davenport (Ed.), Formable HSLA and Dual-phase Steels, The Metallurgical Society of AIME, New York, 1979, pp. 25–39.
[16] G.R. Speich, R.L. Miller, in: R.A. Kot, J.W. Morris (Eds.), Structure and Properties of Dual-phase Steels, The Metallurgical Society of AIME, New York, 1979, pp. 145–182.
[17] J.Y. Koo, M.J. Young, G. Thomas, Metall. Trans. A 11 (1980) 852–854.
[18] N.K. Balliger, T. Gladman, Met. Sci. 15 (1981) 95–108.
[19] A. Rizk, D.L. Bourell, Scripta Metall. 16 (1982) 1321–1324.
[20] D.L. Bourell, A. Rizk, Acta Metall. 31 (1983) 609–617.
[21] R. Priestner, C.L. Aw, Scripta Metall. 18 (1984) 133–136.
[22] H.P. Shen, T.C. Lei, J.Z. Liu, Mater. Sci. Technol. 2 (1986) 28–33.
[23] M.S. Nagorka, G. Krauss, D.K. Matlock, Mater. Sci. Eng. 94 (1987) 183–193.
[24] Y.L. Su, J. Gurland, Mater. Sci. Eng. 95 (1987) 151–165.
[25] A.K. Jena, M.C. Chaturvedi, Mater. Sci. Eng. 100 (1988) 1–6.
[26] B. Grushko, B.Z. Weiss, Scripta Metall. 23 (1989) 865–870.
[27] A. Bhattacharyya, T. Sakaki, G.J. Wenig, Metall. Trans. A 24 (1993) 301–314.
[28] M. Sarwar, R. Priestner, J. Mater. Sci. 31 (1996) 2091–2095.
[29] A. Bag, K.K. Ray, E.S. Dwarakadasa, Metall. Mater. Trans. A 30 (1999) 1193–1202.
[30] W. Bleck, A. Frehn, J. Ohlert, Proceedings of the International Symposium on Niobium Niobium Science and Technology, Orlando, USA, 2001, pp. 727–752.
[31] U. Liedl, S. Traint, E.A. Werner, Comput. Mater. Sci. 25 (2002) 122–128.
[32] F.M. Al-Abbasi, J.A. Nemes, Int. J. Mech. Sci. 45 (2003) 1449–1465.
[33] C.Y. Kung, J.J. Rayment, Metall. Trans. A 13 (1982) 328–331.
[34] C.L. Magee, R.G. Davies, Acta Metall. 20 (1972) 1031–1043.
[35] J.F. Nye, Acta Metall. 1 (1953) 153–162.
[36] M.F. Ashby, Philos. Mag. 21 (1970) 399–424.
[37] E. Kröner, Int. J. Eng. Sci. 1 (1963) 261–278.
[38] G.E. Dieter, Mechanical Metallurgy, third ed., McGraw-Hill, New York, 1986.
[39] B.L. Adams, S.I. Wright, K. Kunze, Met. Trans. A 24 (1993) 819–831.
[40] A.J. Schwartz, M. Kumar, B.L. Adams (Eds.), Electron Backscatter Diffraction in Materials Science, Kluwer Acad/Plenum Publishers, New York, 2000.
[41] F.J. Humphreys, J. Mater. Sci. 36 (2001) 3833–3854.
[42] R. Kaspar, O. Pawelski, Materialprüfung 31 (1989) 14–16.
[43] R. Song, D. Ponge, D. Raabe, R. Kaspar, Acta Mater. 53 (2005) 845–858.
[44] M. Calcagnotto, D. Ponge, D. Raabe, ISIJ Int. 48 (2008), 1096-1011.
[45] M. Calcagnotto, D. Ponge, D. Raabe, Proceedings of the MS&T Conference and Exhibition, Pittsburgh, USA, 2008, CD-Rom.
[46] D. Dingley, J. Microsc. 213 (2004) 214–224.
[47] P.S. Bate, R.D. Knutsen, I. Brough, F.J. Humphreys, J. Microsc. 220 (2005) 36–46.
[48] S. Zaefferer, Ultramicroscopy 107 (2007) 254–266.
[49] J. Konrad, S. Zaefferer, D. Raabe, Acta Mater. 54 (2006) 1369–1380.
[50] N. Zaafarani, D. Raabe, R.N. Singh, F. Roters, S. Zaefferer, Acta Mater. 54 (2006) 1863–1876.
[51] S. Zaefferer, S.I. Wright, D. Raabe, Metall. Mater. Trans. A 39 (2008) 374–389.
[52] A. Bastos, S. Zaefferer, D. Raabe, J. Microsc. 230 (2008) 487–498.
[53] A. Khorashadizadeh, M. Winning, D. Raabe, Mater. Sci. Forum 584–586 (2008) 434–439.
[54] S.B. Lee, A.D. Rollett, G.S. Rohrer, Mater. Sci. Forum 558–559 (2007) 915–920.
[55] A.D. Rollett, S.B. Lee, R. Campman, G.S. Rohrer, Ann. Rev. Mater. Res. 37 (2007) 627–658.
[56] W. Xu, M. Ferry, F.J. Humphreys, Scripta Mater. 60 (2009) 862–865.
[57] W. Xu, M. Ferry, J.M. Cairney, F.J. Humphreys, Acta Mater. 55 (2007) 5157–5167.
[58] W. Xu, M. Ferry, N. Mateescu, J.M. Cairney, F.J. Humphreys, Mater. Charact. 58 (2007) 961–967.
[59] L.P. Kubin, A. Mortensen, Scripta Mater. 48 (2003) 119–125.
[60] H. Gao, Y. Huang, W.D. Nix, J.W. Hutchinson, J. Mech. Phys. Solids 47 (1999) 1239–1263.
[61] E. Demir, D. Raabe, N. Zaafarani, S. Zaefferer, Acta Mater. 57 (2009) 559–569.
[62] D. Raabe, Phys. Stat. Sol. A 149 (1995) 575–581.
[63] D. Raabe, Mater. Sci. Eng. A 197 (1995) 31–37.
[64] M. Calcagnotto, D. Ponge, D. Raabe, Proceedings of the 3rd Internatonal Conference on Thermomechanical Processing of Steels, Padova, Italy, 2008, CD-Rom.
[65] J.M. Moyer, G.S. Ansell, Metall. Trans. A 6 (1975) 1785–1791.
[66] U.F. Kocks, Philos. Mag. 13 (1966) 541–566.
[67] X.L. Cai, J. Feng, W.S. Owen, Metall. Trans. A 16 (1985) 1405–1415.

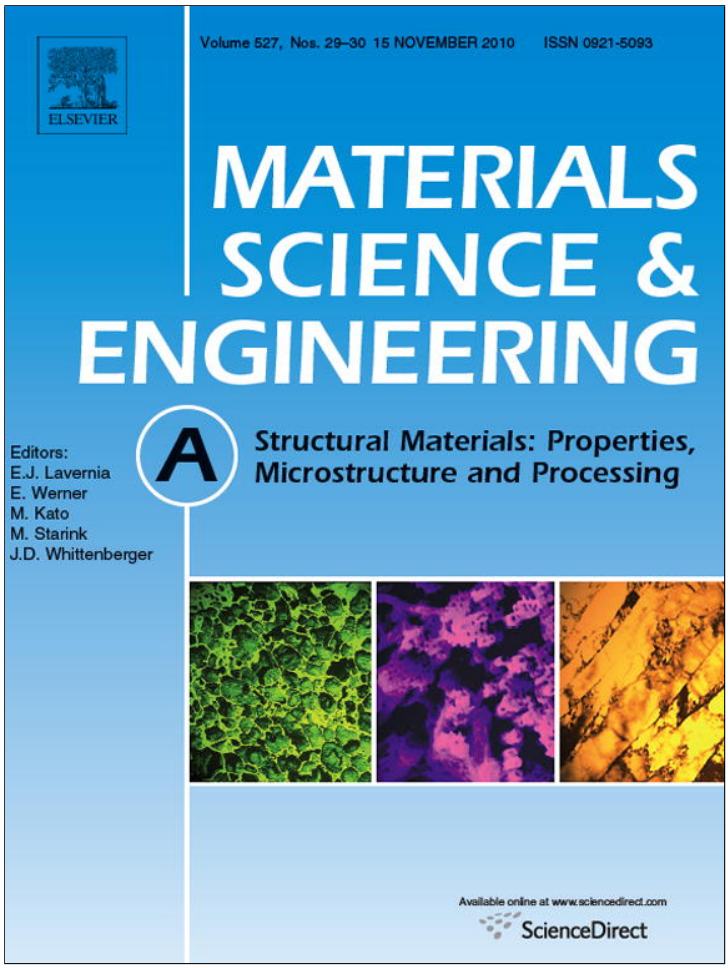

Materials Science and Engineering A 527 (2010) 7832–7840

Contents lists available at ScienceDirect

Materials Science and Engineering A

journal homepage: www.elsevier.com/locate/msea

Effect of grain refinement to 1 μm on strength and toughness of dual-phase steels

Marion Calcagnotto*, Dirk Ponge, Dierk Raabe

Max-Planck-Institut für Eisenforschung GmbH, Max-Planck-Straße 1, 40237 Düsseldorf, Germany

ARTICLE INFO

Article history:
Received 16 June 2010
Received in revised form 19 August 2010
Accepted 24 August 2010

Keywords:
Grain refinement
Dual-phase steel
Ultrafine grains
Toughness
Warm deformation

ABSTRACT

Large strain warm deformation at different temperatures and subsequent intercritical annealing has been applied to obtain fine grained (2.4 μm) and ultrafine grained (1.2 μm) ferrite/martensite dual-phase (DP) steels. Their mechanical properties were tested under tensile and impact conditions and compared to a hot deformed coarse grained (12.4 μm) reference material. Both yield strength and tensile strength follow a Hall–Petch type linear relationship, whereas uniform elongation and total elongation are hardly affected by grain refinement. The initial strain hardening rate as well as the post-uniform elongation increase with decreasing grain size. Ductile fracture mechanisms are considerably promoted due to grain refinement. Grain refinement further lowers the ductile-to-brittle transition temperature and leads to higher absorbed impact energies. Besides the common correlations with the ferrite grain size, these phenomena are explained in terms of the martensite particle size, shape and distribution and the more homogeneous dislocation distribution in ultrafine ferrite grains.

1. Introduction

Dual-phase (DP) steels consisting of a soft ferrite matrix and typically 5–30 vol.% of hard martensite particles combine high strength with good formability and weldability. Therefore, they are widely used for automotive applications. Since their development four decades ago, the microstructure–property relationships have been extensively studied [1–13]. In view of the increasing demands for occupant safety and fuel efficiency, further strengthening of DP steels without a loss in ductility is required. Grain refinement is a promising tool to achieve this aim [14–19]. In the early studies on the grain size effect in DP steels [14,15], the minimum ferrite grain size was around 5 μm due to limitations of the conventional thermomechanical processing routes. In recent years, a variety of new processing routes has been developed to produce ultrafine grained (UFG) low carbon steels with a ferrite grain size of 1 μm and below [20].

UFG DP steels with a ferrite grain size around 1 μm have been produced by applying a two-step processing route consisting of (1) a deformation treatment to produce UFG ferrite and finely dispersed cementite or pearlite and (2) a short intercritical annealing in the ferrite/austenite two-phase field followed by quenching to transform all austenite to martensite. Grain refinement in step (1) was achieved by equal channel angular pressing (ECAP) [16], cold rolling [17] and cold swaging [18]. A single-pass processing route based on deformation induced ferrite transformation (DIFT) was proposed by Mukherjee et al. [21]. It was consistently found that yield strength and tensile strength are increased due to grain refinement, whereas uniform and total elongation are less affected. The strain hardening rate was found to increase with decreasing grain size [16] which is in contrast to the observation of the very restricted strain hardening rate in UFG low carbon ferrite/cementite steels [22,23]. As the number of investigations on this topic is very limited, a better understanding of the mechanical response of DP steels to ferrite grain sizes close to or below 1 μm is required.

In contrast to other methods to increase the strength of steels, grain refinement simultaneously improves the toughness of the material, i.e. its capability to absorb energy under impact conditions. Several studies on UFG ferrite/cementite steels revealed that the ductile-to-brittle transition temperature (DBTT) is significantly reduced due to grain refinement, e.g. [24–26]. However, the grain size dependence of the impact properties of UFG DP steels has not been addressed up to now.

The most distinct mechanical properties of DP steels are the low elastic limit, the high initial strain hardening and the overall continuous yielding in the quenched state. These features have been attributed to residual stresses and dislocation heterogeneities present in the ferrite as a result of the austenite-to-martensite transformation [27–30]. This transformation involves a volume expansion of 2–4%, depending on chemical composition [31], causing an elastically and plastically deformed zone in the ferrite adjacent to martensite [7,32,33]. The elastic stresses facilitate plastic flow during the early stages of yielding. Dislocation–dislocation interaction, dislocation pile-ups at ferrite/martensite interfaces and

* Corresponding author. Tel.: +49 211 6792 416; fax: +49 211 6792 333.
E-mail addresses: m.calcagnotto@mpie.de (M. Calcagnotto), d.ponge@mpie.de (D. Ponge), d.raabe@mpie.de (D. Raabe).

0921-5093/$ – see front matter © 2010 Elsevier B.V. All rights reserved.
doi:10.1016/j.msea.2010.08.062

the corresponding long-range elastic back stresses contribute to rapid strain hardening [4,28]. However, it is not clear to which extent this theory applies to UFG ferrite. Clearly, the dislocation distribution is different in UFG ferrite and consequently, the deformation mechanisms might change.

This study aims at a detailed description of the tensile and impact properties of three DP steels having the same chemical composition but different grain sizes. Unlike in previous studies, the materials presented in this study have roughly the same martensite volume fraction and the same martensite carbon content, so that the individual effect of grain refinement on the overall mechanical properties can be studied more consistently, without the simultaneous change of other microstructure features.

2. Experimental procedures

The chemical composition of the steel used was (in wt.%) 0.17 C, 1.49 Mn, 0.22 Si, 0.033 Al, 0.0033 N, 0.0017 P and 0.0031 S. A lean composition was chosen in order to show that a stable ferrite grain size of around 1 μm can be achieved via thermomechanical processing without the addition of expensive grain growth inhibitors like vanadium or niobium. Previously, it was shown that a certain manganese content is highly beneficial for the grain refining process [34] and essential to achieve sufficient hardenability [35]. The steel was produced by vacuum induction melting. Samples (50 mm × 40 mm × 60 mm) were machined directly from the cast ingot. The thermomechanical processing was realized by use of a large scale 2.5 MN hot deformation simulator located at the Max-Planck-Institut für Eisenforschung [36–38]. This computer controlled servohydraulic press allows to simulate industrial hot rolling processing routes by performing multi-step flat compression tests. The processing schedules to obtain different grain sizes are outlined in Fig. 1. Austenitization at 912 °C for 3 min and subsequent deformation at 860 °C (with a logarithmic strain of $\varepsilon = 0.3$ at a strain rate of $10\,s^{-1}$) produces fully recrystallized austenite which transforms into relatively coarse grained (CG) ferrite and pearlite upon slow cooling, Fig. 1a. Grain refinement is achieved by subsequent warm deformation exerting a four-step flat compression series with a strain of 0.4 per step, an interpass time of 0.5 s and a strain rate of $10\,s^{-1}$. The deformation temperature controls the degree of grain refinement. At 700 °C (Fig. 1b), a fine grained (FG) polygonal ferrite matrix is obtained with small islands of pearlite and globular cementite (FG-route). At 550 °C (Fig. 1c), the ferrite is refined to around 1 μm (which is referred to as UFG ferrite) due to grain subdivision and pronounced recovery [39,38]. The cementite lamellae of the pearlite colonies undergo continuous fragmentation and spheroidization. After a total strain of 1.6, pearlite is completely replaced by spheroidized sub-μm sized cementite which is distributed homogeneously along the ferrite grain boundaries (UFG-route). After warm deformation, specimens were annealed for 2 h at the respective deformation temperature to simulate elevated coiling temperatures. Details about the microstructure evolution during warm deformation and annealing at 550 °C are given in Ref. [38]. To obtain the final ferrite/martensite dual-phase microstructure the specimens were subjected to intercritical annealing in a salt bath furnace. The temperature was controlled electronically and held constant at 730 °C. The samples were annealed for 3 min (including reheating time) in the salt bath, before they were quenched in water to obtain a ferrite/martensite DP structure. These parameters were established by performing dilatometer tests [35].

Cylindrical tensile test specimens with a diameter of 4 mm and a gage length of 20 mm were machined according to the German Industry Norm DIN 50125-B. Tensile tests were conducted at room temperature with a constant cross-head speed of 0.5 mm/min and an initial strain rate of $0.5 \times 10^{-3}\,s^{-1}$. Due to the continuous yielding behavior, the yield strength is given as the 0.2% offset yield strength. The uniform elongation was determined as the strain at which the true strain equals the strain hardening rate (Considère criterion). The strain hardening exponent, n, was determined as an approximation to the Hollomon equation ($\sigma_t = k\varepsilon_t^n$, where σ_t is the true stress, ε_t is the true strain and k is an empirical constant) between 2% and uniform elongation. The reduction in area was determined by measuring the area of the fracture surface related to the initial surface.

V-notched specimens test were cut along the rolling direction with a cross section of 3 mm × 4 mm according to the German Industry Norm DIN 50115. The notch was placed 10 mm from the center of the sample where the local strain equals the nominal strain [40]. Impact tests were carried out in a temperature range of −40 to 200 °C. The temperature was controlled by a thermocouple welded on the specimen surface. The ductile-to-brittle transition temperature (DBTT) was determined using two different approaches. First, it was measured as the temperature corresponding to the half value of the upper shelf energy (USE), determined from the Charpy impact curve. Second, it was defined as the temperature at which 50% of fracture is of brittle type, observed by electron microscopy. The latter is the fracture appearance transition temperature (50%-FATT). The USE and the DBTT obtained using subsize specimen are smaller than the values obtained using fullsize specimen because of the reduced specimen cross section and the different stress state. Kaspar and Faul [41] conducted a comparative study on normalized ferrite/pearlite steels with several chemical compositions and found linear relations of the USE and the DBTT to hold between subsize and fullsize specimen. Although the steel investigated in the present study is different, their correlations are used here as a first approximation to convert the USE and the DBTT to the respective values of conventional Charpy V-notch specimens.

Samples for scanning electron microscopy (SEM) were prepared by standard mechanical grinding and polishing procedures, finishing with 3 min colloidal silica polishing. To reveal the microstructure, the samples were additionally etched in 1% Nital for 3 s.

The martensite volume fraction and the ferrite grain size were determined on the basis of three SEM micrographs taken at a magnification of 3000× for the UFG and FG steel and of 500× for the CG steel. The point counting method was used to determine the second-phase fraction. As it is not possible to differentiate between martensite and austenite on etched specimens in the SEM, the second-phase fraction was determined as the fraction of martensite plus retained austenite. The retained austenite volume fraction was determined to range between 1 and 3 vol.% based on electron backscatter diffraction (EBSD) measurements. The ferrite mean linear intercept (MLI) length was determined both in the compression direction and in the rolling direction. The average value determines the ferrite grain size.

3. Results

3.1. Microstructures

The microstructure obtained after hot deformation and air cooling followed by intercritical annealing (CG-route) consists of a ferrite matrix with a grain size of 12.4 μm and 31.3% martensite, Table 1, the latter occurring partly as isolated islands, partly as aligned bands. By applying multi-pass warm deformation at 700 °C (FG-route) and 550 °C (UFG-route) between hot deformation and intercritical annealing, the ferrite grain size is reduced to 2.4 and 1.2 μm, respectively. The martensite fraction is 30.1 vol.% in the FG steel and 29.8 vol.% in the UFG steel. The martensite islands are

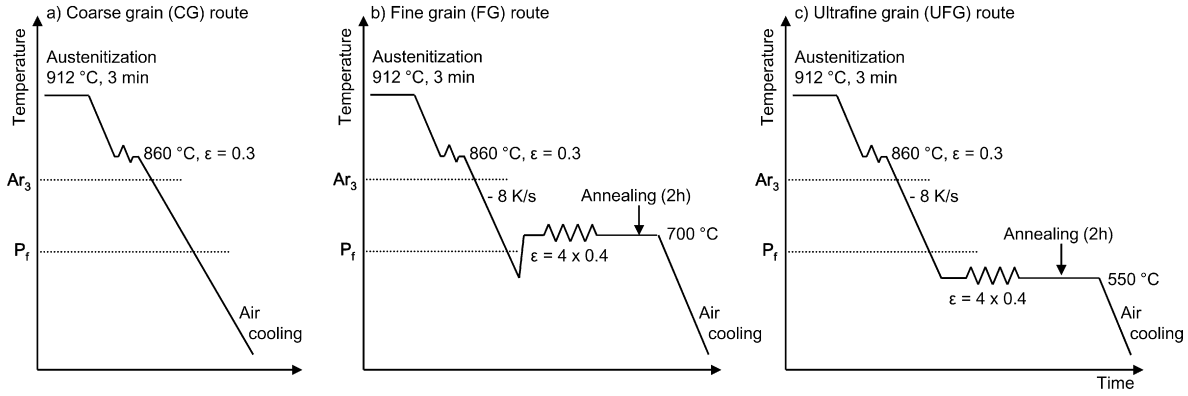

Fig. 1. Thermomechanical processing routes to produce different grain sizes in a hot deformation simulator. Ar_3: non-equilibrium transformation start temperature, P_f: pearlite transformation finish temperature, ε: logarithmic strain.

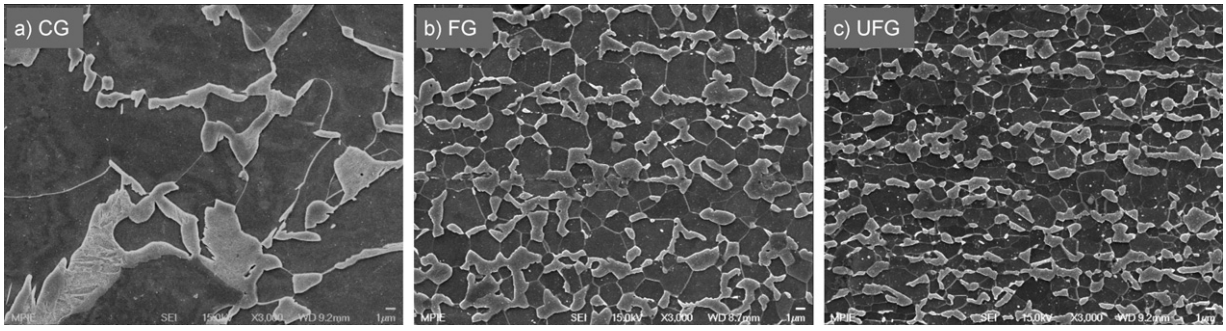

Fig. 2. Microstructures used to evaluate the effect of grain refinement on mechanical properties. The (a) coarse grained (CG), (b) fine grained (FG) and (c) ultrafine grained (UFG) material were produced by the processing routes illustrated in Fig. 1 plus intercritical annealing for 3 min at 730 °C in a salt bath, followed by water quenching. Rolling direction is horizontal, compression direction is vertical.

mainly isolated. Exemplary micrographs are shown in Fig. 2, the magnification being the same in all images.

As neither the chemical composition, nor the intercritical annealing temperature or holding time was changed, all three steels contain similar martensite fractions with presumably similar martensite carbon contents. Using a mass balance calculation, the martensite carbon content C_m can be estimated from the equation

$$C_m = \frac{C_c - C_f(1 - f_m)}{f_m} \quad (1)$$

where C_c is the carbon content of the composite, C_f is the carbon content of ferrite and f_m is the martensite volume fraction. The ferrite carbon content was estimated using Thermo-Calc [42]. It was assumed that upon water quenching, the ferrite keeps the carbon content which is present at the temperature where the austenite fraction is 30 vol.%. Thus, ferrite is supersaturated in carbon, the carbon content being 0.01 wt.%. Inserting this value in Eq. (1) yields a martensite carbon content of 0.54 wt.%.

Other authors conducting similar investigations [16,18] found that phase transformation kinetic is enhanced upon grain refinement. Hence, they report a higher martensite volume fraction in their UFG materials after the same intercritical annealing treatment. The reason why the martensite volume fraction is nearly the same for all grain sizes in the present case is probably the different processing route applied. Due to the pronounced recovery during large strain warm deformation [38], the stored energy in the initial microstructure might be lower than in the materials processed by ECAP [16] or cold swaging [18]. Hence, the driving force for phase transformation is not profoundly enhanced in the present case. This leads to the advantageous situation that in this study, the differences in the mechanical properties can be solely attributed to the different grain size and these effects are not overlaid by differences in martensite volume fraction. However, it will be shown in the following, that the martensite distribution and the crystallographic texture have a considerable influence on the mechanical behavior.

3.2. Tensile properties

Fig. 3 shows the engineering stress–strain curves of the coarse grained, the fine grained, and the ultrafine grained DP steels. For each material, the result of only one of the three tensile tests is shown, because the variations within each series are rather small. The steels show the typical behavior of as-quenched ferrite/martensite dual-phase steels: low elastic limit, absence of a distinct yield point, continuous yielding and high initial strain hardening rate. With decreasing grain size, the tensile strength is remarkably increased whereas uniform elongation and total elongation are only slightly affected.

Table 1
Microstructure parameters obtained from SEM micrographs and tensile data presented as average value of three tensile specimen for each group. MVF: martensite volume fraction, d_f: ferrite grain size, YS: 0.2% offset yield strength, UTS: ultimate tensile strength, UE: uniform elongation, TE: total elongation, RIA: reduction in area.

Steel	MVF (%)	d_f (μm)	YS (MPa)	UTS (MPa)	UE (%)	TE (%)	RIA (%)	Yield ratio	n (2%-UE)
CG	31.3	12.4	445	870	7.2	7.7	13.0	0.51	0.21
FG	30.1	2.4	483	964	7.4	8.9	18.7	0.50	0.18
UFG	29.8	1.2	525	1037	7.1	7.3	15.3	0.51	0.18

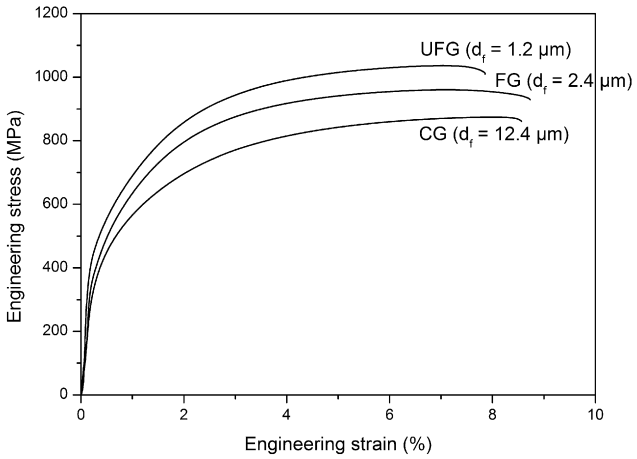

Fig. 3. Exemplary engineering stress–strain curves of the steels with coarse grained (CG), fine grained (FG) and ultrafine (UFG) ferrite matrix. Ferrite grain size (d_f) is given in brackets.

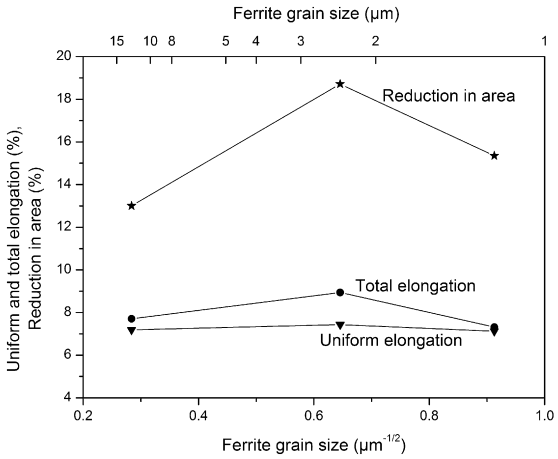

Fig. 5. Effect of grain refinement on ductility. The data points represent average values from three separate tensile tests for each steel.

Figs. 4–7 show average values for each steel obtained from three separate tensile tests which are listed in Table 1. The increase in yield strength (0.2% offset yield strength) and tensile strength (Fig. 4) follow a linear trend which was expected as the grain size and strength are related by a linear relationship given by the Hall–Petch equation ($\sigma_y = \sigma_0 + k_y d^{-1/2}$ where σ_y is the yield strength, d is the grain size, σ_0 is the friction stress required to move dislocations in a ferrite single crystal and k_y is the Hall–Petch slope quantifying the resistance against slip propagation across a grain boundary).

The grain size dependence (Hall–Petch coefficient) is 8.39 MPa/$d^{-1/2}$ (with d being the grain diameter in mm) for the tensile strength, and it is 4.0 MPa/$d^{-1/2}$ for the yield strength. These values are in the common range reported for dual-phase steels [43]. However, the Hall–Petch coefficient of the yield strength is lower than in ferrite/cementite steels that are refined to 1 μm and below [44]. This indicates that other phenomena like residual stresses and mobile dislocations, as described in the introduction, exert a strong influence on the yield strength of dual-phase steels. As yield and tensile strength are increased by about the same factor due to grain refinement, the yield ratio is nearly constant.

The effect of grain refinement on ductility is more complex than its effect on strength. The uniform elongation (Fig. 5) is nearly con-

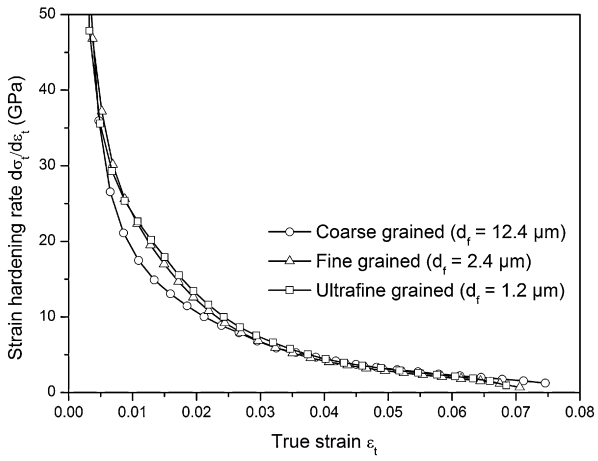

Fig. 6. Strain hardening rate as a function of true strain (average values from three tensile tests). Grain refinement increases the initial strain hardening rate. d_f: ferrite grain size.

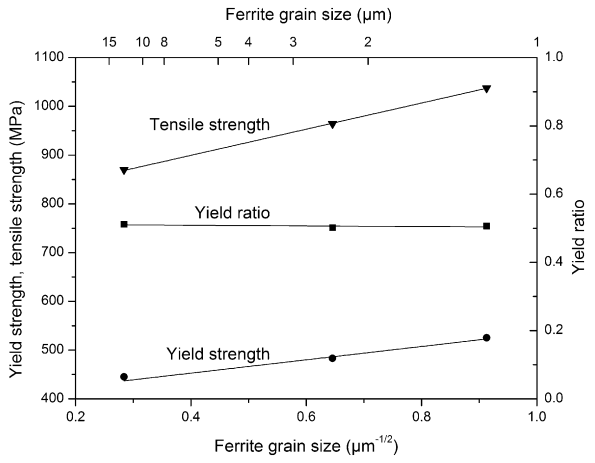

Fig. 4. Effect of grain refinement on yield strength (0.2% offset) and tensile strength. The data points represent average values from three separate tensile tests for each steel.

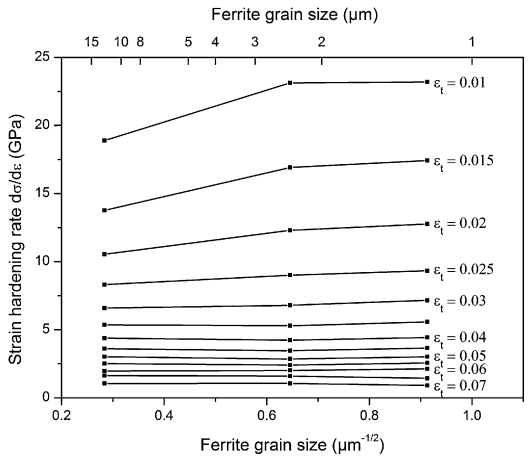

Fig. 7. Strain hardening rate at different true strain levels ε_t as a function of grain size, calculated as average values from three tensile test data.

stant around 7% for all steels. Both total elongation and reduction in area are highest in the FG steel. The UFG steel has a lower total elongation than the CG steel, but a higher reduction in area. However, the differences are rather small.

The analysis of the strain hardening rate (Fig. 6) reveals that the initial strain hardening rate is increased by grain refinement, but is nearly the same for the FG and the UFG steel. At higher strain levels, the two curves converge with the curve of the CG steel.

The effect of grain size on strain hardening behavior is more clearly revealed by plotting the average strain hardening rate of the three tensile specimens at different strain levels as a function of grain size, Fig. 7. It is obvious from this figure that grain refinement promotes initial strain hardening rate. At higher strains, the effect of grain refinement continuously decreases. At a true strain of around 0.07, the strain hardening rate of the ultrafine grained steel is slightly smaller than in the other steels. The *n*-value, calculated at strain levels between 2% and uniform elongation (Table 1), drops off slightly from 0.21 for the CG steel to 0.18 for the FG and UFG steel.

Fig. 8 shows the tensile specimens after failure. The post-uniform elongation increases with decreasing grain size which is clearly revealed by the more pronounced necking. The micrographs reveal the respective fracture modes of the steels. In case of the CG steel, it is mainly brittle, which is documented by well-defined facets and cleavage steps on these facets, Fig. 8a. Only some small areas consist of dimples. The latter are located in the martensitic area, whereas the ferrite exhibits cleavage planes. The dominant fracture mode of the FG steel is ductile, although smaller parts of the specimen have undergone brittle fracture, Fig. 8b. The UFG steel shows dimples throughout the specimens, Fig. 8c. This suggests a failure process of void nucleation and growth and hence, entirely ductile fracture. Some dimples are formed around inclusions which are probably manganese sulphides.

To find out the preferred void nucleation sites, surfaces perpendicular to the fracture surface were also analyzed. In the CG steel, the main fracture mechanism is martensite cracking. The cracks form mostly in the banded areas perpendicular to the applied tensile strain, Fig. 9a. The main part of the cracks stop at the ferrite/martensite interface, but some travel through a minor fraction of the adjacent ferrite grain. Martensite fracture was observed at strains as low as 3.4% plastic strain. Void nucleation and growth along ferrite/martensite interfaces occurs to a lesser extent within the areas of isolated martensite islands. In the FG and UFG steels, the voids form primarily at ferrite/martensite interfaces and are distributed more homogeneously, Fig. 9b. Martensite cracking takes place less frequently in martensite islands which exceed the average martensite island size and occurs only after necking has started.

3.3. Toughness

The Charpy impact curves for the CG, FG and UFG steel are depicted in Fig. 10a. In Table 2, both the raw data obtained from the subsize specimen (index "s") and the recalculated values for full size specimen (index 'C') are listed.

Both the upper shelf energy (USE) and the lower shelf energy (LSE) are enhanced continuously with ferrite grain refinement. The ductile-to-brittle transition temperature (DBTT), defined as the temperature at half USE, decreases from 127 °C for the CG steel to 100 °C for the FG steel and 94 °C for the UFG steel. This method of determining the transition temperature has the shortcoming that the microstructure is not taken into account. Therefore, the temperature at which the fracture mode is 50% brittle and 50% ductile (fracture appearance transition temperature, 50%-FATT), was determined additionally. While the 50%-FATT of the CG steel (132 °C) is similar to the value determined by the half USE (124 °C), it is 24 °C lower in case of the FG steel and 33 °C lower in the case of the UFG steel, Fig. 10b. This means that the FG steel and (more strongly) the UFG steel are able to deform plastically and therefore, to absorb more energy, at relatively low impact temperatures. This is reflected by the gradual decrease of the absorbed energy at low temperatures for the FG and UFG steel, Fig. 10a. In contrast, the curve of the CG steels exhibits a sharp drop in the absorbed energy between the USE and LSE.

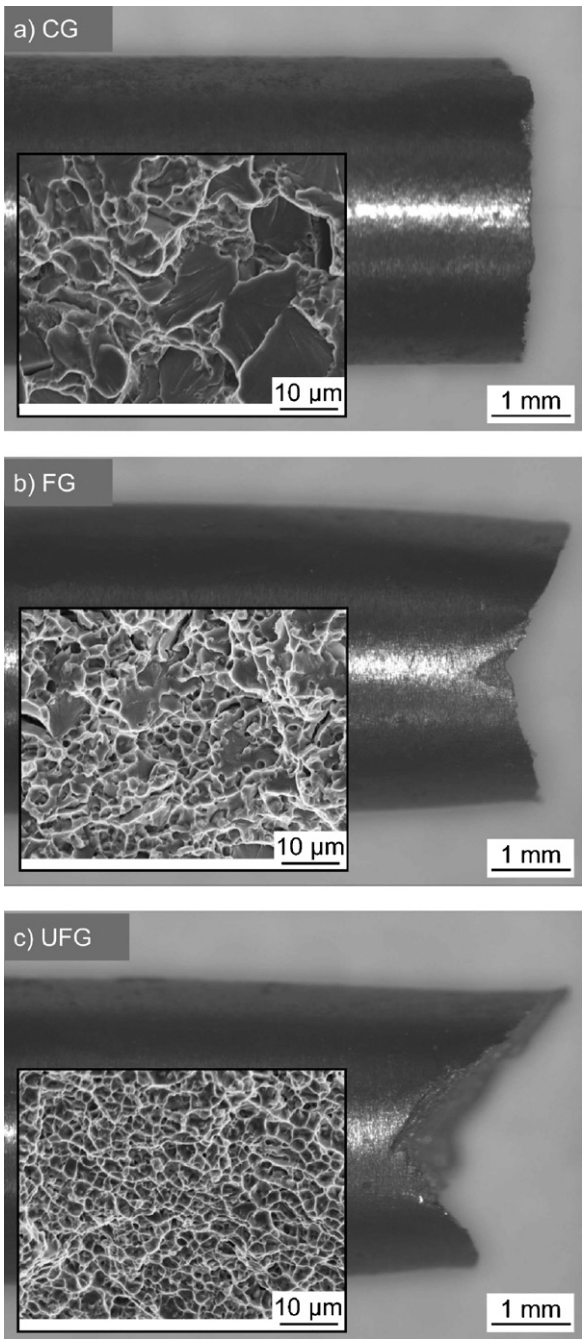

Fig. 8. Tensile specimen after failure showing the increase in post-uniform elongation with decreasing grain size and the promotion of ductile fracture mechanism.

Experimental evidence for the ability of the FG and UFG steel to deform plastically even close to the LSE is found by observing the fractured surfaces broken at room temperature, Fig. 11. While the CG steel fractures in a dominantly brittle manner, the UFG steel fails by void nucleation and growth. The main part of the FG steel shows ductile fracture as well, but some brittle fracture marks occur.

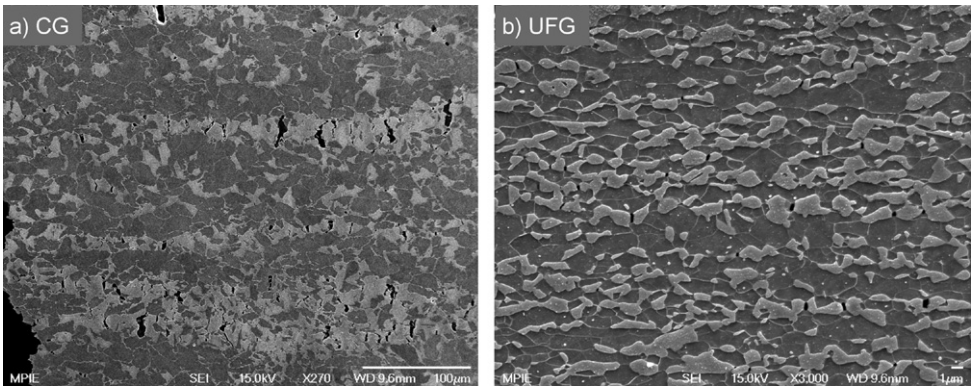

Fig. 9. Observation of the planes perpendicular to the fractured tensile specimen surfaces reveals (a) martensite cracking as the main fracture mechanism in the CG specimen and (b) void nucleation and growth in the UFG specimen. Note the different magnification of the images. The tensile direction is horizontal.

Both the FG and the UFG steel show some secondary fracture along the rolling direction (arrows in Fig. 11). This splitting phenomenon, sometimes referred to as delamination, is commonly observed in hot-rolled high strength steels and was found to exert a considerable effect on the energy absorption and on the DBTT [45].

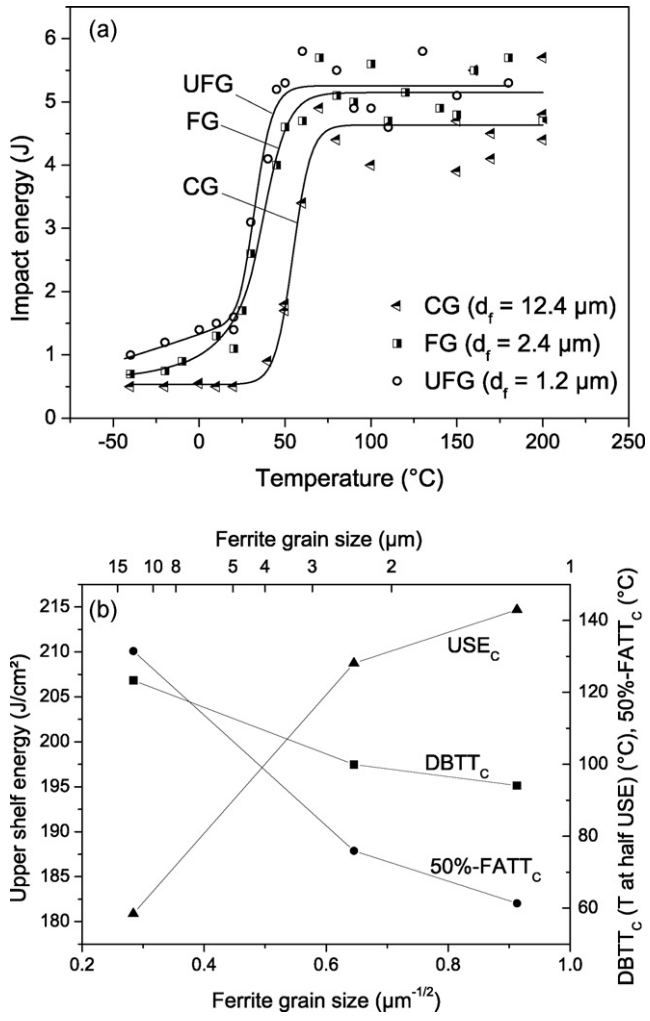

Fig. 10. Energy absorption curves obtained from subsize Charpy V-notch impact tests (a) and the impact data obtained by recalculating the values to full size specimen using the equations recommended by Kaspar and Faul [41] (b). USE: upper shelf energy, DBTT: ductile-to-brittle transition temperature, 50%-FATT: 50% ductile fracture appearance transition temperature, d_f: ferrite grain size.

It is seen that grain refinement enhances toughness in terms of both absorbed energy (USE and LSE) and transition temperature (T at half USE and 50%-FATT). The increase in toughness in the present case is due to the refinement of both ferrite and martensite, as the effective grain size in martensite (the coherent length of {0 0 1} plane in martensite packet) is also reduced [46]. In fact, it was calculated from EBSD scans that the average packet size (taking only HAGBs into account) is 0.9 µm in the CG steel and 0.5 µm in the UFG steel. A secondary reason for the deteriorated toughness of the CG steel is the partial banding of martensite, Fig. 9a. It was shown in previous studies that a fine distribution of martensite leads to improved impact properties when compared to fully banded microstructures [47].

4. Discussion

4.1. Strength and ductility

In general, the enhancement in strength due to grain refinement is accompanied by a deterioration of ductility. However, it was shown in previous studies [14–19] that this does not apply to DP steels. Instead, it was shown, that uniform and total elongation are only slightly affected by a decreasing ferrite grain size, as it is also observed in the present study. The grain size dependence of the mechanical properties is illustrated in Fig. 12. The data are in good agreement with the previous results. The differences in the Hall–Petch slopes result from the different processing routes and chemical compositions applied.

The increase in yield and tensile strength at roughly constant uniform and total elongation was explained with an increase in strain hardening rate with decreasing grain size [5,15,16,43]. A higher strain hardening rate delays the onset of necking and therefore, increases uniform elongation. Figs. 5–7 confirm these findings. Grain refinement increases strain hardening rate at low strains, at higher strains it levels off and equals the rate of the coarse grained reference material. This leads to a nearly unchanged uniform elongation with decreasing grain size. There are several explanations for this behavior. Firstly, the higher fraction of grain boundaries and heterophase interfaces increases the number of dislocation sources, giving rise to rapid increase in dislocation density and thus, strength [48]. Balliger and Gladman [5] further demonstrated that the strain hardening rate of DP steels is dependent on $(f/d)^{1/2}$ where f is the volume fraction of second phase and d is the mean second-phase diameter. Thus, at a constant martensite volume fraction, the strain hardening rate is increased with decreasing martensite island size. Son et al. [16] explain the increase in initial strain hardening rate due to grain refinement with the dislocation distribution in ferrite. In their coarse grained microstructure, the dislocation density

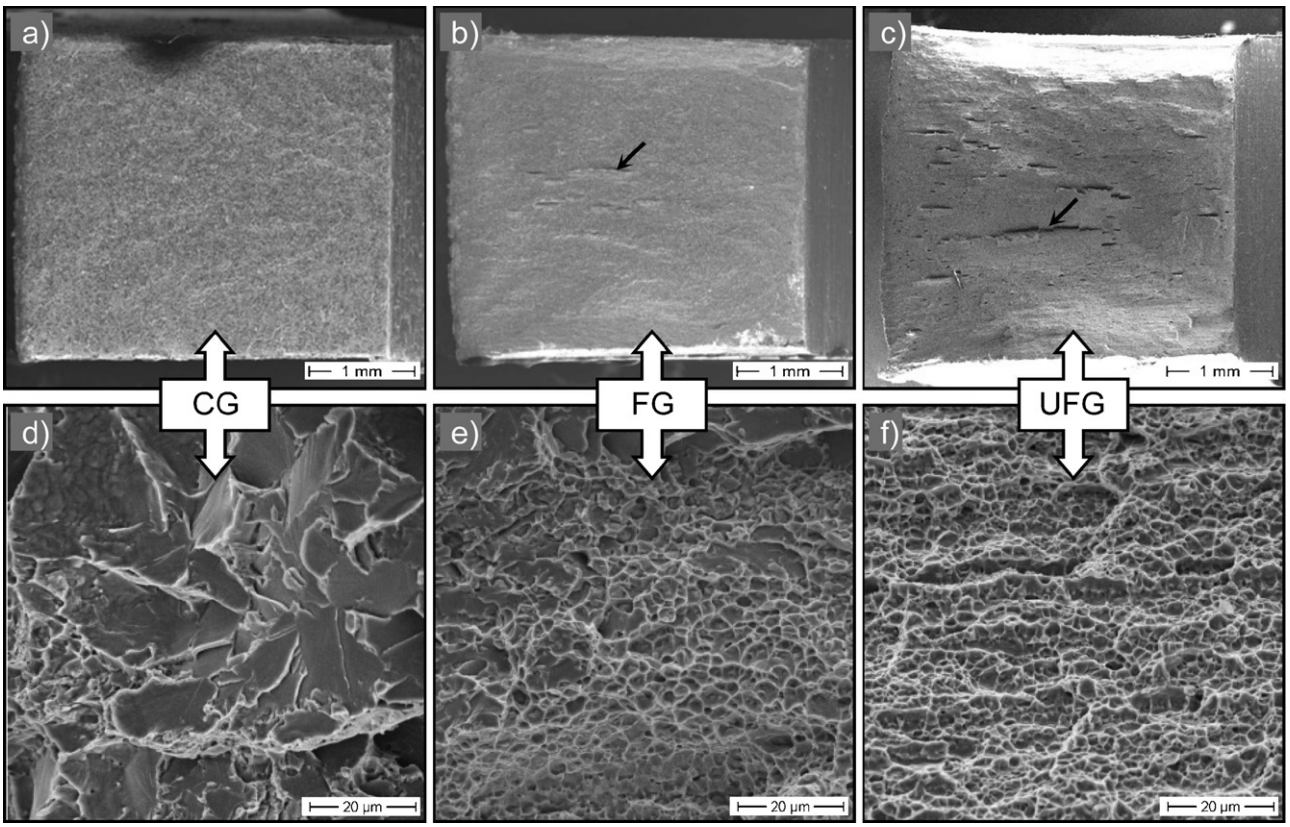

Fig. 11. Fracture surfaces of subsize Charpy impact specimen fractured at room temperature. Like in the tensile specimen, grain refinement promotes ductile failure. Some delamination occurs in the FG and the UFG specimen (arrows). Rolling direction is horizontal.

is very high close to the ferrite/martensite interface and low in the ferrite center, whereas in the ultrafine grained structure (~1 μm) it is high throughout the ferrite grains. Therefore, strain hardening by dislocation intersections is more rapid in the UFG microstructure. In fact, we observed [49] by using 3D-EBSD tomography, that ferrite grains smaller than 1 μm^3 can be entirely affected by the strain accommodation due to the martensitic phase transformation. In larger grains, the deformed zone does not extend to the ferrite grain interior. Therefore, we confirm the more homogeneous distribution of a high dislocation density described by Son et al. [16] for grains below 1 μm^3. Besides the stress increment due to rapid dislocation interaction as proposed by the authors, we assume that the plasticity of the ultrafine ferrite grains is restricted due to the high average dislocation density. Larger ferrite grains, which are always present in this type of microstructure, contain areas which are unaffected by the martensitic phase transformation. These grains will carry the main part of the strain during the initial stages of tensile straining, whereas the ultrafine ferrite grains will partly act as load carrying phase. Like the martensite phase, the ultrafine ferrite grains thus exert elastic back stresses due to the plastic incompatibility that contribute to the high initial strain hardening rate.

In view of low strain levels below 2%, it must be stated that the increase in yield strength due to ferrite grain refinement might affect the high initial strain hardening rate. Due to the absence of a distinct yield point, it is not possible to clearly distinguish between the effect of grain size on strain hardening rate and on yield strength. In this context, the investigation of the strain hardening rate after bake-hardening, i.e. after a heat treatment at 170 °C which leads to the reoccurrence of a yield point, would offer valuable information.

Another reason for the nearly constant uniform elongation with decreasing grain size might be the presence of small amounts (1–3 vol.%) of retained austenite in the UFG steel which is partly of isolated and partly of interlath type [35]. It was found from EBSD data that the amount of retained austenite is below 1% in the specimen area of uniform elongation and 0% in the necked area. That means, retained austenite transformed to martensite during tensile straining, supplying fresh dislocations to the microstructure which contribute to strain hardening and thus delay necking. This transformation induced plasticity (TRIP) effect is often considered to be negligible in DP steels because of the low volume fractions of retained austenite obtained, but was also shown to increase the uniform and total elongation due to an increase in strain hardening rate before the onset of necking [50–52]. In contrast to the UFG steel, the CG steel does not contain retained austenite. The stability of austenite is higher in the UFG steel due to (1) a size stabilization effect [4,53] and (2) a higher Mn content due to Mn enrichment during warm deformation [35]. Although the effect of retained austenite

Table 2
Charpy impact data obtained from the subsize specimen (index 's') and converted to values for full size Charpy V-notch (index 'C') specimen using the correlations given by Kaspar and Faul [41]. USE: upper shelf energy, DBTT: ductile-to-brittle transition temperature (temperature at 50% of USE), FATT: fracture appearance transition temperature.

Steel	USE_S (J)	USE_C (J/cm^2)	$DBTT_S$ (°C)	$DBTT_C$ (°C)	50%-$FATT_S$ (°C)	50%-$FATT_C$ (°C)
CG	4.6	181	53	123	60	131
FG	5.1	209	33	100	12.5	76
UFG	5.3	215	28	94	0	61

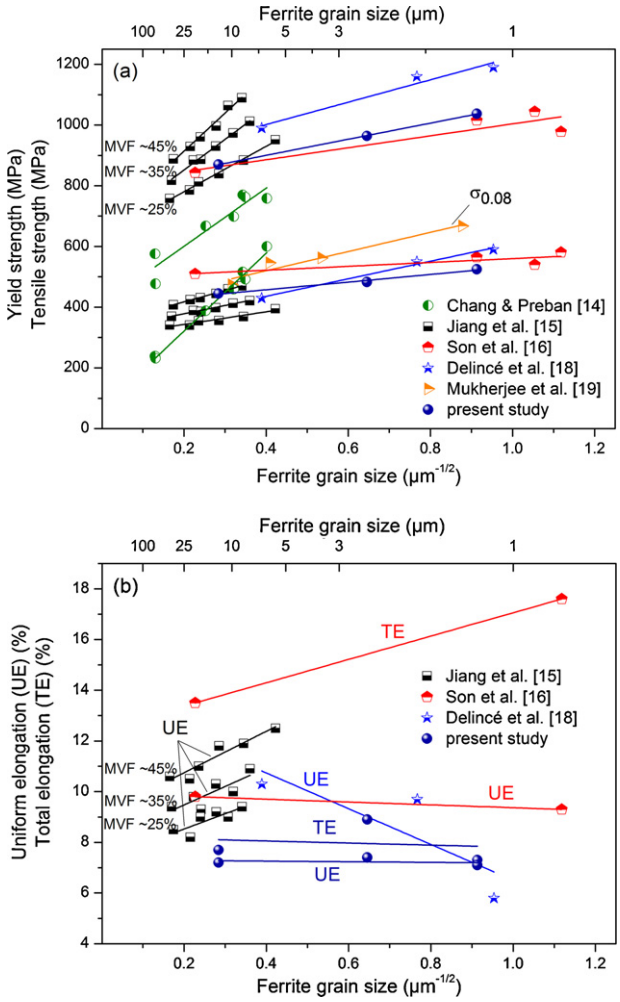

Fig. 12. Grain size dependence of (a) yield and tensile strength and (b) uniform and total elongation. MVF: martensite volume fraction, $\sigma_{0.08}$: flow stress at 8% strain, UE: uniform elongation, TE: total elongation.

transformation on the overall mechanical properties is presumably small, it should not be neglected.

4.2. Fracture mechanisms

The increased ductility due to grain refinement is reflected in the fracture mechanisms of the steels. At room temperature, the UFG steel shows ductile fracture mechanisms in response to both tensile and impact conditions, the CG steel shows mainly brittle behavior and the FG steel exhibits an intermediate fracture mechanism.

Brittle fracture behavior is favored due to martensite banding, large martensite island size and unfavorable distribution along ferrite grain boundaries in the CG steel. Voids and cracks are distributed mainly around martensite bands, Fig. 9a. Here, the local stress concentrations are highest as the stress relaxation by deformation of adjacent ferrite grains is restricted. As the plasticity of CG martensite is very low, premature martensite cracking or void nucleation at the interphase interface occurs. Martensite cracking is supported by the presence of former austenite–austenite grain boundaries which are known to be brittle due to their high susceptibility to segregations [54]. Moreover, it is possible that the banded martensite contains more carbon than the isolated martensite due to Mn segregation which acts as a sink for carbon. Therefore, it is likely that the banded martensite is less deformable and undergoes brittle fracture more easily. Davies [43] and Marder [55] found that martensite cracking is greatest when the carbon content is high and when the martensite is banded. As a consequence, premature martensite cracking controls both tensile strength and uniform elongation in the CG steel.

Kunio et al. [56] introduced the idea that connected martensite is the site of the incipient cracks which trigger cleavage in the ferrite. According to Uggowitzer and Stüwe [57], the fractured martensite acts as a sharp notch, leading to cleavage in ferrite. In the present case, martensite cracks are stopped by the ferrite in the CG steel but penetrate deeper into the ferrite grain with increasing strain. Close to the tensile strength, plastic constraints are too high to impede the crack penetration, and ferrite fails by cleavage. In the other steels, martensite cracking is less frequent and does not lead to ferrite cleavage fracture.

The fracture of martensite in the present study is at least in some parts of ductile nature, whereas the adjacent ferrite fails by cleavage. This fracture type was reported for DP steels previously [10,58,59]. As stress is transferred to martensite during tensile straining of DP steels, the fracture stress in martensite is reached much earlier than in ferrite. Therefore, ductile fracture of martensite is initiated. However, the initiated microcracks impose a high shear stress on the neighboring ferrite which increases with the martensite effective grain size. Hence, coarse martensite leads to cleavage fracture of ferrite, whereas the stresses produced by the fracture of fine or ultrafine martensite can be accommodated by plastic deformation of ferrite. Moreover, it is known that the plastic strain needed for the failure of a particle (or grain) increases with decreasing particle size. This behavior was repeatedly observed in DP steels [58,10] and is explained by the smaller number of dislocations piling-up at grain and phase boundaries which result in lower shear stresses. Kim and Thomas [60] found that coarse DP structures fracture predominantly by cleavage, while both fine fibrous and fine globular structures fracture in a ductile manner. They attribute this behavior to the constrained possibility of deformation localization in the fine structures which reduces the probability of cleavage crack nucleation in ferrite. The deformation mechanisms of ferrite and martensite are the subject of another paper recently submitted by our group.

The promotion of ductile fracture behavior is further revealed by the improved Charpy impact properties due to grain refinement, Fig. 10. Grain refinement increases the cleavage fracture stress by reducing the maximum size of a crack and thus, the stress at the crack tip. This leads to the decrease of the ductile-to-brittle transition temperature. Consequently, at low impact temperatures, the FG and the UFG material are capable of undergoing ductile fracture behavior more readily than the CG material, leading to a lower 50%-FATT temperature and an increase in the lower shelf energy (LSE). Additionally, texture effects might play an important role [25]. In the CG material, texture is nearly random, whereas the FG and UFG steels exhibit a strong bcc rolling texture due to large strain warm deformation. Furthermore, the ferrite grains are slightly elongated and inclusions are aligned with the rolling directions. These features promote the occurrence of delaminations within the rolling plane [26,61,62], as revealed in Fig. 11b and c. Delaminations were found to reduce the triaxial stress state at the head of a propagating crack and to blunt the crack tip when the crack and delaminations planes intersect [63]. Thus, more energy can be absorbed at lower temperatures.

At high impact test temperatures, it is obvious that the FG and UFG steel absorb more energy than the CG steel. The higher initial strain hardening rate of the FG and UFG steels might contribute to the higher upper shelf energy (USE). Yet, the scatter of the data is rather high. This may be caused by tempering effects. Therefore, a further interpretation of the grain size effect on the USE does not seem to be reasonable.

5. Conclusions

Three low carbon dual-phase steels with nearly constant martensite fraction around 30 vol.% martensite and different ferrite grain size (1.2, 2.4 and 12.4 μm) were produced by applying hot deformation and large strain warm deformation at different deformation temperatures, followed by intercritical annealing. Their mechanical properties were studied based on tensile and impact test data and microstructure observations. The main conclusions are:

- Grain refinement leads to an increase of both yield strength and tensile strength following a linear relationship of Hall–Petch type. Uniform elongation and total elongation are hardly affected. The initial strain hardening rate and the post-uniform elongation increase as the grain size decreases.
- The increase in the initial strain hardening rate due to grain refinement is attributed to early dislocation interactions, the high number of dislocation sources and the back stresses exerted by (1) martensite islands and (2) ultrafine ferrite grains below 1 μm^3. The presence of small amounts of retained austenite in the ultrafine grained steel might play a secondary role.
- Impact toughness is improved by grain refinement which is revealed by a lower ductile-to-brittle transition temperature and an increase in both upper and lower shelf energy.
- Grain refinement promotes ductile fracture mechanisms in response to both tensile and impact conditions. The formation of martensite cracks and cleavage fracture in ferrite is suppressed in the fine grained and the ultrafine grained steels due to the small size, the more homogeneous distribution and more spherical shape of martensite islands.

References

[1] H. Fischmeister, B. Karlsson, Z. Metallkd. 68 (1977) 311–327.
[2] R.G. Davies, Metall. Trans. A 10 (1979) 1549–1555.
[3] D.K. Matlock, G. Krauss, L.F. Ramos, G.S. Huppi, in: R.A. Kot, J.W. Morris (Eds.), Structure and Properties of Dual-phase Steels, The Metallurgical Society of AIME, New York, USA, 1979, pp. 62–90.
[4] J.M. Rigsbee, P.J. Vander Arend, in: A.D. Davenport (Ed.), Formable HSLA and Dual-phase Steels, The Metallurgical Society of AIME, New York, USA, 1979, pp. 58–86.
[5] N.K. Balliger, T. Gladman, Met. Sci. 15 (1981) 95–108.
[6] G.R. Speich, A.B. Miller, in: R.A. Kot, B.L. Bramfitt (Eds.), Fundamentals of Dual-phase Steels, The Metallurgical Society of AIME, New York, USA, 1981, pp. 279–304.
[7] D.L. Bourell, A. Rizk, Acta Metall. 31 (1983) 609–617.
[8] D.A. Korzekwa, D.K. Matlock, G. Krauss, Metall. Trans. A 15 (1984) 1221–1228.
[9] A.M. Sarosiek, W.S. Owen, Mater. Sci. Eng. 66 (1984) 13–34.
[10] Y.L. Su, J. Gurland, Mater. Sci. Eng. 95 (1987) 151–165.
[11] M. Sarwar, R. Priestner, J. Mater. Sci. 31 (1996) 2091–2095.
[12] O. Bouaziz, T. Iung, M. Kandel, C. Lecomte, J. Phys. IV 11 (2001) 223–231.
[13] F.M. Al-Abbasi, J.A. Nemes, Int. J. Mech. Sci. 45 (2003) 1449–1465.
[14] P.H. Chang, A.G. Preban, Acta Metall. 33 (1985) 897–903.
[15] Z.H. Jiang, Z.Z. Guan, J.S. Lian, Mater. Sci. Eng. A 190 (1995) 55–64.
[16] Y.I. Son, Y.K. Lee, K.T. Park, C.S. Lee, D.H. Shin, Acta Mater. 53 (2005) 3125–3134.
[17] P. Tsipouridis, E. Werner, C. Krempaszky, E. Tragl, Steel Res. Int. 77 (2006) 654–667.
[18] M. Delincé, Y. Brechet, J.D. Embury, M.G.D. Geers, P.J. Jacques, T. Pardoen, Acta Mater. 55 (2007) 2337–2350.
[19] K. Mukherjee, S.S. Hazra, M. Militzer, Metall. Mater. Trans. A 40A (2009) 2145–2159.
[20] R. Song, D. Ponge, D. Raabe, J.G. Speer, D.K. Matlock, Mater. Sci. Eng. A 441 (2006) 1–17.
[21] K. Mukherjee, S. Hazra, P. Petkov, M. Militzer, Mater. Manuf. Process. 22 (2007) 511–515.
[22] K.T. Park, Y.S. Kim, J.G. Lee, D.H. Shin, Mater. Sci. Eng. A 293 (2000) 165–172.
[23] N. Tsuji, N. Kamikawa, R. Ueji, N. Takata, H. Koyama, D. Terada, ISIJ Int. 48 (2008) 1114–1121.
[24] T. Hanamura, F. Yin, K. Nagai, ISIJ Int. 44 (2004) 610–617.
[25] R. Song, D. Ponge, D. Raabe, Acta Mater. 53 (2005) 4881–4892.
[26] Y. Kimura, T. Inoue, F. Yin, O. Sitdikov, K. Tsuzaki, Scripta Mater. 57 (2007) 465–468.
[27] S. Hayami, T. Furukawa, in: M. Korchynsky (Ed.), Microalloying 75 Proceedings of an International Symposium on High-Strength, Low-Alloy Steels, Union Carbide Corporation, New York, USA, 1977, pp. 311–320.
[28] G.R. Speich, R.L. Miller, in: R.A. Kot, J.W. Morris (Eds.), Structure and Properties of Dual-phase Steels, The Metallurgical Society of AIME, New York, USA, 1979, pp. 145–182.
[29] T. Sakaki, K. Sugimoto, T. Fukuzato, Acta Metall. 31 (1983) 1737–1746.
[30] Q.A. Chen, R. Kaspar, O. Pawelski, Z. Metallkd. 76 (1985) 348–352.
[31] J.M. Moyer, G.S. Ansell, Metall. Trans. A 6 (1975) 1785–1791.
[32] G. Tither, M. Lavite, JOM 27 (1975) 15–23.
[33] M. Grujicic, T. Erturk, W.S. Owen, Mater. Sci. Eng. 82 (1986) 151–159.
[34] R. Song, D. Ponge, D. Raabe, ISIJ Int. 45 (2005) 1721–1726.
[35] M. Calcagnotto, D. Ponge, D. Raabe, ISIJ Int. 48 (2008) 1096–1101.
[36] O. Pawelski, R. Kaspar, Materialprüfung 30 (1988) 357–360.
[37] R. Kaspar, O. Pawelski, Materialprüfung 31 (1989) 14–16.
[38] R. Song, D. Ponge, D. Raabe, R. Kaspar, Acta Mater. 53 (2005) 845–858.
[39] A. Belyakov, T. Sakai, H. Miura, R. Kaibyshev, K. Tsuzaki, Acta Mater. 50 (2002) 1547–1557.
[40] J.S. Distl, A. Streißelberger, R. Kaspar, U. Zeislmair, Materialprüfung 27 (1985) 131–135.
[41] R. Kaspar, H. Faul, Materialprüfung 43 (2001) 18–21.
[42] B. Jansson, M. Schalin, M. Selleby, B. Sundman, in: C.W. Bale, G.A. Irons (Eds.), Computer Software in Chemical and Extractive Metallurgy, The Metallurgical Society of CIM, Quebec, Canada, 1993, pp. 57–71.
[43] R.G. Davies, Metall. Trans. A 9 (1978) 671–679.
[44] K. Takeda, N. Nakada, T. Tsuchiyama, S. Takaki, ISIJ Int. 48 (2008) 1122–1125.
[45] M. Yang, Y.J. Chao, X. Li, D. Immel, J. Tan, Mater. Sci. Eng. A 497 (2008) 462–470.
[46] S. Morito, H. Saito, T. Ogawa, T. Furuhara, T. Maki, ISIJ Int. 45 (2005) 91–94.
[47] A. Bag, K.K. Ray, E.S. Dwarakadasa, Metall. Mater. Trans. A 30 (1999) 1193–1202.
[48] H. Mathy, J. Gouzou, T. Gréday, in: R.A. Kot, B.L. Bramfitt (Eds.), Fundamentals of Dual-phase Steels, The Metallurgical Society of AIME, New York, 1981, pp. 413–426.
[49] M. Calcagnotto, D. Ponge, E. Demir, D. Raabe, Mater. Sci. Eng. A 527 (2010) 2738–2746.
[50] A.K. Sachdev, Acta Metall. 31 (1983) 2037–2042.
[51] S. Sangal, N.C. Goel, K. Tangri, Metall. Trans. A 16 (1985) 2023–2029.
[52] M.H. Saleh, R. Priestner, J. Mater. Process. Technol. 113 (2001) 587–593.
[53] S. Takaki, K. Fukunaga, J. Syarif, T. Tsuchiyama, Mater. Trans. 45 (2004) 2245–2251.
[54] J. Becker, E. Hornbogen, P. Stratmann, Z. Metallkd. 71 (1980) 27–31.
[55] A.R. Marder, Metall. Trans. A 13 (1982) 85–92.
[56] T. Kunio, M. Shimizu, K. Yamada, H. Suzuki, Eng. Fract. Mech. 7 (1975) 411–417.
[57] P. Uggowitzer, H.P. Stüwe, Mater. Sci. Eng. 55 (1982) 181–189.
[58] X.J. He, N. Terao, A. Berghezan, Met. Sci. 18 (1984) 367–373.
[59] X.L. Cai, J. Feng, W.S. Owen, Metall. Trans. A 16 (1985) 1405–1415.
[60] N.J. Kim, G. Thomas, Metall. Trans. A 12 (1981) 483–489.
[61] C.M. Yen, C.A. Stickels, Metall. Trans. 1 (1970) 3037–3047.
[62] B.L. Bramfitt, A.R. Marder, Metall. Trans. A 8 (1977) 1263–1273.
[63] D.W. Kum, T. Oyama, J. Wadsworth, O.D. Sherby, J. Mech. Phys. Solids 31 (1983) 173–186.

ELSEVIER

Materials Science and Engineering A 441 (2006) 1–17

MATERIALS SCIENCE & ENGINEERING A

www.elsevier.com/locate/msea

Review

Overview of processing, microstructure and mechanical properties of ultrafine grained bcc steels

R. Song [a,*], D. Ponge [b], D. Raabe [b,**], J.G. Speer [a], D.K. Matlock [a]

[a] *Department of Metallurgical and Materials Engineering, Colorado School of Mines, Golden, CO 80401, USA*
[b] *Max-Planck-Institut für Eisenforschung, Max-Planck-Str. 1, 40237 Düsseldorf, Germany*

Received 18 July 2006; received in revised form 3 August 2006; accepted 25 August 2006

Abstract

Ultrafine grained steels with grain sizes below about 1 μm offer the prospect of high strength and high toughness with traditional steel compositions. These materials are currently the subject of extensive research efforts worldwide. Ultrafine grained steels can be produced either by advanced thermomechanical processes or by severe plastic deformation strategies. Both approaches are suited to produce submicron grain structures with attractive mechanical properties. This overview describes the various techniques to fabricate ultrafine grained bcc steels, the corresponding microstructures, and the resulting spectrum of mechanical properties.

Keywords: Ultrafine grained steels; Microstructure; Thermomechanical processing; Severe plastic deformation; Mechanical properties

Contents

* Corresponding author. Tel.: +1 303 273 3624; fax: +1 303 273 3016.
** Corresponding author. Tel.: +49 211 6792 340.
E-mail addresses: rsong@mines.edu (R. Song), d.raabe@mpie.de (D. Raabe).

0921-5093/$ – see front matter © 2006 Elsevier B.V. All rights reserved.
doi:10.1016/j.msea.2006.08.095

1. Introduction

Among the different strengthening mechanisms, grain refinement is the only method to improve both strength and toughness simultaneously. Therefore, ultrafine grained steels with relatively simple chemical compositions, strengthened primarily by grain refinement, have great potential for replacing some conventional low alloyed high strength steels. The main benefits behind such an approach are to avoid additional alloying elements; to avoid additional heat treatments like soft annealing, quenching and tempering; and to improve weldability owing to lower required carbon contents and other alloying elements when compared with other high strength steels. A further high potential domain for such ultrafine grained steel is the possibility for high strain rate superplasticity at medium and elevated temperatures [1]. In general, the term ultrafine grain is used here in the context of average grain sizes between 1 and 2 μm in diameter; submicron refers to grain sizes between 100 and 1000 nm; while nanostructured refers to grain sizes below about 100 nm.

The purpose of this overview is to provide a detailed introduction to the processing technologies, to the resulting microstructures, and to the mechanical properties associated with ultrafine grained body centered cubic (bcc) steels.

2. Methods of producing ultrafine grained steels

2.1. Introduction

Currently, laboratory techniques to produce ultrafine grained bcc steels utilize two approaches: severe plastic deformation techniques or advanced thermomechanical processing, which essentially involves modification to conventional large scale steel rolling processes. Compared to severe plastic deformation techniques, advanced thermomechanical methods are large-scale industrial processes and can be somewhat more readily optimized to operate in temperature regimes where they beneficially exploit phase transformation and controlled cooling.

2.2. Severe plastic deformation

2.2.1. Severe plastic deformation techniques for steels

Severe plastic deformation (SPD) techniques [2–4] impose large accumulated plastic strains at room or elevated temperatures, e.g. mainly in the temperature regime of warm deformation. These techniques can be used to produce ultrafine grained steels with an average grain size below 1 μm [5–19]. Typical SPD techniques include equal-channel angular pressing (ECAP) [5–11], accumulative roll bonding (ARB) [12–14], bi-directional compression [15], and high-pressure torsion (HPT) [16–19].

2.2.2. Equal-channel angular pressing

Equal-channel angular pressing imposes large plastic strains on massive billets via a pure shear strain state. The approach was developed by Segal et al. in the early 1980s [20]. Its goal was to introduce intense plastic strain into materials without changing the cross-sectional area of the deformed billets. Owing to this characteristic, repeated deformation is possible. At the beginning of the 1990s this method was further developed and applied as a severe plastic deformation method for the processing

of microstructures with submicron grain sizes [21]. The equal-channel angular pressing method was mainly applied for non-ferrous alloys (e.g. Al and Mg alloys) and some low carbon steels. The finest ferrite grain size obtained by use of this method is reportedly about 0.2 μm [7,22].

2.2.3. Accumulative roll bonding

Accumulative roll bonding essentially involves repeated application of conventional rolling. This approach has been suggested to possess the potential for mass production [12–14,23–25]. While rolling is an attractive deformation process for continuous production of bulk sheets, the total reduction in thickness, i.e. the accumulated strain, which can be achieved by this method, is limited because of the decrease in the strip thickness with increasing rolling reduction. In order to obtain bulk material, rolled sheets are stacked and then bonded together during rolling. Hence, the process involves simultaneous bonding and deformation. In the accumulative roll bonding method, the rolled material is cut, stacked to the initial thickness and rolled again. Owing to this approach, multiple repetitions are possible to achieve huge strains. A natural limit of this approach lies in the increase in strength and the gradually reduced surface quality of the roll-bonded sheets.

2.2.4. High pressure torsion

High-pressure torsion (HPT) imposes a pressure of up to several GPa for the fabrication of disk shaped samples with a diameter from 10 to 20 mm and a thickness of 0.2–0.5 mm [19]. A disk shaped specimen, which is usually first provided as a powder sample, is compressed in an almost closed die. During loading, the contact platens rotate in opposite directions in order to impose a shear strain. The through-thickness distribution of shear strain depends on the contact friction, a function of the roughness of the contact plates and the lubrication state. The torsion straining achieves a substantial degree of substructure refinement and controls the evolution of large crystallographic misorientations among adjacent grains. The HPT technique also has the advantage of being able to refine the grain size during powder consolidation, making it possible to produce bulk nanomaterials from micrometer-sized metallic powders.

2.2.5. Bi-directional large strain deformation

Bi-directional compression can be used to introduce large plastic strains in steels. It combines severe plastic deformation (large strain) and thermomechanical processing (phase transformation and controlled cooling can be exploited). Compression is realized by alternate forging in two perpendicular directions. Elongation in the third direction is usually not restricted.

2.3. Advanced thermomechanical processes

2.3.1. Introduction

In contrast to severe plastic deformation approaches in which large strain is the main factor, advanced thermomechanical processes pursue alternative strategies to produce ultrafine ferrite grains. For instance, these processes exploit dynamic recrystallization of austenite during hot deformation with subsequent $\gamma \rightarrow \alpha$ (austenite to ferrite) transformation [26]; strain-induced ferrite transformation (i.e. transformation during rather than after deformation) [27–32]; hot rolling in the intercritical region (i.e. in the austenite/ferrite two-phase region) [33]; warm rolling in the ferrite region [34] involving either dynamic recrystallization or pronounced recovery of the ferrite during warm deformation [35–45]; or cold rolling and annealing of a martensitic starting microstructure [46–51].

2.3.2. Recrystallization of austenite during hot deformation

An important mechanism that is widely used for grain refinement in steels is dynamic recrystallization during hot deformation [26]. This technique has been used to produce ferrite grain sizes as fine as 2–5 μm via recrystallization-controlled rolling or by conventional rolling followed by accelerated cooling. In recrystallization-controlled rolling fine precipitates restrict austenite grain growth after deformation. Recrystallization-controlled rolling is often used in conjunction with accelerated cooling and microalloying in order to effectively refine the grain size. Accelerated cooling is used to increase the cooling rate through the transformation zone in order to decrease the transformation temperature. In principle, a lower transformation temperature results in a higher ferrite nucleation rate due to a higher undercooling, and a decreased growth rate. Conventional controlled rolling has been implemented in many commercial operations through the addition of elements such as Nb, which increases the recrystallization temperature to over 1173 K, such that deformation in the last passes are applied below the recrystallization temperature. This increases the density of sites for ferrite nucleation.

2.3.3. Strain-induced ferrite transformation

A simple rolling procedure which entails strain-induced phase transformation from austenite to ferrite has been found to provide significant grain refinement in the sheet surface. In this approach, steel strips are reheated to obtain austenite microstructure and subsequently rolled in a single pass (30% reduction) just above A_{r3} (austenite to ferrite transformation temperature) but below A_{e3} (equilibrium austenite to ferrite transformation temperature) [27,52–56]. The three critical factors promoting the formation of ultrafine ferrite grains during a strain-induced transformation are a high shear strain, a high cooling rate as a result of rapid heat transfer to the colder rolls during the roll pass, and an appropriate deformation temperature (between A_{r3} and A_{e3}).

Hodgson et al. [27] applied strain-induced transformation to a plain carbon steel strip (0.06C–0.59Mn, wt.%) with an original thickness of about 2 mm, reduced to about 1.4 mm after a single pass at roll exit temperatures between 953 and 983 K. Equiaxed ultrafine ferrite grains of about 1 μm in the subsurface region were obtained, but the microstructure of the rolled strip was inhomogeneous through the thickness. The microstructure consisted of ultrafine ferrite grains in the surface layers, which penetrated to between one-quarter and one-third of the thickness with coarser ferrite (about 5–10 μm) and pearlite in the core of the strip.

2.3.4. Intercritical hot rolling

Ultrafine ferrite grains in plain C–Mn steels have also been obtained through hot rolling in the intercritical region (i.e. in the austenite plus ferrite two-phase region) by Yada et al. [57]. They attributed grain refinement to both dynamic transformation of austenite into ferrite and the dynamic recrystallization of the ferrite phase. Nucleation of ferrite at austenite grain boundaries during the dynamic transformation was considered to play a major role in the formation of ultrafine ferrite grains while dynamic recrystallization of ferrite was assumed to be of minor relevance.

2.3.5. Dynamic recrystallization of ferrite during warm deformation

Warm deformation in the ferrite regime may further refine steel microstructures that were previously refined during transformation. It has been considered that recovery is the main softening process during warm deformation of ferrite and that dynamic recrystallization does not occur [35]. This behavior is attributed to the fact that bcc ferrite has a high stacking fault energy which results in rapid recovery and insufficient accumulation of stored deformation energy to promote dynamic recrystallization. However, the occurrence of dynamic recrystallization of ferrite has been reported by several researchers [35–37,58]. The recent study of Murty et al. [36] confirmed the occurrence of dynamic recrystallization of ferrite in an ultra-low carbon steel processed by warm deformation at a strain rate of 0.01 s^{-1} (low Zener–Hollomon parameter). Since warm deformed ferrite usually contains pronounced subgrain structures that are sometimes difficult to distinguish from recrystallized grains in standard light optical micrographs, the authors confirmed the occurrence of dynamic recrystallization in ferrite by use of the electron backscattered diffraction (EBSD) technique to characterize the crystallographic relationships across grain boundaries. Most of the equiaxed ferrite grains were surrounded by high-angle grain boundaries (HAGBs) (with grain boundary misorientations $\geq 15^\circ$) rather than by low-angle grain boundaries (with grain boundary misorientations $<15^\circ$).

In another case, warm-rolling of interstitial free (IF) steel in the ferrite region was found by Najafi-Zadeh et al. [34] to produce ultrafine ferrite with grain size of 1.3 μm. Dynamic recrystallization of ferrite was considered to play a major role in the formation of ultrafine ferrite. A key barrier to the occurrence of dynamic recrystallization of ferrite is suggested to involve the presence of interstitial elements such as C and N. Removing interstitial elements from the matrix reduces the possibility of strain-induced precipitation, which inhibits dynamic recrystallization and increases the likelihood of dynamic recrystallization of ferrite [34].

2.3.6. Pronounced recovery of ferrite during warm deformation and annealing

Recently, Song et al. [39–45] have reported the production of ultrafine ferrite through pronounced recovery following warm deformation and annealing. Compared with the earlier studies on low carbon ultrafine grained bcc steels, Song et al. [39–45] investigated medium carbon steels in an effort to increase the work hardening rate of ultrafine grained steels, since high work hardening rates are associated with high ductility. In their studies, steels with ultrafine ferrite grains and homogeneously distributed cementite particles were produced by large strain warm deformation ($\varepsilon = 1.6$) at 823 K and subsequent annealing (Fig. 1). The ultrafine microstructures obtained were stable against grain and cementite coarsening even during a 2 h annealing treatment at 823 K. Pronounced recovery instead of primary recrystallization was required to obtain a large fraction of HAGBs. It was concluded in [39] that the prevalence of primary recrystallization, instead of recovery, is not generally beneficial in warm rolling. Primary recrystallization reduces significantly the dislocation density and removes the substructure, which is important for the gradual formation of subgrains that eventually become ultrafine grains surrounded by HAGBs.

2.3.7. Cold rolling and annealing of martensitic steel

Another route to fabricate ultrafine grained steel was developed by Tsuji et al. [49–51]. The process includes cold-rolling (50% reduction) of a martensite starting microstructure in a low carbon steel (0.13 wt.% C) and subsequent annealing at 773–873 K. The final microstructure was reported to consist of ultrafine ferrite grains and uniformly precipitated carbides. The formation of an ultrafine microstructure was attributed to the fine martensite starting microstructure, which augmented the effect of plastic deformation enhancing grain subdivision [49–51]. The high dislocation density as a result of cold rolling and the high concentration of solute carbon atoms in the martensite were also expected to facilitate grain subdivision by causing inhomogeneous deformation [49–51].

2.4. Summary of the two strategies of producing ultrafine grained steels

2.4.1. Differences

As mentioned above, ultrafine grained steels can be produced by two main methods. Table 1 gives a summary of the various process techniques described above and the ferrite grain sizes obtained for the different bcc steels. Among the SPD techniques the accumulated plastic strains (true strains) required to obtain submicron-sized grains are of the order of 3–4 using ECAP and of the order of 5–6 using the ARB process. For the SPD methods, a well-designed strain path is more important and also more feasible than a precisely controlled temperature path. The small-scale complexity and the "batch" nature of these methods suggest that they would require considerable ingenuity and investment for application to high volume steel production.

The advanced thermomechanical processing routes employ a relatively low accumulated strain in the range of about 1.0–3.6 to produce ultrafine grained steels (except for the strain-induced ferrite transformation technique which typically requires even less strain). The advanced thermomechanical processing methods are less effective with respect to grain refinement, but more adaptable to large sample sizes when compared with the

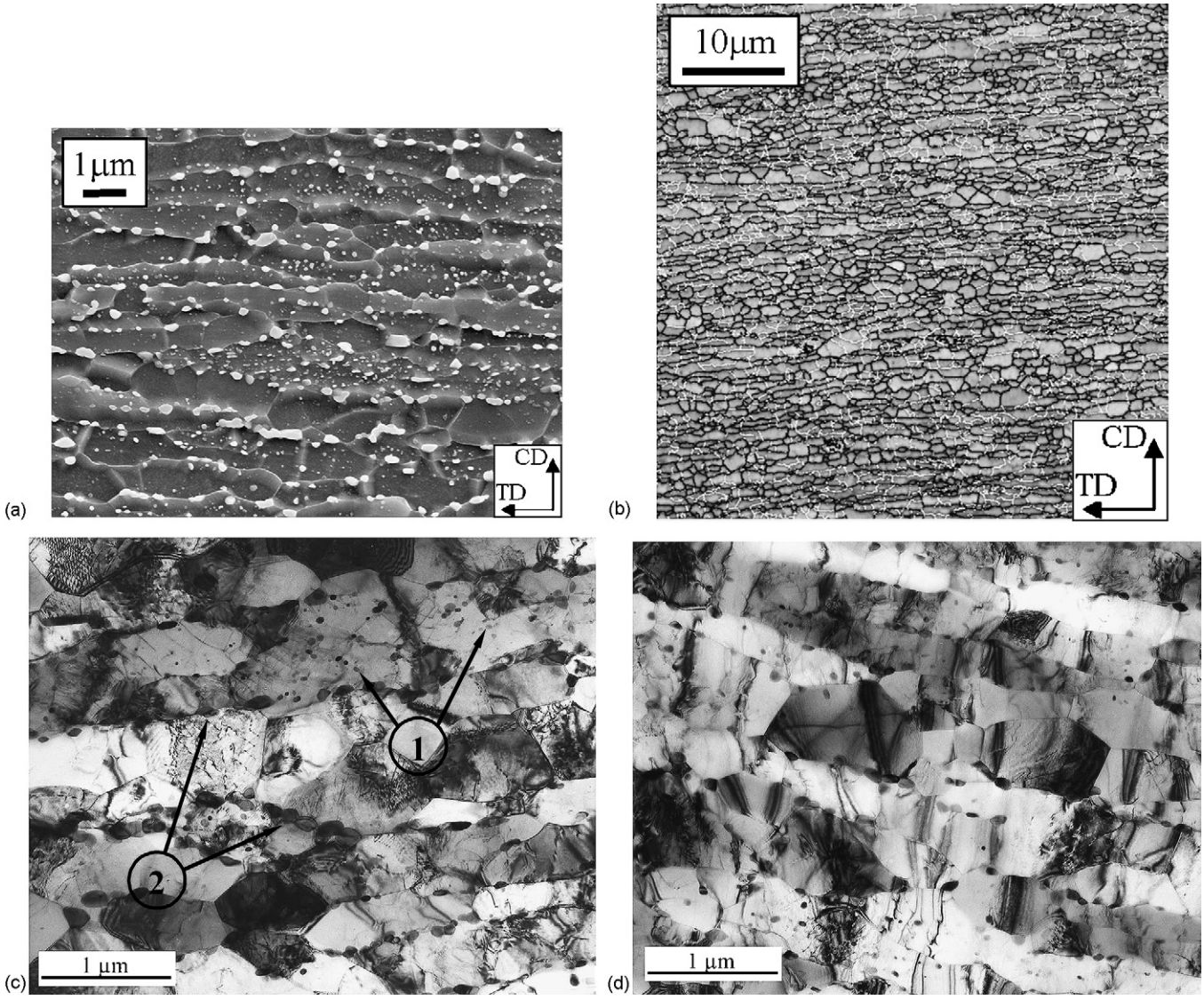

Fig. 1. SEM image (a) and EBSD map (b) after large-strain deformation ($\varepsilon = 1.6$) and subsequent 2 h annealing at 823 K obtained for a plain C–Mn steel (CD, compression direction; TD, transition direction). The black lines indicate grain boundary misorientations between 15° and 63°. White lines indicate grain boundary misorientations between 2° and 15°. (c) TEM micrograph of an ultrafine grained steels after large strain warm deformation ($\varepsilon = 1.6$, and 2 h at 823 K) with 0.74 mass% Mn. Arrows "1" point at very fine cementite particles inside the ferrite grains; arrows "2" point at coarse cementite particles at the ferrite grain boundaries. (d) Corrresponding TEM micrograph for a steel with 1.52 mass% Mn. Details of the compositions and of the processing are given in [39–45].

SPD methods. An important issue in this context, however, is that in the case of large sample sizes the strain and cooling paths have to be carefully controlled since they are key parameters that govern the final grain size within relatively small process windows.

A further difference between these two approaches is that the advanced thermomechanical methods are continuous processes and can be well optimized when they work in a temperature regime where they exploit phase transformation and controlled cooling. The most significant feature of transformation refinement is the possibility of optimizing the conditions to produce a maximum number of new grains that usually nucleate at grain boundaries. In this context, the high temperature phase can be pretreated to increase the grain boundary area (refined or pancaked grains) and to introduce a dense dislocation substructure by large strains at the lowest possible temperature to avoid static primary recrystallization. Ultimately, the transformed product can be subjected to warm or cold deformation, possibly in conjunction with precipitation of carbides in steel. A concern in this context is not only the desired increase in strength but also the possible drop in toughness and ductility [61].

2.4.2. Similarities

Ultrafine grained ferrite microstructures are of great interest for low alloyed structural steels as reflected by the steels reported in Table 1, regardless of severe plastic deformation or advanced thermomechanical processes. Structural steels with improved mechanical properties may facilitate light-weight construction design (buildings, bridges, large structures). Both the SPD and advanced thermomechanical processes may encounter difficulties in being scaled up to large commercial scales and

Table 1
Summary of different techniques reported to produce ultrafine grains in bcc steels

Techniques	Steels	Steels composition (wt.%)	Ferrite grain size achieved (μm)	Log. strain imposed [1]	Deformation temperature (K)	Heat treatment after deformation	Reference
ECAP	Plain low carbon steel	0.08C–0.42Mn–0.18Si	0.2	3.0	293	AC	[7]
	Plain low carbon steel	0.15C–1.1Mn–0.25Si	0.3 in thickness	4.0	623	AC	[22]
	Ti–V carbon steel	0.1C–1.59Mn–0.29Si–0.02Ti–0.05V	∼0.3 in thickness	1.0	573	AC	[59]
	Ferrite–martensite dual phase steel	0.15C–1.06 Mn–0.25Si	0.8	4.0	773	1003 K × 10 min WQ	[46]
ARB	Ti added IF steel	0.003C–0.15Mn–<0.01Si–0.049Ti	0.4	5.6	773	WC	[14]
HPT	Plain low carbon steel	∼0.7C–∼1.0Mn–∼0.3Si	0.01	Shear strain 300, log. strain 0.45	293	AC	[16,18]
DRX* during hot deformation	Microalloyed steel	0.11C–1.45Mn–0.34Si–0.068Nb	2–5	Final rolling 2.2–3.6	1153–1033	AC	[26]
Strain-induced ferrite transformation	Plain low carbon steel	0.06C–0.59Mn	1.0 (strip surface)	0.36	1053	AC	[27]
Deformation in the intercritical region	Plain low carbon steel	0.17C–1.32Mn–0.44Si–0.15Nb	2.1	2.3	973	WQ	[60]
Warm rolling in the ferrite region	Ti added IF steel	0.003C–0.15Mn–0.022Si–0.065Ti	1–3	Final rolling ∼0.55 × 5	Below A^*_{r1}	WQ	[34]
DRX* of ferrite during warm deformation	Ultra-low carbon steel	0.0016C–0.1Si–0.3Mn	–	4.0	723–823 (lower than A^*_{c1})	WQ	[36]
Pronounced recovery of ferrite during warm deformation and annealing	Plain medium carbon steel	0.22C–0.21Si–0.74Mn	1.3	1.6 at strain rate of 0.01 s^{-1}	823	823 K × 120 min	[39]
Cold deformation and annealing of martensitic steel	Martensitic steel	0.13C–0.37Mn–0.01Si	0.18	0.8	293	773 K × 30 min	[49]

Abbreviations: DRX*, dynamic recrystallization; A^*_{r1}, austenite to pearlite transformation temperature during cooling; A^*_{c1}, pearlite to austenite transformation temperature during heating; ECAP, equal channel angular pressing; ARB, accumulative roll bonding; HPT, high pressure torsion; AC, air cooling; WC, water cooling; WQ, water quench.

mass production, but both approaches offer insight into the microstructure and properties that can be achieved by such approaches.

3. Microstructure characterization of ultrafine grained steels

Ultrafine grained ferrite microstructures can be quite different due to the various methods and heat treatments applied as well as the differences in the chemical compositions and the initial microstructures. In this section, characterization of ultrafine grained bcc steel microstructures will be discussed in detail.

3.1. Microstructure of ultrafine grained steels produced by SPD techniques

3.1.1. Equal-channel angular pressing

The microstructures of low carbon steels (0.15 wt.% C) after different passes of equal-channel angular pressing have been investigated by Fukuda et al. and Shin et al. [7,22]. After one ECAP pass ($T = 623$ K, $\varepsilon = 1.0$), the microstructure consisted of extended parallel grain boundaries with mainly low-angle misorientation angle between adjacent crystals [7,22]. The width of the parallel bands was approximately 0.3 μm and the dislocation density inside the subgrains was relatively low. After two ECAP passes ($\varepsilon = 2.0$), the average misorientation between subgrains increased, the ferrite grain shape was less elongated and the average grain size was approximate 0.5 μm. Equiaxed ferrite grains with an average grain size of 0.2–0.3 μm were achieved after four ($\varepsilon = 4.0$) ECAP passes. The fraction of high-angle grain boundaries increased gradually with further deformation passes. Consequently, the final microstructure of samples, which had undergone a sufficient number of ECAP passes consisted mainly of high-angle grain boundaries [7].

For a submicron grained low carbon steel processed by ECAP ($\varepsilon = 4.0$) at 623 K, less grain growth was observed at relatively low annealing temperatures (693–783 K for 1 h) [62]. Both the dislocation structure and the well-defined grain boundaries at elevated temperatures observed in the microstructure demonstrated the occurrence of recovery during annealing in this temperature region. A further increase in the annealing temperature ($\geq$813 K) led to partial primary recrystallization. The addition of Ti and V to low carbon steels did not lead to significant refinement of ferrite after ECAP processing [59]. Nevertheless, very fine Ti–V nitrides were reported to be beneficial for improving work hardening of the steel by accumulation of dislocations around the precipitates.

It is well known that many ultrafine grained single phase steels exhibit relatively low tensile ductility at room temperature. This can be partially attributed to the low work hardening rate, which is commonly observed for ultrafine grained single phase material. One approach to improve the work hardening of such steels is to create microstructures, which contain a second phase. In this context, ultrafine grained dual phase steels seem to be attractive for obtaining both higher strength and improved ductility. Ultrafine grained ferrite–martensite dual phase steels (0.15% C) have been fabricated by Park et al. [48,63] using ECAP plus intercritical annealing in the ferrite/austenite two phase region (i.e. between the A_{c1} and A_{c3} temperatures) followed by quenching. The microstructure of the steel after the ECAP deformation ($T = 773$ K, $\varepsilon = 4.0$) consisted of a severely deformed pearlitic lamellar microstructure with reduced interlamellar spacing, ultrafine ferrite with an average grain size of 0.2–0.5 μm with high dislocation density, and spheroidized cementite particles. After intercritical annealing at 1003 K for 10 min and subsequent water quenching, the microstructure consisted of ultrafine ferrite grains, homogeneously distributed martensite islands, and incomplete martensite networks at the ferrite–ferrite grain boundaries. The martensite islands were transformed from the austenite, which replaced pearlite during the intercritical annealing treatment. The martensite network was reported to be associated with local segregation of Mn [48,63]. High dislocation densities were observed in the ferrite grains adjacent to the martensite. Most of these dislocations were assumed to result from accommodation of the phase transformation during quenching. The high dislocation density enhanced the work hardening behavior. In summary, grain refinement was significant after the first pass of ECAP. A further increase in the number of deformation passes had a diminishing effect on grain refinement but was beneficial for the formation of high-angle grain boundaries and the transition of the ferrite grain morphology from an elongated to more equiaxed shape. The ultrafine grained microstructure produced by ECAP was relatively stable against grain coarsening at certain temperatures. Recovery was the main softening mechanism at modest annealing temperatures.

3.1.2. Accumulative roll bonding

Compared with the ultrafine grained microstructure produced by the other SPD and conventional rolling techniques, different types of microstructures and crystallographic textures were observed for steels produced by the ARB method [23,64,65]. This difference can be attributed to the different strain distributions associated with the various approaches. It is well known that the surface regions of ferritic steel sheets processed by large strain rolling reveal a pronounced shear texture which is quite different than the texture observed in the through-thickness center regions of the same sheet [66–69]. In the ARB technique, the rolled sheet is cut and stacked between ensuing cycles, so that half of the surface, which had undergone the severe shear deformation in the prior rolling step ends up in the sheet center in the following ARB rolling step. These shear regions appear not only at the surface layers, but are also distributed through the sheet thickness after several ARB passes. Materials processed by ARB undergo a complicated mixed series of plane strain and shear deformation states. Thus, steels processed by the ARB method experience a complex distribution of microstructure and texture through their sheet thickness [23,64,65].

Tsuji et al. [23,64] investigated the microstructure and crystallographic texture of an ultra-low carbon (0.003% C) IF steel processed by the ARB process. Experiments were conducted by imposing a logarithmic strain of $\varepsilon = 0.8$ (50% reduction) at 773 K. This procedure was repeated up to seven cycles corresponding to a total strain of 5.6. The microstructure after one

cycle of the ARB process ($\varepsilon = 0.8$) showed a typical dislocation cell structure. The size and orientation of elongated cells varied through the sheet thickness. After two more cycles of the ARB process ($\varepsilon = 2.4$), elongated grains with high-angle misorientation were observed in addition to the dislocation cell structure. With further increases in strain ($\varepsilon \geq 3.2$) the resulting microstructure consisted mainly of elongated ultrafine ferrite grains, and an increased fraction of high-angle grain boundaries. After seven cycles of the ARB process ($\varepsilon = 5.6$) around 80% ultrafine ferrite grains were surrounded by high-angle grain boundaries, while some dislocations remained in the ferrite. The ultrafine grained microstructure was distributed relatively homogenously throughout the sheet thickness.

The ultrafine grained microstructure formed via the ARB process can be interpreted in terms of a process of repeated gradual recovery and grain subdivision. The extent of recovery is sufficient to result in high-angle grain boundaries after extensive ARB. The ARB method is more effective for achieving grain refinement than conventional routes at identical strains. The authors attributed this to the redundant shear strain throughout the thickness of specimens processed by the ARB, which facilitated grain subdivision and formation of an ultrafine grained microstructure [23,64,65].

3.1.3. High pressure torsion

The thickness reduction imposed on samples processed by HPT is negligible compared to the large shear strain imposed. The formation of nanostructures and the dissolution of pearlite lamella in a commercial pearlitic steel (~0.7% C) produced by HPT were reported by Ivanisenko et al. [16–18]. After a shear strain of 100 at room temperature the microstructure at the surface of a disk shaped sample consisted of a cell structure and partially dissolved cementite lamellae. Further increase in the shear strain to a level of 200 resulted in an inhomogeneous grain morphology. Elongated grains 100 nm in length and 15 nm in height were created during the process. The elongated grains were separated by dense dislocation walls. This morphology was very similar to the lamellar-type boundaries observed in samples processed by ECAP. The spacing of the cementite lamella decreased during straining. After a shear strain of 300, a homogeneous nanostructure with a grain size of 10 nm and total dissolution of cementite was obtained.

3.2. Microstructure of ultrafine grained steels produced by advanced thermomechanical processing

3.2.1. Transformation grain refinement

In low carbon microalloyed steels, ferrite grain sizes and precipitation states are important factors, which affect the strength–toughness relationship. The ferrite grain size is a function of the austenite grain size after austenite recrystallization, the amount of retained strain in the austenite before the start of transformation, and the cooling rate through the transformation regime [56].

Progressive refinement of the austenite can be achieved through dynamic and static recrystallization during large strain deformation (roughing) at temperatures above the recrystallization temperature. According to the work of Kaspar et al. [26], by strictly controlled hot deformation schedules, dynamic recrystallization of austenite is obtained at relatively low temperatures (less than 1143 K) by applying total finishing strains greater than 2.2 in a microalloyed steel (0.11C–0.34Si–1.45Mn–0.068Nb–0.08V, wt.%). The grain size of the dynamically recrystallized austenite was around 1–4 μm. Priestner and Ibraheem [56] reported that fine austenite with grain size of <5 μm could be obtained by reheating a cold-rolled tempered martensite (with finely dispersed cementite) in a Nb microalloyed steel (0.1C–0.31Si–1.42Mn–0.035Nb, wt.%) [56]. Average ferrite grain sizes of <1 μm in the surface layer of a 2–3 mm thick sheet have been achieved using accelerated cooling (e.g. ~8 K s^{-1}) after hot rolling of fine austenite to equivalent strains of 0.5–1.0 at 1123 K [56]. The ferrite grain size in the center of the plate was ~1.5 μm. Studies using EBSD and misorientation imaging showed that most of the grain boundaries revealed misorientations above 15° [56].

Contrary to the accepted view that fine austenite grain sizes lead to fine ferrite grains, Hurley and Hodgson [54] showed that a very fine ferrite grain size could be produced from a steel having a large prior austenite grain size. Intragranular nucleation of ferrite may be an important factor contributing to the additional grain refinement observed when a dynamic strain-induced transformation occurs, and is encouraged by large austenite grain sizes and accelerated cooling, both of which suppress the formation of grain boundary proeutectoid ferrite [54]. The strain-induced transformation rolling procedure is attractive in terms of its relative simplicity and ability to refine ferrite grain sizes in plain carbon steels [70–75]. The technique involves rolling steel strip containing a large austenite grain size (>100 μm), at a temperature just above the A_{r3} but below the A_{e3}. A single rolling pass induces very efficient grain refinement, producing equiaxed and fine polygonal ferrite grains on the scale of less than 2 μm in the surface regions (~250 μm deep) of the strip [53]. The rolling reduction required to generate this ultrafine ferrite is approximately 35–40%. It appears that a roll chilling effect in conjunction with large shear strains resulting from roll friction explain the phenomenon. These steps facilitate a high density of intergranularly nucleated ferrite grains during hot rolling of austenite.

Using large strain ($\varepsilon = 2.3$) hot rolling in the austenite/ferrite two-phase region, followed by fast cooling, Nanba et al. [60] produced ultrafine ferrite with a grain size of 1.2 μm in a low alloyed steel (0.17C–0.44Si–1.32Mn–0.015Nb, wt.%). In contrast, Bodin et al. [76] reported that a bimodal grain size distribution was obtained by hot rolling in the two-phase region. Conceivably, the large ferrite grains (>6 μm in diameter) observed in the bimodal size distribution can be attributed to growth of the transformed ferrite into the deformed ferrite. The transformed ferrite resulted from austenite that was deformed during intercritical rolling, while the deformed ferrite was transformed from austenite before intercritical rolling. The small ferrite grains (1–2 μm in diameter) were attributed to extended recovery of the deformed ferrite [76]. In order to obtain homogeneous ultrafine ferrite by intercritical rolling, it seems to be very important to balance the dynamic transformation of austenite into ferrite and the dynamic

recovery and recrystallization of ferrite through careful control of the processing parameters including chemical composition, deformation schedules (strain/strain rate/temperature), and cooling rate. For example, low carbon steels have a relatively small intercritical regime and recrystallization of deformed ferrite can proceed rapidly but is terminated upon rapid cooling.

3.2.2. Grain refinement by recovery/recrystallization in warm working

Since hot working involves a high cost of thermal energy, there has been a trend to develop processes at lower temperatures [77]. Deformation at lower temperature, also referred to as warm working, can help to produce steels close to their final shape and reduce or eliminate cold work involving higher roll forces or die-pressures. Grain refinement during warm or ferritic rolling can be realized by recovery/recrystallization. In this context, dynamic recrystallization of ferrite under conditions of temperature and strain rate that correspond to a large Zener–Hollomon parameter, i.e. at low temperatures and high strain rates, is more beneficial to obtain good microstructure homogeneity.

In contrast to the accepted view that grain refinement is achieved by recrystallization, Song et al. [40,44] have recently proposed that pronounced or extended recovery is more effective for the formation of ultrafine microstructure. In their studies, the prevalence of primary recrystallization instead of recovery was not generally beneficial since it significantly reduced the dislocation density and removed the substructure that was important for the gradual formation of subgrains and of ultrafine grains surrounded by HAGBs.

3.2.3. Grain refinement by cold deformation and annealing

It is known that the grain size obtained by static recrystallization is a function of the prior strain and the prior grain size [56]. Cold rolling and annealing of an initial martensite microstructure have drawn some attention recently to produce multiphase ultrafine grained steels [49–51]. The initial fine martensite is beneficial for grain subdivision during cold rolling due to the high dislocation density and substantial amount of solute carbon atoms in martensite. Nearly equiaxed ferrite grains and a homogeneous distribution of carbides were found after annealing. A multiphase ultrafine grained steel, consisting of ultrafine ferrite, dispersed cementite and tempered martensite, showed a good combination of strength and ductility.

3.3. Summary: production of ultrafine grained microstructures

In order to more quantitatively evaluate the microstructure of ultrafine grained steels, it has become customary to report not only the average cell or grain sizes and the corresponding grain size distributions, but also the fraction of high-angle grain boundaries obtained from the various processing strategies. The submicron structure produced by SPD is typically more elongated due to the intense deformation involved. Around 40% of the grain boundaries are of the low-angle dislocation boundary type (misorientations $< 15^\circ$), which is less beneficial for the overall mechanical response. These low-angle grain boundaries often appear in TEM as dense dislocation walls, rather than as sharp boundaries, which could migrate more easily. It is difficult for the cells to be transformed into discrete grains surrounded by high-angle grain boundaries without an annealing treatment. The conversion to high-angle misorientation walls usually occurs at a temperature of 0.3–0.4T_M (melting temperature), which is much below the traditional static recrystallization temperature of 0.5T_M [61].

Hot deformation develops larger more polygonized cells or subgrains during dynamic recovery compared to the submicron structure produced by SPD. Increasing strain leads to the occurrence of dynamic recrystallization of austenite. Hot working at intermediate temperature often provides a mixed microstructure of different grain sizes. Warm and cold working hastens grain subdivision due to a relatively higher dislocation density introduced/accumulated compared to hot deformation. Subsequent annealing is beneficial for formation of high-angle grain boundaries by pronounced recovery/recrystallization processes.

The effects of alloying are largely similar in the different types of processing. Solid solution additions usually increase the degree of strain hardening in both cold and hot working and may slow dynamic recovery in bcc steels. Large quantities of second phase constituents, such as fine cementite particles, are beneficial for the formation of a fine ferritic grain structure. They inhibit grain boundary migration due to Zener pinning. This effect stabilizes the ultrafine grains against grain coarsening, and is also thought to inhibit primary recrystallization. The presence of such fine particles results in an increase of the effective recrystallization temperature, widening the temperature windows for corresponding warm rolling and annealing treatments [39].

4. Tensile properties

4.1. Strength

4.1.1. Effect of grain size on strength

The yield stress for bcc steels processed by different methods is plotted in Fig. 2 as a function of the inverse square root of the grain size for grain sizes ranging from 45 to 0.2 μm. The ultrafine microstructures (grain size less than 2 μm) were produced by various techniques: the open symbols display the results from the SPD methods; the full symbols in gray represent the results from the advanced thermomechanical process routes (ATP); the full symbols in black show the results from the conventional route (Conv). For each class of steel, the yield stress follows the Hall–Petch relation for a given steel, $\sigma_y = \sigma_i + k_y d^{-1/2}$, where σ_y is the yield stress, σ_i the friction stress, k_y the grain boundary resistance and d is the grain size in μm.

The lower yield strength of the 0.13C–0.67Mn–0.14Si (wt.%) steel sheet produced by cold rolling and annealing [82] is shown by the solid diamond in Fig. 2 where the grain size varied from 1.6 to 30 μm. The friction stress σ_i is about 100 MPa and the grain boundary resistance k_y is 551 MPa $\mu m^{1/2}$ [82], according to the work of Morrison in 1966.

ECAP (at 623 K) followed by annealing at temperatures between 373 and 873 K produced steels with grain sizes rang-

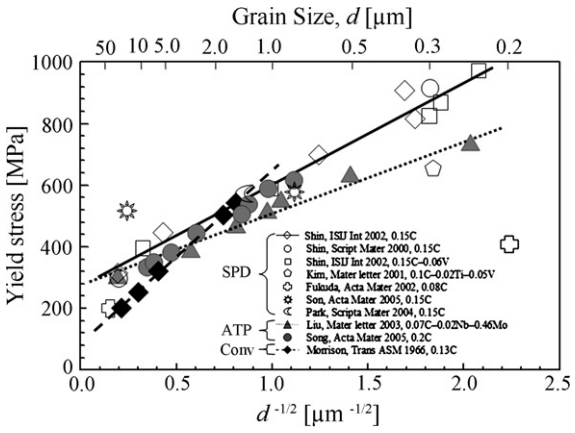

Fig. 2. Hall–Petch relationship in ultrafine grained bcc steels [7,46,48,59,78–82]. The open symbols display the results from the SPD methods; the full symbols in gray represent the results from the advanced thermomechanical process routes (ATP); the full symbols in black show the results from the conventional route (Conv). The straight lines show the Hall–Petch relation for different steels.

ing from about 0.23 to 10 μm in a low carbon (0.15C–1.1Mn –0.25Si, wt.%) and a low alloy steel (0.15C–1.1Mn–0.25Si–0.06V, wt.%) [78]. The k_y value in Fig. 2 (slope of bold line) is smaller in the steel processed by ECAP compared with the results of Morrison (dashed bold line). The yield stress for a grain size of 30 μm before ECAP is above the value predicted by Morrison, while the yield stress after ECAP is below the line. This phenomenon also reappears in other studies from both SPD and advanced thermomechanical processes [7,46,48,59,79–81]. That is, while the Hall–Petch relationship in steels may extend to the submicron range, the parameter k_y may decrease. The reason for this behavior will be discussed in Section 4.1.3.

For steels with submicron grain sizes produced by ECAP, the yield stress for steels with a carbon content less than 0.1 wt.% [7,59] is notably smaller than for the steels with 0.15 wt.% carbon [78] for a given grain size. The reason for this behavior is not fully understood, but could result from differences in grain size measurement.

The data for samples with a dual phase microstructure (displayed by the sun symbol in Fig. 2) [46] do not follow the line predicted by the Hall–Petch relationship as mentioned above. It seems that a smaller increment in stress is achieved in the dual phase steel when the ferrite grain size is refined from 19.4 to 0.8 μm. It is not clear whether this is related to some variation in the amount and morphology of the second phase after grain refinement.

4.1.2. Summary of Hall–Petch analysis for bcc steels

It should be stressed that in early investigations by Morrison [82], as shown in Fig. 2, the different grain sizes were produced by cold rolling and subsequent annealing at different temperatures. This offered the advantage to alter only one parameter—the grain size. In the investigation by Song et al. (where the initial motivation was not to measure the value of k_y and σ_i in the Hall–Petch equation), the coarse microstructure consisted of conventional ferrite and pearlite. When refined into the ultrafine microstructure, however, it comprised ferrite and fine spheroidized cementite. A smaller k_y value was found by Shin et al. [79], which might also be attributed to the change in overall microstructure (along with grain size) in their study. By use of the ECAP technique, the initial coarse grained ferrite–pearlite microstructure was severely deformed. After four deformation passes, a microstructure with finer ferrite and a partially spheroidized pearlite was obtained. Thus, the smaller k_y value in some studies on ultrafine ferrite might be the result of a reduction in the yield strength by replacing harder pearlite with softer ferrite and spheroidized cementite in the ultrafine microstructure. The presence of low misorientations between some grains in the ultrafine ferrite may also contribute to the reduced k_y value in comparison to conventional "coarse" ferrite with high misorientations.

It should be mentioned that most of the submicron microstructures measured for the SPD technique consist of large quantities of low-angle grain boundaries, and grain dimensions measured refer to the thickness of stretched microbands, which is not the same as average grain diameter. Further consideration of grain morphologies and appropriate characterization methods may be worthwhile to define the Hall–Petch relationship more accurately.

4.1.3. Comments on the effect of ultra grain refinement on the Hall–Petch k_y value

A series of early experimental investigations using Armco iron and nickel [83,84] over a broad range of grain size showed that the Hall–Petch relationship was an approximation applicable only over a limited range of grain sizes. The value of k_y seems to decrease for very small grain sizes. This deviation of the Hall–Petch relationship has been noted since the late 1950s and early 1960s [85–88]. Efforts have been made to develop an understanding of this behavior.

For polycrystalline materials, there exist three main theories for the Hall–Petch equation: the pile-up models [86,89–91], those based on work hardening [88,92,93] and the grain boundary source theories [94,95]. Pande et al. [96] demonstrated that the decrease of k_y at small grain sizes can be explained within the framework of the traditional dislocation pile-up model. The solution of the pile-up problem for small numbers of dislocations ($n < 20$) differs considerably from the usual solution [97] valid for larger n. With smaller grain sizes the $\sigma_y(d^{-1/2})$ relationship becomes a staircase function that reaches a plateau equal to $\sigma_y^{max} = M\tau_c$ at $n = 1$, where M is the Taylor factor and τ_c is the critical shear stress required for dislocation motion.

Fig. 3 shows a comparison of calculated exact and approximate n values together with the Hall–Petch prediction. It can be observed from Fig. 3 that the linear Hall–Petch relation is valid for this model when $n > 20$. If the length of one pile-up is assumed to be equal to half of the grain diameter, L, when n is equal to 20, the grain size/diameter is about 0.79 μm. This means based on the prediction in Fig. 3 a smaller k_y value results when the grain size is less than 0.79 μm. According to the results from SPD as displayed in Fig. 2, k_y maintains the same value when grain size is varies from 10 to 0.23 μm for a given steel. Therefore, it can be concluded that the smaller value of k_y in the present study is not fully explained by the model discussed above.

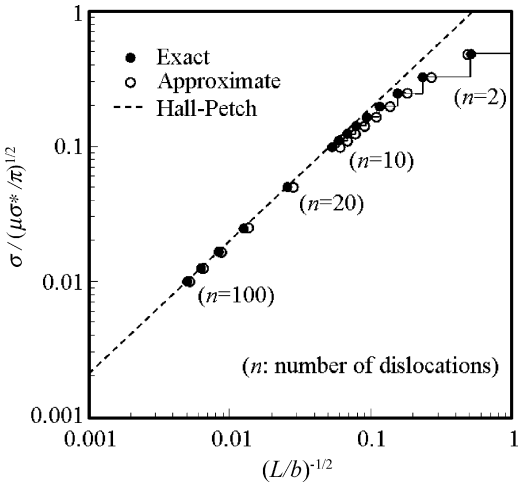

Fig. 3. Comparison of the exact and approximate n value (number of dislocations) together with the Hall–Petch prediction. After [96]. The exact value is calculated from the data of [98]. The approximate curves exhibit discrete steps and begin to level off as described by [99]. L is the length of the pile-up which is associated with the grain size, b the magnitude of Burger's vector, σ the applied stress and σ^* is the barrier stress which is assumed to be constant and independent of grain size; μ is the shear modulus.

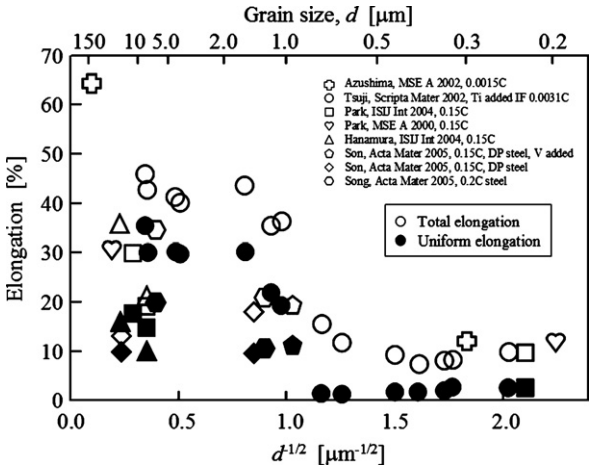

Fig. 4. Grain size dependence of ductility for bcc steels [24,44,46,102–105]. Open symbols represent total elongation while filled symbols display uniform elongation in tension.

Recent studies have reduced grain sizes to a few nanometers. Compared to conventional polycrystalline materials, nanocrystalline materials have often been found to exhibit a smaller or even a negative Hall–Petch slope. The critical grain size where deviation from Hall–Petch relation occurs is dependent on the specific material of interest [100].

4.2. Ductility

Several groups [27,40,52,101,102] have reported promising room temperature tensile strength properties for ultrafine grained steels. The steels are produced either by the severe plastic deformation or by the advanced thermomechanical processes. Many of the ultrafine grained steels investigated do not display a significant amount of work hardening, however. This shortcoming is reflected in high yield ratios (lower yield stress to ultimate tensile stress). For many ultrafine grained steels, the yield ratios are almost 1.0, compared to 0.7 for conventional steels with similar alloy content.

Reduced work hardening typically leads to low tensile ductility in ultrafine grained steels. According to the work of Park et al. [102], an ultrafine grained low carbon steel (0.15C–1.1Mn–0.25Si, wt.%) with a grain size of 0.2 μm, manufactured by severe plastic deformation (accumulative equivalent strain of 4.0 at 623 K), exhibited no work hardening, i.e. necking occurred already in the Lüders regime. Therefore, only a small "uniform" elongation was reported. As an example, Fig. 4 provides data on tensile ductility versus inverse square root of grain size for bcc steels with grain sizes of 150–0.2 μm. For each of the steels, the total elongation is represented by an open symbol and the uniform elongation is displayed by a filled symbol. The figure shows that a decrease in grain size leads to a decrease in ductility. A sudden drop of elongation at a grain size of about 1 μm was reported in the study by Tsuji et al. (circles) for an IF steel refined by the ARB process at 773 K and subsequent annealing [24]. It is interesting to note that this tendency does not apply to the ultrafine grained dual phase steel (diamonds) according to Son et al. [46], produced by ECAP with an effective strain of around 4.0 at 773 K and subsequent intercritical annealing at 1003 K for 10 min. The uniform elongation was higher for the ultrafine grained dual phase steel (the sizes of the ferrite grains and martensite islands were about 0.8 μm), while the total elongation was comparable to its coarse grained counterpart, having ferrite grain and martensite island diameters of about 19.4 and 9.8 μm, respectively. The authors attributed the better ductility in the ultrafine grained dual phase steel to extensive work hardening associated with a high density of mobile dislocations.

The decrease in tensile ductility at room temperature for most of the ultrafine grained steels, especially single phase steels, can be explained as follows. First, dynamic recovery as a softening mechanism is able to reduce the apparent work hardening rate. During deformation, dislocations that carry the intragranular strain are trapped at grain boundaries. The kinetics of dynamic recovery are associated with the spreading of trapped lattice dislocations into grain boundaries especially in ultrafine grained steels [106–108]. The change of the dislocation density during dynamic recovery in terms of the trapped lattice dislocations spreading into the grain boundaries was studied in detail by Park et al. [102]. The authors calculated approximate recovery times for dislocations moving into grain boundaries, and showed that for ultrafine grained steels the time for dislocations moving into grain boundaries is shorter than the time of the tensile test. This decrease in dislocation density reduces accumulation of dislocations inside grains, and consequently leads to less work hardening when compared with corresponding steels of large grain size. Following these earlier investigations, it is suggested that there are two kinds of recovery mechanisms, namely, slow recovery in the grain interiors and much faster recovery in the vicinity of grain boundaries. In coarse grained steels, the latter mechanism is less important due to the lower volume fraction of material near grain boundaries. Taking the study of Song et

al. [44] for example, a plain carbon steel (0.2 wt.% C) grain diameter was reduced from 6.8 to 1.3 μm. This grain refinement enhanced the fraction of the overall volume near grain boundaries by a factor of about 143. Thus, in ultrafine grained steels, faster recovery near grain boundaries seems to be important.

Second, the decrease in tensile ductility can be explained in terms of plastic instability, which initiates necking due to localized deformation. The condition for initiation of necking in a uniaxial tensile test is indicated by the Considère criterion [109], $\sigma_t = d\sigma_t/d\varepsilon_t$. When the slope of the true-stress true-strain curve (work hardening rate), $d\sigma_t/d\varepsilon_t$, is equal to the true stress, σ_t, uniform deformation stops and necking is initiated. As mentioned above, ultra grain-refinement greatly increases the flow stress of steels, especially during the early stages of plastic deformation. Grain refinement also leads to reduced work hardening capacity. As a result, plastic instability (necking) occurs at an early stage during tensile testing, which results in limited uniform elongation in ultrafine grained steels.

The yield ratio is high in ultrafine grained steels. However, according to the study by Song et al. [44], good ductility can still be obtained in 0.2% C steel, as documented by a total elongation of about 20% and uniform elongation of about 10% (Fig. 5). These values differ from the results reported in previous studies, where total elongations are usually below 10%. The high ductility observed by Song et al. was attributed to the presence of finely dispersed cementite particles, which increase the work hardening rate [42]. A large volume fraction and a fine dispersion of cementite effectively increase the work hardening rate by promoting accumulation of dislocations around the particles [110,111]. Another approach to improve the tensile ductility of ultrafine grained steel at room temperature is to adopt a composite structure in which only the surface is ultrafine, while the core with a coarse microstructure provides ductility. An interesting extension of this idea is to employ ultrafine grains locally, only where they are needed in the product to locally generate high strength and toughness [112].

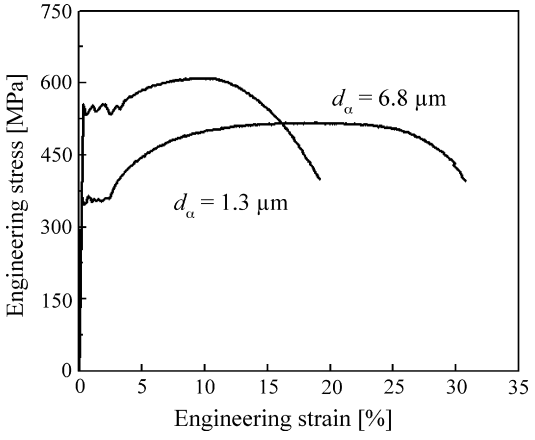

Fig. 5. Comparison of engineering stress–strain curves of the 0.2% C steels with different ferrite grain sizes. The different grain sizes were produced by the conventional route (without large strain warm deformation) and the ultrafine grain route, respectively. The ultrafine grain route involved a warm deformation procedure with four steps (each deformation step with $\varepsilon = 0.4$ and $\dot{\varepsilon} = 10\,s^{-1}$) and a subsequent 2 h annealing treatment at 823 K. The symbol d_α refers to the average ferrite grain diameter. After Song et al. [44].

4.3. Lüders strain

It is well known that a decrease in grain size leads to an increase in Lüders strain as illustrated in Fig. 5 [44]. A large Lüders strain has also been noted by Lloyd and Morris [113] in a fine grained (1–3 μm) Al–6% Ni alloy that contained small amounts of magnesium in solid solution. They observed that the reduction of grain size entailed an increase in yield stress and a decrease in work hardening. Hayes and Wang [114,115] conducted a study on the influence of grain refinement on Lüders strain in Al alloys. They investigated the serrated strain regime for specimens with various grain sizes between 0.4 and 20 μm and observed that the Lüders strain was linearly proportional to the inverse square root of the grain size in Al alloys, as in the Hall–Petch relationship. The appearance of pronounced yield drops and very large Lüders strain regimes thus appear to be characteristics of ultrafine grained Al alloys as well as steels [44,114]. These phenomena can be linked to an instantaneous low density of mobile dislocations, lack of dislocation sources within grains, and the low work hardening rate of ultrafine grained alloys.

The serrated flow that characterizes the propagation of plastic strain within a Lüders band is governed by the dynamic interplay of micromechanical hardening and softening. The Lüders regime is determined by the population of mobile dislocations, the strain hardening coefficient, the strain softening coefficient, the strain rate and temperature [42]. Song et al. [42] reported that yielding involved the initiation of deformation bands due to local stress concentrations. Owing to the high density of mobile dislocations formed by unlocking and by dislocation multiplication, the material within the deformation band effectively softens and undergoes localized plastic deformation. As mentioned in Section 4.2, dynamic recovery is pronounced in steels with smaller grain sizes owing to fast recovery in the vicinity of grain boundaries [102]. A decrease in the work hardening rate in the ultrafine grained steel, which can be attributed to the rapid dynamic recovery, favors a non-uniform deformation mode like local deformation by Lüders bands. This leads to slow propagation of the Lüders band front in the steel with a fine microstructure. The slow propagation is coupled with a large Lüders strain.

5. Toughness of ultrafine grained bcc steels

5.1. Toughness improvement in ultrafine grained steels

While several studies examined tensile properties of ultrafine grained steels, Charpy impact properties were less commonly investigated due to limitations in the sample size typically available from laboratory-scale process set-ups.

The impact properties of ultrafine grained IF, low/medium carbon and Nb–V–Ti microalloyed steels have been reported by Tsuji et al. [116], Hanamura et al. [105], Song et al. [44] and Sjong et al. [117]. Fig. 6 shows the impact transition curves of the medium carbon steels (0.2 wt.% C) for subsize (3 mm × 4 mm) specimens [44]. Compared with conventional steel (grain size: 6.8 μm), the upper shelf energy is lower and the transition

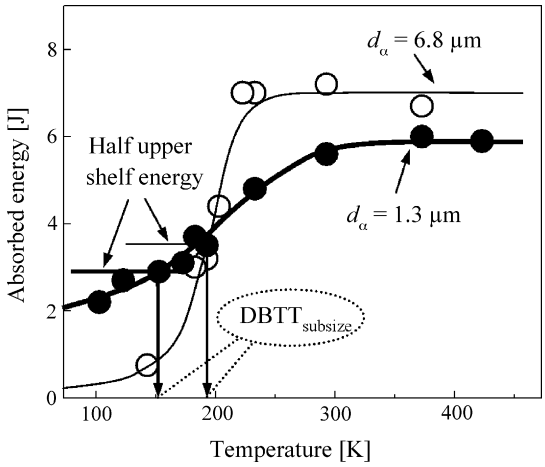

Fig. 6. Dependence of the Charpy impact properties on temperature of the steels with different ferrite grain sizes [44]. The symbol d_α refers to average ferrite grain diameter. DBTT$_{subsize}$: ductile-to-brittle transition temperature of subsize specimen with a 1 mm notch depth and a ligament size of 3 mm × 3 mm. The ductile-to-brittle transition temperature was determined by using the correlation procedure recommended in [118].

region occurs over a wider temperature range in the ultrafine grained steel (grain size: 1.3 μm). The ductile-to-brittle transition temperature was defined as the temperature at half of the upper shelf energy [44]. Fig. 6 shows the decrease in ductile-to-brittle transition temperature (from 193 to 153 K) associated with grain refinement into the ultrafine ferrite regime. In the ductile-to-brittle transition region, the temperature dependence of the absorbed energy is reduced for the ultrafine grained steel. Currently, there is insufficient data to report quantitatively on the relationship between grain size and toughness in the ultrafine and nanocrystalline regime.

5.2. Fundamental explanation for the low ductile-to-brittle transition temperature in ultrafine grained steels

5.2.1. Effect of grain refinement on improving toughness

A reduction in the average grain size commonly leads to a lower ductile-to-brittle transition temperature. This can be understood in terms of cleavage crack initiation and propagation. It is known that the grain size is one of the major factors determining the cleavage fracture unit [119,120]. A decrease in grain size can limit the propagation of initiated cleavage cracks and raise the fracture toughness in the transition region. Since the ductile-to-brittle transition temperature is the point at which the yield stress is equal to the cleavage fracture stress, the ductile-to-brittle transition temperature is lowered by grain refinement due to a more significant increase in the cleavage fracture stress than in the yield stress.

5.2.2. Effect of delamination on lowing the ductile-to-brittle transition temperature

Delamination behavior in Charpy specimens has been reported by several researchers [44,116,121–124]. As shown in Fig. 7, a decrease in grain size or Charpy impact testing temperature leads to an increase in the number of delaminations.

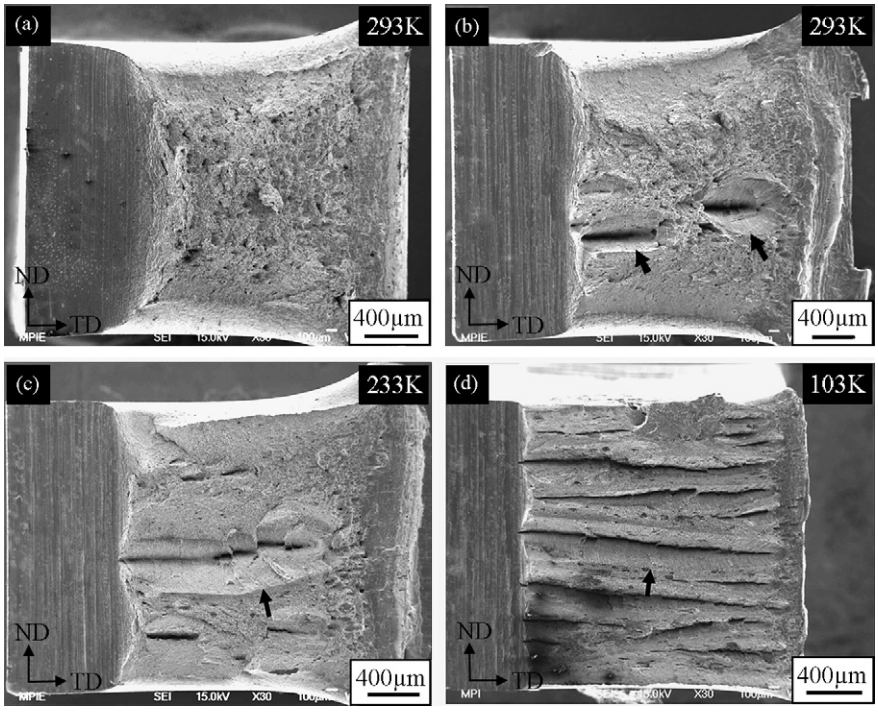

Fig. 7. Scanning electron microscope (SEM) images of fracture surfaces for the steels with different ferrite grain sizes after subsize (3 mm × 4 mm) Charpy V-notch impact tests. (a) Fracture surface of the conventional 0.2% C steel (average ferrite grain diameter of 6.8 μm) after impact testing at 293 K; (b–d) fracture surfaces of the ultrafine grained 0.2% C steel (average ferrite grain diameter of 1.3 μm) after impact testing at 293, 233 and 103 K, respectively. The black arrows point out material delaminations. After [44].

The origin of the delaminations is not completely understood at present. From previous studies it seems that distorted ferrite–pearlite microstructures [125], elongated ferrite grain shapes [121], certain texture characteristics [44,124,126], and aligned particles and inclusions [44,127] favor the occurrence of delamination. However, the phenomenon of delamination does not have a direct influence on the speed of crack growth in ductile failure [128]. Nevertheless, delamination leads to a reduction of the ductile-to-brittle transition temperature in the impact test samples of the ultrafine grained steel due to a decrease in the triaxiality of the stress state [44].

5.3. Shelf energy

The ductile-to-brittle transition in steels is associated with two different failure mechanisms. At high temperatures in the upper shelf region, fracture occurs by nucleation and coalescence of microvoids entailing ductile tearing. This process requires extensive plastic deformation and large amounts of energy. At low temperatures, fracture occurs by cleavage, which is the sudden separation of atomic planes across the specimen [125,129]. In this case, less energy is required.

5.3.1. Lower shelf energy

Fig. 6 shows that the lower shelf energy is significantly higher in the ultrafine grained steel than in the coarse grained steel. On the one hand, this can be attributed to the effect of grain refinement on improving toughness even at very low temperatures. This behavior is shown by the presence of about 50% shear fracture in the ultrafine grained subsize specimen when the test temperature was as low as 103 K. Low temperature toughness can also be enhanced by anisotropic microstructure or pronounced crystallographic texture of the ultrafine grained steel produced by the large strain deformation below the A_1 temperature (austenite to pearlite transformation finish temperature) [44].

Fig. 8a shows the fracture surface of an ultrafine grained 0.2% C steel after Charpy impact testing at 103 K. The high-magnification view of the fracture surface in Fig. 8b clearly shows the smooth delamination surface as well as the dimpled ductile fracture area. The smooth undulating surface suggests some type of decohesion of the grain boundaries. Fig. 8c shows delaminations in the rolling direction, and Fig. 8d shows delaminations following the elongated grain boundaries. The occurrence of delamination along the grain boundaries, both above and below an elongated grain, indicates that the crack can make minor adjustments in its propagation direction switching from one grain boundary to another. This is also confirmed by the observation that two elongated grains (i.e. grain "1" and grain "2" in Fig. 8d) with different texture components, ⟨1 1 1⟩ ∥ ND and ⟨0 0 1⟩ ∥ ND, respectively, were separated by a crack. The delaminations appear to propagate by means of a low-energy fracture mechanism that produces a fairly smooth fracture surface. This fracture does not exhibit the typical cleavage appear-

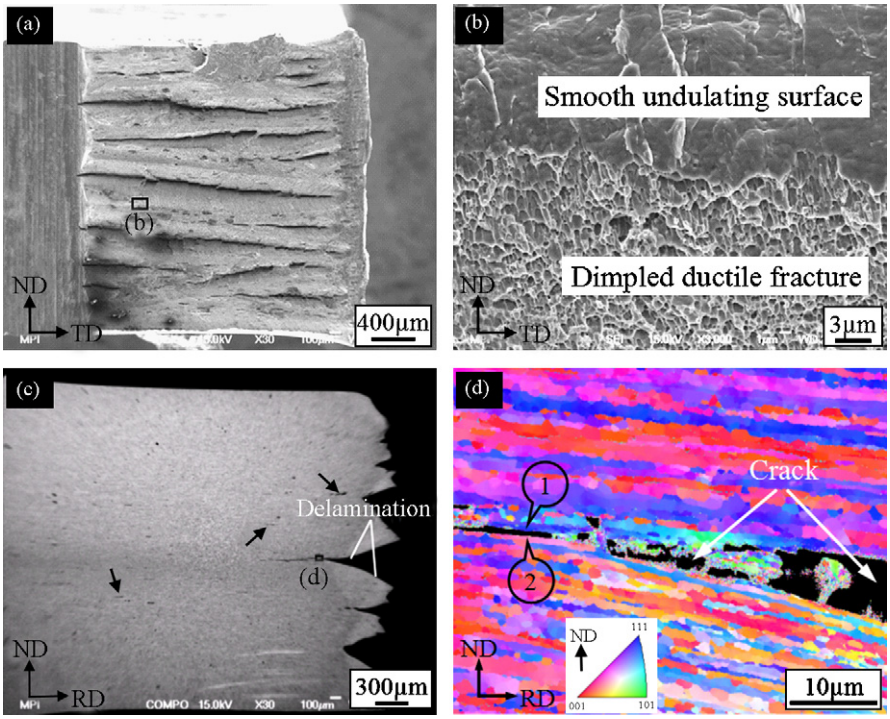

Fig. 8. SEM micrographs and ND (normal direction) orientation map (taken by electron backscatter diffraction (EBSD) measurement) of ultrafine grained 0.2% C steel (average ferrite grain diameter of 1.3 μm) after subsize Charpy impact testing at 103 K. The images shown in (a) and (b) are taken from a plane normal to the rolling direction (RD), while (c) and (d) are normal to the transverse direction (TD) of the sample. Orientation components in (d), ⟨1 1 1⟩ ∥ ND in blue, ⟨0 0 1⟩ ∥ ND in red and ⟨1 0 1⟩ ∥ ND in green. After [44]. (a) Overall fracture surface; (b) transition between delaminated and shear fracture regions. The observation area of (b) is shown in (a). (c) Longitudinal cross-section. The black arrows point out chains of large voids in the specimen; (d) crack propagation along interfaces. The circles 1 and 2 show two elongated grains with high-angle grain boundaries in between. The observation area of (d) is shown in (c).

ance with a strong (1 0 0) texture [121] and contributes to a higher fracture toughness in the lower shelf energy region for the ultrafine grained steel investigated due to reduced triaxiality of the stress state [44]. According to Song et al. [44], a high-angle grain boundary can act as a favorable path for crack propagation especially when large cementite particles are located along the boundary. An alternating microstructure of ferrite and aligned cementite can facilitate the spread of cracks in both the transverse and rolling directions.

5.3.2. Upper shelf energy

A reduced upper shelf energy can be observed in Fig. 6 in the ultrafine grained steel compared with a conventional steel of the same composition. This may be due to the relatively low work hardening and ductility of this steel, consistent with the smaller integrated area below the engineering stress–strain curve, Fig. 5. Delaminations in the ultrafine grained steel observed in the upper shelf region may also contribute to the reduced upper shelf energy.

Compared to the shear fracture surface in the conventional steel (Fig. 7a), a few delaminations can be observed in the ultrafine grained steel (Fig. 7b) Charpy impact specimen tested at room temperature (in the upper shelf region). Since there is little plastic deformation in the area of the delamination, lower absorbed energy and reduced fracture toughness is not surprising in the ultrafine grained steel (Fig. 7b) compared with the conventional steel exhibiting complete shear fracture (Fig. 7a). This differs from the lower shelf energy region, where a decrease in the ductile-to-brittle transition temperature is evident in the ultrafine grained steel due to the change in the stress triaxiality associated with relaxing σ_{zz}. As a result, reduced upper shelf energy and reduced ductile-to-brittle transition temperature appear characteristic of ultrafine grained steel processed by large strain warm deformation (Fig. 6).

According to the work of Fujioka et al. [130], a reduction of the upper shelf energy was also observed in a 0.16C–0.44Si–1.33Mn–0.012Ti–0.013Nb steel with a grain size of 1.5 μm. The ultrafine grained steel in their study was produced by flat rolling with a total logarithmic strain of $\varepsilon \approx 2.5$ at 973 K. They attributed the reduced value of the upper shelf energy to the elongated grain morphology in the ultrafine grained steel. However, in the study of Nagai [131] the same value of upper shelf energy was found for an ultrafine and a coarse grained steel (0.15C–0.3Si–1.5Mn) with grain sizes of 0.9 and 20 μm, respectively. The ultrafine grained steel was fabricated by warm rolling. The sample was rotated 90° about the rolling direction after each pass in order to conduct multi-directional deformation. The upper shelf energy was unexpectedly high, and was explained by the low impurity level of the steel investigated [131].

According to reports in the literature on the shelf energy of ultrafine grained steels [44,130,131], a reduced value of the upper shelf energy in two-phase ultrafine grained materials may be mainly due to the anisotropic microstructure resulting from the large strain deformation. Currently, large strain deformation at a low deformation temperature is a favorable method to produce ultrafine grained microstructures. Therefore, it might be particularly attractive in the future to develop ultrafine grained steels by the use of relatively lower strains and higher temperatures to develop microstructures with fewer delaminations.

6. Conclusions

Processing, microstructure and mechanical properties of ultrafine grained bcc steels were discussed and compared with several of their coarse grained counterparts. The following conclusions can be drawn based on the interpretations presented in this paper:

(1) Ultrafine grained bcc steels can be produced by severe plastic deformation techniques or advanced thermomechanical processing routes. For the severe plastic deformation methods, a well-designed strain path is more important and also more feasible than a precisely controlled temperature path. The small scale, complexity and the discontinuous nature of these processes suggest that they would require considerable ingenuity and investment to be applied on a high-volume industrial scale. Compared with severe plastic deformation methods, the advanced thermomechanical processing routes are less effective with respect to grain refinement, but they are more efficient with respect to large sample sizes. A further difference between these two approaches is that the advanced thermomechanical methods are continuous processes, require less total strain, and can be readily optimized when they work in a temperature regime where they exploit phase transformation.

(2) The submicron structure produced by SPD is typically more elongated due to the intense deformation involved. Around 40% of the grain boundaries are usually subgrain boundaries (grain boundary misorientations <15°) so that many cells are not actually grains but subgrains which are less beneficial for the overall mechanical response of such specimens. It is difficult for the cells to be transformed into real grains, which are surrounded by high-angle grain boundaries without an annealing treatment.

Hot deformation develops larger more polygonized cells or subgrains as a result of dynamic recovery. Hot working at intermediate temperature often provides a mixed microstructure. Deformation induced grain subdivision is essential for the formation of ultrafine grained microstructures by warm and cold working. Pronounced recovery/recrystallization processes are necessary to form high-angle grain boundaries.

(3) An improved combination of strength and toughness is obtained in ultrafine grained steels compared with their coarse grained counterparts. Reasonable ductility in ultrafine grained steel can be attributed to the presence of finely dispersed particles which improve the work hardening capacity owing to the accumulation of geometrically necessary dislocations around the particles. Ultrafine grained steel exhibits a large Lüders strain because of the relatively low work hardening rate due to rapid dynamic recovery in ultrafine grained steel compared with coarse grained steel. In ultrafine grained steel, the upper shelf energy is rela-

tively low due to the occurrence of delaminations. Some factors such as crystallographic texture and alignment of cementite particles along the ferrite grain boundaries, etc., may promote the formation of delaminations. The lower shelf energy is significantly raised and the ductile-to-brittle transition temperature is reduced in ultrafine grained steel compared to conventional steel. This can be attributed to the joint effect of the small ferrite grain size and the occurrence of delamination, which involves a decrease in the triaxiality of the stress state in the impact test samples of the ultrafine grained steel.

Acknowledgements

The authors would like to express their gratitude for the financial support of the European Coal and Steel Community (ECSC). The support of the Max-Planck-Institut für Eisenforschung in Germany and the sponsors of the Advanced Steel Processing and Products Research Center at the Colorado School of Mines in the USA are gratefully acknowledged.

References

[1] G. Frommeyer, J.A. Jiménez, Metall. Mater. Trans. A 36 (2005) 295.
[2] R.Z. Valiev, A.V. Sergueeva, A.K. Mukherjee, Scripta Mater. 49 (2003) 669.
[3] I.V. Alexandrov, R.Z. Valiev, Scripta Mater. 44 (2001) 1605.
[4] V.V. Stolyarov, Y.T. Zhu, T.C. Lowe, R.K. Islamgaliev, R.Z. Valiev, Nanostruct. Mater. 11 (1999) 947.
[5] R.Z. Valiev, Mater. Sci. Eng. A 234 (1997) 59.
[6] V.M. Segal, Mater. Sci. Eng. A 271 (1999) 322.
[7] Y. Fukuda, K. Oh-Ishi, Z. Horita, T.G. Langdon, Acta Mater. 50 (2002) 1359.
[8] J. Kim, I. Kim, D.H. Shin, Scripta Mater. 45 (2001) 421.
[9] D.H. Shin, I. Kim, J. Kim, K.T. Park, Acta Mater. 49 (2001) 1285.
[10] Z. Horita, M. Furukawa, M. Nemoto, T.G. Langdon, Mater. Sci. Technol. 16 (2000) 1239.
[11] Y.T. Zhu, T.C. Lowe, Mater. Sci. Eng. A 291 (2000) 46.
[12] Y. Saito, H. Utsunomiya, N. Tsuji, T. Sakai, Acta Mater. 47 (1999) 579.
[13] N. Tsuji, R. Ueji, Y. Minamino, Scripta Mater. 47 (2002) 69.
[14] N. Tsuji, Y. Saito, H. Utsunomiya, S. Tanigawa, Scripta Mater. 40 (1999) 795.
[15] T. Inoue, S. Torizuka, K. Nagai, Proceedings of the International Symposium on Ultrafine Grained Steels (ISUGS 2001), The Iron and Steel Institute of Japan, Fukuoka, Japan, 2001, pp. 88–91.
[16] Y. Ivanisenko, R.Z. Valiev, W. Lojkowski, A. Grob, H.J. Fecht, Ultrafine Grained Materials, vol. II, TMS, Seattle, USA, 2002, pp. 47–54.
[17] Y. Ivanisenko, R.K. Wunderlich, R.Z. Valiev, H.J. Fecht, Scripta Mater. 49 (2003) 947.
[18] Y. Ivanisenko, W. Lojkowski, R.Z. Valiev, H.J. Fecht, Acta Mater. 51 (2003) 5555.
[19] R.Z. Valiev, I.V. Alexandrov, Ann. Chim. Sci. Matér. 27 (2002) 3.
[20] V.M. Segal, V.I. Reznikov, A.D. Drobyshevskiy, V.I. Kopylov, Russ. Metall. 1 (1981) 99.
[21] R.Z. Valiev, N.A. Krasilnikov, N.K. Tsenev, Mater. Sci. Eng. A 137 (1991) 35.
[22] D.H. Shin, B.C. Kim, Y.-S. Kim, K.-T. Park, Acta Mater. 48 (2000) 2247.
[23] N. Kamikawa, N. Tsuji, Y. Minamino, Sci. Technol. Adv. Mater. 5 (2004) 163.
[24] N. Tsuji, Y. Ito, Y. Saito, Y. Minamino, Scripta Mater. 47 (2002) 893.
[25] Y. Saito, N. Tsuji, H. Utsunomiya, T. Sakai, R.G. Hong, Scripta Mater. 39 (1998) 1221.
[26] R. Kaspar, J.S. Distl, O. Pawelski, Steel Res. 59 (1988) 421.
[27] P.D. Hodgson, M.R. Hickson, R.K. Gibbs, Scripta Mater. 40 (1999) 1179.
[28] H. Mabuchi, T. Hasegawa, T. Ishikawa, ISIJ Int. 39 (1999) 477.
[29] Z.M. Yang, R.Z. Wang, ISIJ Int. 43 (2003) 761.
[30] J.K. Choi, D.H. Seo, J.S. Lee, K.K. UM, W.Y. Choo, ISIJ Int. 43 (2003) 764.
[31] M.R. Hickson, P.J. Hurley, R.K. Gibbs, G.L. Kelly, P.D. Hodgson, Metall. Mater. Trans. A 33 (2002) 1019.
[32] S.C. Hong, S.H. Lim, K.J. Lee, D.H. Shin, K.S. Lee, ISIJ Int. 43 (2003) 394.
[33] Y. Matsumura, H. Yada, ISIJ Int. 27 (1987) 492.
[34] A. Najafi-Zadeh, J.J. Jonas, S. Yue, Metall. Trans. A 23 (1992) 2607.
[35] N. Tsuji, Y. Matsubara, Y. Saito, Scripta Mater. 37 (1997) 477.
[36] S.V.S. Murty, S. Torizuka, K. Nagai, T. Kitai, Y. Kogo, Scripta Mater. 53 (2005) 763.
[37] J. Baczynski, J.J. Jonas, Metall. Trans. A 29 (1998) 447.
[38] Y. Weng, ISIJ Int. 43 (2003) 1675.
[39] R. Song, D. Ponge, D. Raabe, R. Kaspar, Acta Mater. 53 (2005) 845.
[40] R. Song, R. Kaspar, D. Ponge, D. Raabe, Ultrafine Grained Materials, vol. III, TMS, Charlotte, North Carolina, USA, 2004, p. 445.
[41] R. Song, D. Ponge, R. Kaspar, D. Raabe, Z. Metallkd. 95 (2004) 513.
[42] R. Song, D. Ponge, D. Raabe, Scripta Mater. 52 (2005) 1075.
[43] R. Song, D. Ponge, R. Kaspar, Steel Res. 75 (2004) 33.
[44] R. Song, D. Ponge, D. Raabe, Acta Mater. 53 (2005) 4881.
[45] R. Song, D. Ponge, D. Raabe, ISIJ Int. 45 (2005) 1721.
[46] Y.I. Son, Y.K. Lee, K.-T. Park, C.S. Lee, D.H. Shin, Acta Mater. 53 (2005) 3125.
[47] G. Azevedo, R. Barbosa, E.V. Pereloma, D.B. Santos, Mater. Sci. Eng. A 402 (2005) 98.
[48] K.-T. Park, S.Y. Han, B.D. Ahn, D.H. Shin, Y.K. Lee, K.K. Um, Scripta Mater. 51 (2004) 909.
[49] R. Ueji, N. Tsuji, Y. Minamino, Y. Koizumi, Acta Mater. 50 (2002) 4177.
[50] N. Tsuji, R. Ueji, Y. Minamino, Y. Saito, Scripta Mater. 46 (2002) 305.
[51] R. Ueji, N. Tsuji, Y. Minamino, Y. Koizumi, Sci. Technol. Adv. Mater. 5 (2004) 153.
[52] M.R. Hickson, P.D. Hodgson, Mater. Sci. Technol. 15 (1999) 85.
[53] P.J. Hurley, P.D. Hodgson, B.C. Muddle, Scripta Mater. 40 (1999) 433.
[54] P.J. Hurley, P.D. Hodgson, Mater. Sci. Eng. A 302 (2001) 206.
[55] H. Mabuchi, T. Hasegawa, T. Ishikawa, ISIJ Int. 39 (1999) 477.
[56] R. Priestner, A.K. Ibraheem, Mater. Sci. Technol. 16 (2000) 1267.
[57] H. Yada, Y. Matsumura, K. Nakajima, United State Patent, 4,466,842, Nippon Steel Corporation, Tokyo (1984).
[58] D.J. Hamre, D.K. Matlock, J.G. Speer, in: E. Essadiqi, J. Thomson (Eds.), Ultra-fine Structured Steels, Canada Institute of Mining, Metallurgy, and Petroleum, Montreal, Canada, 2004, pp. 109–121.
[59] W.J. Kim, J.K. Kim, W.Y. Choo, S.I. Hong, J.D. Lee, Mater. Lett. 51 (2001) 177.
[60] S. Nanba, M. Nomura, N. Matsukura, K. Makii, Y. Shirota, Proceedings of the International Symposium on Ultrafine Grained Steels (ISUGS 2001), The Iron and Steel Institute of Japan, Fukuoka, Japan, 2001, pp. 286–289.
[61] H.J. McQueen, N.D. Ryan, in: E. Essadiqi, J. Thomson (Eds.), Ultra-fine Structured Steels, Met. Soc. CIM, 2004, pp. 55–67.
[62] D.H. Shin, B.C. Kim, K.-T. Park, W.Y. Choo, Acta Mater. 48 (2000) 3245.
[63] K.-T. Park, Y.K. Lee, D.H. Shin, ISIJ Int. 45 (2005) 750.
[64] N. Tsuji, Y. Saito, S.-H. Lee, Y. Minamino, Adv. Eng. Mater. 5 (2003) 338.
[65] X. Huang, N. Tsuji, N. Hansen, Y. Minamino, Mater. Sci. Eng. A 340 (2003) 265.
[66] M. Hölscher, D. Raabe, K. Lücke, Steel Res. 62 (1991) 567.
[67] M. Hölscher, D. Raabe, K. Lücke, Acta Metall. 42 (1994) 879.
[68] D. Raabe, K. Lücke, Mater. Sci. Technol. 9 (1993) 302.
[69] D. Raabe, Mater. Sci. Technol. 11 (1995) 461.
[70] M.R. Hickson, R.K. Gibbs, P.D. Hodgson, ISIJ Int. 39 (1999) 1176.
[71] Z.M. Yang, R.Z. Wang, ISIJ Int. 43 (2003) 761.
[72] J.-K. Choi, D.-H. Seo, J.-S. Lee, K.-K. Um, W.-Y. Choo, ISIJ Int. 43 (2003) 746.
[73] P.J. Hurley, G.L. Kelly, P.D. Hodgson, Mater. Sci. Technol. 16 (2000) 1273.

[74] S.C. Hong, S.H. Lim, K.J. Lee, D.H. Shin, K.S. Lee, ISIJ Int. 43 (2003) 394.
[75] S.C. Hong, K.S. Lee, Mater. Sci. Eng. A 323 (2002) 148.
[76] A. Bodin, J. Sietsma, S. van der Zwaag, Mater. Charact. 47 (2001) 187.
[77] G.H. Akbari, C.M. Sellars, J.A. Whiteman, Acta Mater. 45 (1997) 5047.
[78] D.H. Shin, J.-J. Park, S.Y. Chang, Y.-K. Lee, K.-T. Park, ISIJ Int. 42 (2002) 1490.
[79] D.H. Shin, C.W. Seo, J. Kim, K.-T. Park, W.Y. Choo, Scripta Mater. 42 (2000) 695.
[80] M.Y. Liu, B. Shi, C. Wang, S.K. Ji, X. Cai, H.W. Song, Mater. Lett. 57 (2003) 2798.
[81] R. Song, Microstructure and Mechanical Properties of Ultrafine Grained C–Mn Steels, Shaker Verlag GmbH, Aachen, 2005, p. 126.
[82] W.B. Morrison, Trans. ASM 59 (1966) 824.
[83] A.A.W. Thompson, Acta Metall. 23 (1975) 1337.
[84] A.A.W. Thompson, Acta Metall. 25 (1977) 83.
[85] W.M. Baldwin, Acta Metall. 6 (1958) 139.
[86] R.W. Armstrong, I. Codd, R.M. Douthwaite, N.J. Petch, Philos. Mag. 7 (1962) 45.
[87] J.D. Campbell, K.J. Marsh, Philos. Mag. 7 (1962) 933.
[88] H. Conrad, Acta Metall. 11 (1963) 75.
[89] N.J. Petch, Iron Steel Inst. 174 (1953) 25.
[90] A.H. Cottrell, Trans. Metall. Soc. AIME 212 (1958) 192.
[91] J.S. Koehler, Phys. Rev. 85 (1952) 480.
[92] A.A. Johnson, Philos. Mag. 7 (1962) 177.
[93] H. Conrad, S. Feuerstein, L. Rice, Mater. Sci. Eng. 2 (1967) 157.
[94] J.C.M. Li, Trans. Metall. Soc. AIME 227 (1963) 239.
[95] J.C.M. Li, Y.T. Chou, Metall. Trans. 1 (1970) 1145.
[96] C.S. Pande, R.A. Masumura, R.W. Armstrong, Nanostruct. Mater. 2 (1993) 323.
[97] J.D. Eshelby, F.C. Frank, Philos. Mag. 42 (1951) 351.
[98] T.E. Mitchell, S.S. Hecker, R.L. Smialek, Phys. Stat. Sol. 11 (1965) 585.
[99] R.W. Armstrong, Y.T. Chou, R.M. Fisher, N. Louat, Philos. Mag. 14 (1966) 943.
[100] H.W. Song, S.R. Guo, Z.Q. Hu, Nanostruct. Mater. 11 (1999) 203.
[101] M. Liu, B. Shi, G. Bi, H. Cao, X. Cai, H. Song, Mater. Sci. Eng. A 360 (2003) 101.
[102] K.T. Park, Y.S. Kim, J.G. Lee, D.H. Shin, Mater. Sci. Eng. A 293 (2000) 165.
[103] A. Azushima, K. Aoki, Mater. Sci. Eng. A 337 (2002) 45.
[104] K.-T. Park, S.Y. Han, D.H. Shin, Y.-K. Lee, K.J. Lee, K.S. Lee, ISIJ Int. 44 (2004) 1057.
[105] T. Hanamura, F. Yin, K. Nagai, ISIJ Int. 44 (2004) 610.
[106] R.Z. Valiev, E.V. Kozlov, Y.F. Ivanov, J. Lian, A.A. Nazarov, B. Baudelet, Acta Metall. Mater. 42 (1994) 2467.
[107] J. Lian, B. Baudelet, A.A. Nazarov, Mater. Sci. Eng. A 172 (1993) 23.
[108] W. Lojkowski, Acta Metall. Mater. 39 (1991) 1891.
[109] R.E. Reed-Hill, R. Abbaschian, Physical Metall Principles, PWS Publishing Company, 1994, p. 158.
[110] M.F. Ashby, Philos. Mag. 21 (1970) 399.
[111] J.C. Fisher, E.W. Hart, R.H. Pry, Acta Mater. 1 (1953) 336.
[112] A.A. Howe, Mater. Sci. Technol. 16 (2000) 1264.
[113] D.J. Lloyd, L.R. Morris, Acta Metall. 25 (1977) 857.
[114] J.S. Hayes, R. Keyte, P.B. Prangnell, Mater. Sci. Technol. 16 (2000) 1259.
[115] Z.C. Wang, P.B. Prangnell, Mater. Sci. Eng. A 328 (2002) 87.
[116] N. Tsuji, S. Okuno, Y. Koizumi, Y. Minamino, Mater. Trans. 45 (2004) 2272.
[117] A.L. Sjong, R.L. Bodnar, M.J. Merwin, D.K. Matlock, J.G. Speer, in: R.I. Asfahani, R.L. Bodnar, M.J. Merwin (Eds.), Proceedings of the Symposium on Microalloyed Steels, Ohio, 2002, pp. 92–100.
[118] R. Kaspar, H. Faul, MP Materialprüfung 43 (2001) 18.
[119] S. Kim, Y.R. Im, S. Lee, H.C. Lee, Y.J. Oh, J.H. Hong, Metall. Mater. Trans. A: Phys. Metall. Mater. Sci. 32 (2001) 903.
[120] P. Brozzo, G. Buzzichelli, A. Mascanzoni, M. Mirabile, Met. Sci. 11 (1977) 123.
[121] B.L. Bramfitt, A.R. Marder, Metall. Trans. A 8 (1977) 1263.
[122] T. Hashimoto, T. Sawamura, H. Ohtani, Iron Steel Inst. Jpn. 65 (1979) 1425.
[123] S. Matsuda, Y. Kawashima, S. Sekiguchi, M. Okamoto, Iron Steel Inst. Jpn. 68 (1982) 436.
[124] A. Ohmori, S. Torizuka, K. Nagai, Iron Steel Inst. Jpn. 89 (2003) 765.
[125] P. Shanmugam, S.D. Pathak, Eng. Fract. Mech. 53 (1996) 991.
[126] R. Schofield, G. Roentree, N.V. Sarma, R.T. Weiner, Met. Technol. (1974) 325.
[127] A.J. McEvely, R.H. Rush, Trans. ASM 55 (1962) 654.
[128] E. Miyoshi, M. Fukuda, H. Iwanaga, Okazawa T, Proceedings of the Inst. of Gas Eng. Conference, 1974 (paper 4).
[129] W. Pitsch, G. Sauthoff, H.P. Hougardy, in: V.D. Eisenhüttenleute (Ed.), A Handbook for Mater Research and Engineering, vol. 1, Springer-Verlag, 1992, p. 278.
[130] M. Fujioka, T. Yokota, Y. Adachi, N. Matsukura, Proceedings of the Second Symposium on Super Metal, Japan, 1999, p. 193.
[131] K. Nagai, Mater. Proc. Technol. 117 (2001) 329.